Synchronization and Phase Transitions on Multiplex Networks

Ph.D. Thesis

by

ANIL KUMAR

DISCIPLINE OF PHYSICS

INDIAN INSTITUTE OF TECHNOLOGY INDORE

NOVEMBER 2021

Synchronization and Phase Transitions on Multiplex Networks

A THESIS

Submitted in partial fulfillment of the requirements for the award of the degree

of

DOCTOR OF PHILOSOPHY

by

ANIL KUMAR

DISCIPLINE OF PHYSICS

INDIAN INSTITUTE OF TECHNOLOGY INDORE

NOVEMBER 2021

INDIAN INSTITUTE OF TECHNOLOGY INDORE

CANDIDATE'S DECLARATION

I hereby certify that the work which is being presented in the thesis entitled "**Synchronization and Phase Transitions on Multiplex Networks**" in the partial fulfillment of the requirements for the award of the degree of **DOCTOR OF PHILOSOPHY** and submitted in the **DISCIPLINE OF PHYSICS, Indian Institute of Technology Indore**, is an authentic record of my own work carried out during the time period from **July 2015** to **November 2021** under the supervision of **Dr. Sarika Jalan**, Professor, Indian Institute of Technology Indore, India.

The matter presented in this thesis has not been submitted by me for the award of any other degree of this or any other institute.

Anil
9/12/2021
Signature of the student with date
ANIL KUMAR

This is to certify that the above statement made by the candidate is correct to the best of my/our knowledge.

Signature of Thesis Supervisor with date

PROF. SARIKA JALAN

ANIL KUMAR has successfully given his/her Ph.D. Oral Examination held on 24/11/2021.

Signature of Chairperson (OEB) Date:	Signature of External Examiner Date:	Signature(s) of Thesis Supervisor(s) Date:
M. Shaikh Signature of PSPC Member #1 Date:	Signature of PSPC Member #2 Date:	Signature of Convener, DPGC Date:

Signature of Head of Discipline
Date:

डॉ. पंकज आर. सगदेव / Dr. Pankaj R. Sagdeo
विभाग प्रमुख / Head
भौतिकी शास्त्र विभाग / Department of Physics
भारतीय प्रौद्योगिकी संस्थान इन्दौर
Indian Institute of Technology Indore

Dedicated

to

My Family

Acknowledgements

First and foremost, I would like to thank my supervisor, Dr. Sarika Jalan, whose enthusiasm and devotion to her work is always an inspiration for me. Thanks a lot for always pushing me for improvement in every work that we have completed and for guiding me through challenges during the Ph.D.

My sincere thanks go to the PSPC committee members—Dr. Manavendra Maheto and Dr. Shaikh M. Mobin—for constructive suggestions in annual CERP meetings to improve my research work. I am thankful to the DPGC convener, Head of the physics department, Dean of academic affairs, and Director, IIT Indore for giving me some extra time to finish the Ph.D. work, without that I could not finish the program properly. I want to thank the staff members of the physics department for helping me in document processing on various occasions. I humbly acknowledge the sincere efforts of Mr. Tapesh Parihar (Academic office) and the medical team of IIT Indore for their help. I am grateful to CSIR-HRDG for providing the senior research fellowship during the last two years of the Ph.D.

Many thanks to all my past and present friends of the Complex Systems Lab: Aradhana, Sanjiv, Ajaydeep, Camellia, Alok, Aparna, Priodutti, Saptarishi, Pramod, Rahul, Ankit, Vasundhara, Tanu, Sanket, and Rhito for making my days at the lab wonderful. I have been staying at the JCB hall of residence since June 2019; I am thankful to every family there for a friendly environment for me and my family.

Finally, I wish to extend my deepest gratitude to my family members for always standing with me in the ups and downs of life. Without their support, perhaps, I can not face the challenges of life. I can never pay the debts of my parents for their selfless love and care. Thanks to my wife, Nirmla, who always works for my well-being and happiness without caring about her own needs. Lastly, I am blessed to have Hitesh (my son) in my life—playing games and spending time with him has been (and will always be) the most pleasant experience for me.

Abstract

Synchronization means rhythmic activity by connected dynamical units. Since 1665 when C. Huygens first noticed the synchronization of hanging pendulums, the question of how a collective behavior can emerge among the interacting elements of a population has always attracted significant attention from the science community. Further, daily life is full of phase transitions whether it is boiling of water to vapor or ferromagnetic transitions; therefore, it is no surprise that phase transitions occupy a prominent place in our longing to understand the natural phenomena around us. In network science also, coupled dynamical units usually exhibit a smooth and reversible transition from an incoherent state to a coherent or synchronized state; however, in rare cases, it can be discontinuous and irreversible as well. The latter is also called explosive synchronization (ES), and it brings various surprising results. Most of the studies on synchronization or explosive synchronization so far are confined to the classical concept of single or single-layer networks that treats all links among the nodes at the same foot. However, as realized recently, a group of nodes having different types of interactions should be treated as a multilayer or multiplex network. The multiplex networks are a special form of multilayer networks in which the same set of nodes are replicated in different layers; also, each node is connected to itself (also called mirror nodes) across the layers.

This thesis can be summarized into two broad questions. The first question one would probably ask while constructing a multiplex network is how to put interlayer connections? If there is any correlation among the mirror nodes, what is its impact on the synchronization ability of connected oscillators? Secondly, what are the different techniques using which one can change a continuous phase transition on multiplex networks into a discontinuous one or vice versa? What are the underlying causes behind the emergence of ES, and what factors govern the width of hysteresis associated with ES?

We investigate identical and non-identical phase oscillators. For the first case, we choose diffusive coupling, while for the latter, Kuramoto type coupling or Kuramoto Oscillators are considered. Due to their analytical solvability and relevance to real systems, the two models occupy a prominent place in the field of collective dynamics. For identi-

cal oscillators, we find that if nodes in individual layers have moderate (strong) degree-degree correlations, strong negative (moderate) degree-degree correlations among the mirror nodes are beneficial for global synchronizability (GS). Furthermore, as determined by degree-degree correlations, increasing connections in the multiplex networks is not always beneficial for the GS. For non-identical oscillators, we focus on the type of phase transition exhibited by the ensemble. We show that using three techniques, i.e., interlayer adaptation, interlayer phase-shifted interactions, and natural frequency displacement between the layers, one can induce ES in a two-layer multiplex network of Kuramoto oscillators. In all three cases, suppression of synchronization is accountable for the onset of ES. Since the ES is accompanied by a hysteresis, different parameters affecting the hysteresis size are discussed in detail. Our observations suggest that interlayer coupling and natural frequency mismatch between the mirror nodes play an important role in the emergence of ES. The robustness of ES against changes in network parameters (for instance, network topology, natural frequency distribution, etc.) is tested. A mean-field analysis is performed to justify the numerical simulations.

Extensive work on synchronization so far reveals that it does not require any proof of its relevance to real-world systems. It has applications in almost all branches of science—from physics, chemistry, and biology to ecology, sociology, and technology. Similarly, the discontinuous phase transitions are undesired in many real-world situations; therefore, it is worthy to investigate them thoroughly. We hope our findings on synchronization and explosive synchronization will strengthen our current understanding of collective dynamics existing in real-world systems that can be modeled in the multiplex framework.

List of Publications

A. Publications from the thesis:

1. **Anil Kumar**, Murilo S. Baptista, Alexey Zaikin, and Sarika Jalan (2017), *Mirror nodes correlations tuning synchronization in multiplex networks*, Phys. Rev. E **96**, 062301 (DOI:10.1103/PhysRevE.96.062301)

2. Sarika Jalan, **Anil Kumar**, and Inmaculada Leyva (2019), *Explosive synchronization in frequency displaced multiplex networks*, Chaos: An Interdisciplinary Journal of Nonlinear Science **29**, 041102 (DOI: 10.1063/1.5092226).

3. **Anil Kumar**, Sarika Jalan, and Ajaydeep Kachwach (2020), *Interlayer adaptation induced explosive synchronization in multiplex networks*, Phys. Rev. Research **2**, 023259 (DOI: 10.1103/PhysRevResearch.2.023259).

4. **Anil Kumar** and Sarika Jalan (2021), *Explosive synchronization in interlayer phase-shifted Kuramoto oscillators on multiplex networks*, Chaos: An Interdisciplinary Journal of Nonlinear Science **31**, 041103 (DOI: 10.1063/5.0043775).

B. Other publications:

5. Sarika Jalan, **Anil Kumar**, Alexey Zaikin, and Jurgen Kurths (2016), *Interplay of degree correlations and cluster synchronization*, Phys. Rev. E **94**, 062202 (DOI:10.1103/PhysRevE.94.062202).

6. Sergey Makovkin, **Anil Kumar**, Alexey Zaikin, Sarika Jalan, and Mikhail Ivanchenko (2017), *Multiplexing topologies and time scales: The gains and losses of synchrony*, Phys. Rev. E **96**, 052214 (DOI: 10.1103/PhysRevE.96.052214).

Table of Contents

List of Figures

List of Abbreviations

GS	Global Synchronizability
ES	Explosive Synchronization
ER	Erdös Rényi
SF	Scale – free

Chapter 1

Introduction

In this chapter, we introduce various basic concepts that will be used in the rest of the thesis.

1.1 Networks

In the simplistic definition, a network is a bunch of nodes connected with links. Social networks, biological networks, internet networks, world wide web (WWW) networks, technological networks, and citation networks are some popular examples of real-world systems where the networked representation of interacting elements has provided extensive information about these systems [1]. For instance, a networked representation of computers connected with the internet is helpful to know the shortest path for the traffic to flow, and therefore can be used in designing an efficient internet network. Social networks can provide information about how opinions changes in a society, and how a disease may spread. Finding important nodes and links in a power grid network whose failure will collapse the whole network is helpful to protect them from failures. The networked representation of interacting dynamical units, which will be our prime focus in this thesis, is helpful to understand different kinds of collective behaviors, e.g., synchronization, explosive synchronization, chimera states, etc.

1.2 Different Network Models

Here we introduce different network models that will be used in the thesis.

1.2.1 Globally Connected Networks

As suggested by its name, each node in a globally connected network is connected with every other node in the network. Therefore, the total number of links in a globally connected network of N nodes is $N(N-1)/2$.

1.2.2 Regular Ring Networks

A regular ring network, also called 1D network, of average connectivity $\langle k \rangle$ is generated as follows [2]: starting with a ring of N isolated nodes, each node in the ring is connected with its k nearest neighbors (or with $k/2$ nodes on either side).

1.2.3 Random Networks

As discussed in Section 1.1, real-world networks are certainly not regular in topology. In 1959, Erdös and Rényi [3] proposed a model to generate random networks. Since its introduction, their model has been used extensively in network science. According to Erdös and Rényi, a random network of size N and average connectivity $\langle k \rangle$ is generated in the following manner: Starting with N isolated nodes, a pair of nodes is selected and a random number is generated from a uniform distribution with range 0 to 1. The selected pair is connected with a link if the random number is less than or equal to $\langle k \rangle/(N-1)$; otherwise, the pair is left un-connected. The procedure is repeated for all the $N(N-1)/2$ pairs. In the honor of Erdös and Rényi, the resulting random network is also called Erdös-Rényi (ER) network. The degree distribution of an ER network, in the limit $N \to \infty$, is a Poisson distribution.

1.2.4 Bárabasi and Albert's Scale-free Networks

Network science aims to introduce network models that resemble real-world systems. Empirical data shows that the degree distribution of many real-world networks is not Poisson. For example, WWW network, internet network, movie actor networks, collaboration networks, power-grid networks, neural networks, metabolic networks, etc., are some of the popular examples where the degree distribution follows a power law [2]. These networks contain very few high degree nodes (also called hubs) and a large number of low degree nodes. Bárabasi and Albert [4] in 1999 suggested that ER networks fail to incorporate two important ingredients of real-world networks: growth and preferential attachment. To generate a Bárabasi and Albert's network, we start with arbitrarily connected m_0 nodes at time $t = 0$; also, each node should have at least one link. Next, at each time step, a new node with $m \leq m_0$ links is connected to the already existing nodes such that probability p_i of getting a link by an i^{th} node is proportional to its degree k_i, i.e.,

$$p_i = \frac{k_i}{\sum_j k_j}. \tag{1.1}$$

The summation in the denominator runs over all the existing nodes in the network. After following the procedure for t time steps, we get a network of $m_0 + t$ nodes which has $mt + m_{l0}$ edges. Here m_{l0} represents the total number of links in the network at time $t = 0$. In the limit $N \to \infty$, the network has a degree distribution $p(k)$ such that $p(k) \propto k^{-\gamma}$, with $\gamma = 3$. The degree distribution $p(k)$ is also called a power-law distribution, and a network following this is called scale-free (SF) network [2].

1.2.5 Scale-free Networks With Varying Degree Heterogeneity

The γ value in Bárabasi and Albert's SF networks remains constant at 3; however, it is natural that real-world networks may have different values of the scale-free exponent γ. The value of γ determines the spread in the degrees and thus heterogeneity in the degree distribution of a network. According to Dorogovtsev and Mendes [5], SF networks with different γ values can be generated by including the ages of the nodes in the Bárabasi and Albert's SF model, i.e., the probability that a newly added node will connect with an existing i^{th} node is now given by

$$p_i = \frac{k_i \tau_i^{-\alpha}}{\sum_j k_j \tau_j^{-\alpha}}. \tag{1.2}$$

Here k_i and τ_i are the degree and the age of the i^{th} node, respectively. The parameter $\alpha = -100, 0, 1$ corresponds to $\gamma \approx 2, 3, \infty$, respectively.

1.3 Identical Phase Oscillators

In their remarkable work in 2002, Barahona and Pecora [6] found that the linear stability of a synchronized state of an identical population can be determined from the eigenvalues of the Laplacian matrix. Their finding is applicable to a model given by

$$\dot{x}_i = F(x_i) + \sigma \sum_{j=1}^{N} A_{ij}(H(x_j) - H(x_i)), \tag{1.3}$$

where $i = 1, 2, \ldots, N$. Here x_i denotes the dynamical variable of an i^{th} oscillator and in general it can be a m dimensional vector. $F(x_i)$ represents the isolated dynamics of the i^{th} node. H is an arbitrary coupling function and it is same for all the oscillators. σ represents the coupling strength among the oscillators. And lastly, A_{ij} is an element in the i^{th} row and j^{th} column of an adjacency matrix A. $A_{ij} = 1$ if the nodes i and j are connected and 0 otherwise. Now, the Laplacian matrix is defined as $L_{ii} = D_{ii}$ if $i = j$, and $L_{ij} = -A_{ij}$ if $i \neq j$, where $D_{ii} = \sum_{k=1}^{N} A_{ik}$. In terms of the Laplacian matrix, Eq. (1.3) can be rewritten as

$$\dot{x}_i = F(x_i) - \sigma \sum_{j=1}^{N} L_{ij} H(x_j). \tag{1.4}$$

Eq. (1.4) shows that, irrespective of σ value, a globally synchronized state $x_i(t) = s(t)\ \forall\, i$ exists for the oscillators. Now, we perform a linear stability analysis for this state. We give a small perturbation to each oscillator such that, for an i^{th} node, $s(t) \to s(t) + \varepsilon_i$. The Taylor expansion of Eq. (1.4) around the synchronous state, with considering only the first order terms in ε_i, leads to

$$\dot{\varepsilon}_i = DF(s)\varepsilon_i - \sigma DH(s) \sum_{j=1}^{N} L_{ij} \varepsilon_j, \tag{1.5}$$

where $DF(s) = \frac{dF(x_i)}{dx_i}\big|_{x_i = s}$ and $DH(s) = \frac{dH(x_i)}{dx_i}\big|_{x_i = s}$. Note that ε_i in Eq. (1.5) depends on the ε_j values from its neighbors, which makes its integration with time very difficult or impossible. Therefore, we need to decouple the system of equations represented by Eq. (1.5). It can be written in a short form as

$$\dot{\varepsilon} = DF(s)\varepsilon - \sigma DH(s) L \varepsilon, \tag{1.6}$$

where ε is a column vector containing all ε_i and L is the Laplacian matrix. As shown in Ref. [7], let say a transformation from the vector ε to a vector η is such that

$$\varepsilon = E\eta, \tag{1.7}$$

where E is a matrix whose columns contains the eigenvectors of the Laplacian eigenvalues. Putting Eq. (1.7) in Eq. (1.6), we get

$$E\dot{\eta} = DF(s)E\eta - \sigma DH(s) L E \eta. \tag{1.8}$$

Now, we apply E^{-1} on Eq. (1.8). From linear algebra we know that $E^{-1}LE$ is nothing but a diagonal matrix with diagonal elements containing the Laplacian eigenvalues.

Therefore, an i^{th} entry of Eq. (1.8) is given by

$$\dot{\eta}_i = \{DF(s) - \sigma\lambda_i DH(s)\}\eta_i. \tag{1.9}$$

Eq. (1.9) depicts that the coordinates η_i are now decoupled. Since the sum of elements in each row of the Laplacian matrix is zero, $(1, 1, \ldots, 1)$ is an eigenvector with eigenvalue $\lambda_1 = 0$. Also, there is only one zero eigenvalue if the network is connected. Moreover, the Laplacian matrix is positive semi-definite, which makes all the eigenvalues non-negative. Therefore, the eigenvalues can be arranged as $\lambda_N > \lambda_{N-1} > \quad . \quad . \quad . \quad > \lambda_2 > \lambda_1 = 0$. Eq. (1.7) hints that for the synchronous state to be stable all other η_i, except η_1, should decay with time as $t \to \infty$. Following Eq. (1.9), Barahona and Pecora found that the synchronous state is stable if $\lambda_N/\lambda_2 < \alpha_2/\alpha_1$, where α_1, α_2 are determined by the dynamics on a network. The σ range over which the synchronous state is stable comes out to be $\alpha_1/\lambda_2 < \sigma < \alpha_2/\lambda_N$. Therefore, the smaller is the λ_N/λ_2 value, the wider is the σ range over which the synchronous state is stable, or we say that the global synchronizability (GS) has increased.

The model represented by Eq. (1.3) relates to many real-world systems; for example, electric circuits (such as Chua, Rossler like, Lorenz like, and master-slave circuits), laser arrays, neural networks, and stable biological systems, etc., [8].

1.4 Non-identical Phase Oscillators

Wiener was probably the first whose attempts to understand the emergence of collective behavior in connected units attracted significant attention [9, 10]. Later on, Winfree proposed a model of non-identical phase oscillators and derived some important conclusions regarding the synchronization of oscillators [11, 12]. Inspired by Winfree's observations, the next breakthrough step was taken by Kuramoto. From nearly identical and weakly coupled limit cycle oscillators, he derived a phase reduced form and used *sine* function for the coupling terms [13]. Angular velocity of an i^{th} oscillator in his all-to-all coupled model is given by

$$\dot{\theta}_i = \omega_i + \frac{\sigma}{N}\sum_{j=1}^{N}\sin(\theta_j - \theta_i), \tag{1.10}$$

where $i = 1, 2, \ldots, N$. ω_i represents the natural frequency of the i^{th} oscillator, and it can be drawn from a probability distribution function $g(\omega)$. If $\bar{\omega}$ represents the mean value of the natural frequencies, then by a change of coordinates such that $\phi_i = \theta_i - \bar{\omega} t$ we can move to a frame rotating with the velocity $\bar{\omega}$. All we have done is that each ω_i is now replaced by $\omega_i - \bar{\omega}$. This transformation leaves the model unchanged; therefore, we can always set $\bar{\omega} = 0$. σ represents the coupling strength, and, in the limit $N \to \infty$, the factor $1/N$ makes the coupling range independent to the network size. Furthermore, Kuramoto used the following equation to measure the phase coherence among the oscillators

$$re^{i\psi} = \frac{1}{N} \sum_{j=1}^{N} e^{i\theta_j}, \tag{1.11}$$

where $0 \leq r \leq 1$. The minimum value 0 corresponds to a uniform distribution of the oscillators over a circle of unit radius, while the maximum value 1 corresponds to the exact phase synchronization (i.e., $\theta_i = \theta \; \forall \; i$). With the help of Eq. (1.11), Eq. (1.10) can be re-written as

$$\dot{\theta}_i = \omega_i + \sigma r \sin(\psi - \theta_i). \tag{1.12}$$

Eq. (1.12) reveals that each oscillator is pulled by ψ and the coupling wants the oscillators to rotate with a velocity determined by $\dot{\psi}$. Also, the effective coupling strength is σr now. The higher is the phase coherence among the oscillators, the stronger will be the effective coupling strength. Since ψ is the mean value of the phases, i.e., $\psi = \tan^{-1}\left\{\frac{\sum_{j=1}^{N} \sin(\theta_j)}{\sum_{j=1}^{N} \cos(\theta_j)}\right\}$, the approach to deal with Eq. (1.10) in terms of r and ψ is called the mean-field analysis. Now, Kuramoto took a symmetric natural frequency distribution, i.e., $g(-\omega) = g(\omega)$. In the limit $N \to \infty$, using the facts that r and $\dot{\psi}$ remain constant in time after a sufficient time is passed, he found that synchronized oscillators rotate with a velocity $\dot{\theta}_i = \dot{\psi} = \bar{\omega} = 0$. Therefore, the synchronized or locked oscillators satisfy the relation

$$\sin(\psi - \theta_i) = -\frac{\omega_i}{\sigma r}. \tag{1.13}$$

Since $|\sin(\psi - \theta_i)| \leq 1$, the locked oscillators must satisfy the relation $|\omega_i| \leq \sigma r$, while those not following this criteria keep drifting around the circle. It turns out that, in the limit $N \to \infty$, we can neglect the drifting oscillators and Eq. (1.11) can be rewritten as [14]

$$r = \sigma r \int_{-\pi/2}^{\pi/2} \cos^2\theta \, g(\sigma r \sin\theta)\, d\theta. \tag{1.14}$$

Solving Eq. (1.14), Kuramoto found that the critical coupling for the onset of the synchronized state comes out to be $\sigma_c = \frac{2}{\pi g(0)}$.

1.4.1 Phase-shifted Kuramoto Oscillators

In the previous Section, we discussed Kuramoto oscillators in which the coupling terms contained only a difference of phases. The oscillators in the model synchronize at a common frequency which is determined by $\bar{\omega}$. However, in many real-world systems resembled by the Kuramoto oscillators, the synchronized frequency turns out to be different than $\bar{\omega}$. In 1962, Sakaguchi and Kuramoto [15] proposed that introduction of a phase shift in the coupling terms can change the synchronized frequency from $\bar{\omega}$. The angular velocity of an i^{th} oscillator in phase-shifted Kuramoto oscillators is given by

$$\dot{\theta}_i = \omega_i + \frac{\sigma}{N} \sum_{j=1}^{N} \sin(\theta_j - \theta_i + \alpha), \tag{1.15}$$

where $i = 1, 2, \ldots, N$ and $0 \leq \alpha \leq 2\pi$. It is useful to discuss the effect of α on the synchronization properties of the oscillators. For that, we consider a Lorentzian natural frequency distribution given by

$$g(\omega) = \frac{\gamma}{\pi((\omega - \bar{\omega})^2 + \gamma^2)}. \tag{1.16}$$

As in Section 1.4, $\bar{\omega}$ in Eq. (1.16) determines the mean of the natural frequencies, and γ determines the half-width at the half maxima. Using the Ott-Antonsen ansatz in the limit $N \to \infty$ [16], two equations governing the time evolution of r and ψ can be obtained. These equations (see Eq. 125 of Ref. [17]) are given as

$$\dot{r} = \frac{\sigma \cos\alpha \; r(1 - r^2)}{2} - \gamma r, \tag{1.17a}$$

$$\dot{\psi} = \bar{\omega} + \frac{r \sin\alpha (1 + r^2)}{2}. \tag{1.17b}$$

In the steady state, we have $\dot{r} = \dot{\psi} = 0$. Therefore, from Eq. (1.17a), we get either $r = r_1 = 0$ or $r = r_2 = \sqrt{1 - \frac{2\gamma}{\sigma \cos(\alpha)}}$. Note that $\cos(\alpha) > 0$ for $0 \leq \alpha < \pi/2$ and $3\pi/2 < \alpha \leq 2\pi$, while $\cos(\alpha) < 0$ for $\pi/2 < \alpha < 3\pi/2$. Now, if $\sigma > 0$, $\gamma > 0$, and $\cos(\alpha) < 0$, we get $r_2 > 1$, which is not possible; therefore, r_2 can not be a solution for $\pi/2 < \alpha < 3\pi/2$. Furthermore, the minimum coupling value at which r_2 can exist is $\sigma_c = 2\gamma/\cos(\alpha)$. This relation manifests that a change in $\alpha \to \pi(3\pi)/2$ delays or suppress the onset of synchronization. Since the coefficient of $\sum_{j=1}^{N} \sin(\theta_j - \theta_i)$ is negative for $\pi/2 < \alpha < 3\pi/2$, an increase in $\sigma \to \infty$ repels the connected pairs at π distances, suggesting that $r = 0$ should be a solution for these α values. The same can also be verified from the linear stability analysis. Giving a small perturbation to the fixed point $r^* = 0$ such that

$r^* \to r^* + \varepsilon$ and taking only the first order terms in ε while the Taylor expansion of Eq. (1.17a), we get

$$\dot{\varepsilon} = \left(\frac{\sigma\cos\alpha}{2} - \gamma\right)\varepsilon. \tag{1.18}$$

$\dot{\varepsilon}$ is negative for $\pi/2 \leq \alpha \leq 3\pi/2$; therefore, $r = 0$ is a stable solution for these α values.

1.4.2 Kuramoto Oscillators on Complex Topologies

As we saw in Sections 1.1 and 1.2.4, real-world networks are irregular or complex in topology. Ref. [12] discuss that a generalization of the Kuramoto oscillators from the globally connected topology to a general network topology can be made by incorporating the adjacency matrix A in the coupling terms. The angular velocity of an i^{th} oscillator is thus given by

$$\dot{\theta}_i = \omega_i + \sigma \sum_{j=1}^{N} A_{ij} \sin(\theta_j - \theta_i), \tag{1.19}$$

where $i = 1, 2, \ldots, N$. The description of σ, ω_i and A_{ij} is the same as mentioned earlier.

1.4.3 Examples of Kuramoto oscillators

Undoubtedly, due to our ability to apply the mathematical tools on them, the Kuramoto oscillators have enjoyed enormous attention in our attempts to understand the collective behavior of coupled dynamical units; nevertheless, the simple phase model also resembles several real-world systems. The review article by Acebrón *et al.* [18] presents that the oscillators relate to laser arrays, power grids, biologically oriented models, associative memory models, charge density waves, and chemical oscillators, etc. Similarly, the phase-shifted variant of Kuramoto oscillators is shown to resemble the Wein-bridge oscillators [19], Josephson-junction arrays, non-resonant interactions in ensembles of phase oscillators, power systems with nontrivial transfer conductance, mechanical rotors, complex Ginzburg–Landau equation, contrarian interactions, and nonlinear quantum networks with interacting qubits [20].

1.5 Relation Between λ_2 and Kuramoto Oscillators

Since we investigate Laplacian eigenvalues and Kuramoto oscillators in detail, it will be useful if we can apply the findings from one model to the other one. For an identical population, i.e., for $\omega_i = 0 \; \forall \; i$, Eq. (1.19) becomes

$$\dot{\theta}_i = \sigma \sum_{j=1}^{N} A_{ij} \sin(\theta_j - \theta_i). \tag{1.20}$$

Eq. (1.13) or the relation $|\omega_i| \leq \sigma r$ suggests that a globally synchronized state (in which $\theta_i = \theta \; \forall \; i$) exists for the identical population for every $\sigma > 0$. When the oscillators are about to reach this state, we can approximate $\sin(\theta_j - \theta_i) \approx \theta_j - \theta_i$. Therefore, Eq. (1.20) can be rewritten as

$$\dot{\theta}_i = -\sigma \sum_{j=1}^{N} L_{ij} \theta_j. \tag{1.21}$$

In terms of normal modes (ψ_j), the solution of Eq. (1.21) is given by [12]

$$\theta_i(t) = \sum_{j=1}^{N} E_{ij} \psi_{j(t=0)} e^{-\sigma \lambda_j t}. \tag{1.22}$$

Here E_{ij} represents an entry of the i^{th} row and j^{th} column of the E matrix defined in Eq. (1.7). Note that the j^{th} column contains the eigenvector corresponding the Laplacian eigenvalue λ_j. Since λ_2 is the smallest nonzero eigenvalue of the Laplacian, Eq. (1.22) demonstrates that the time taken by the oscillators to reach to the synchronized state is determined by λ_2. The higher is λ_2, the smaller is the time taken by the oscillators to reach to the steady state.

1.6 Why Multiplex Networks?

If we ask ourselves, does a group of interacting elements has only one type of interaction among them? The answer is certainly ”No.” Real-world examples indicate that interactions in many networks are interdependent, in the sense that the functioning of one type of interaction affects the functioning of other types of interactions [21]. Often cited example comes from social networks in which a group of people can interact with each other through different means, i.e., either through physical interactions or through virtual interactions (Facebook, Twitter, WhatsApp, etc.). In the neural system of *Caenorhabditis elegans*, two neurons can communicate either through electrical signals (which propagate through synapses and neuronal dendrites) or through the diffusion of ions and small molecules (which travel through intercellular channels called gap junctions) [22]. The different types of interactions (excitatory and inhibitory) among neurons in the human brain have also been described as a network of multiple layers

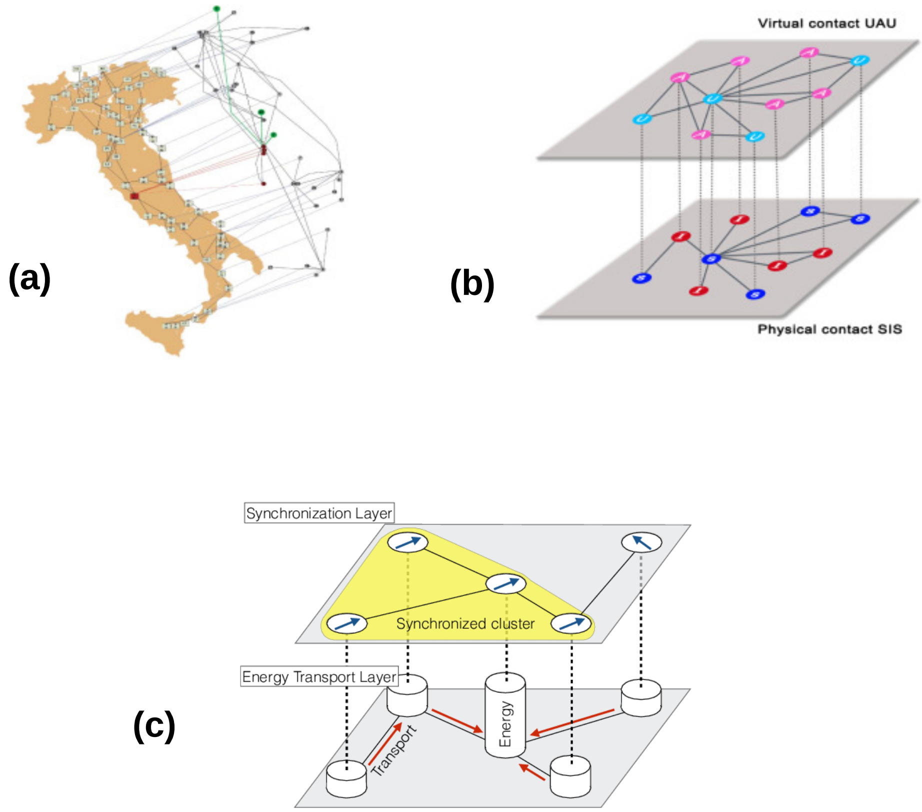

Figure 1.1: The Schematic diagrams represent multiplex networks where each layer contains one type of interaction. (a) The multiplex network of power stations and internet servers [24]. (b) The multiplex network of physical and virtual interactions in social networks [25]. (c) The multiplex network of energy and synchronization layers for neural networks [26].

[23]. The multilayer characteristic of the networks justifies the cascading of failures in power grid networks in Italy which occurred on 28 September 2003 [24]. It happened that the failure of the power grid network led to the failure of the internet communication network, which in turn further led to the failure of power stations. The spreading of a disease in social networks can be controlled by the spread of awareness among people [25]. A two-layer multiplex network in which one layer represents energy flow across different regions of the human brain and the other layer represents synchronization among the neurons enlights our understanding of how the two dynamical processes affect each other [26]. The speed of a diffusion process on multiplex networks can be very different than the corresponding single networks [27]. The impact of spread in information on opinion formation [28], the functioning of different brain regions [29], the response of a network to a random or a targeted attack [30], congestion of flow in

transport networks [31] have all been examined on the novel multiplex networks and the effects of the multiplex framework have been investigated. Protein interactions, airline networks, scientific publication networks, and movies in the Internet Movie Database (IMDb) are some more examples where the multiplex framework has been applied [22]. All these examples suggest that the traditional approach of treating all types of interactions on the same foot is certainly not an exact representation of these systems. Therefore, it has been realized that each type of interaction should be assigned to a separate layer of a multilayer or multiplex network. The latter is a particular form of the first in which each node is replicated in all the layers; also, they are connected with themselves across the layers. The copies of a node in different layers are called its mirror nodes.

1.7 Kuramoto Oscillators on Multiplex Networks

In different works, a multiplex network has been realized through different means. For example, Zhang *et al.* [32] constructed a two-layer network by multiplying the local order parameter of an i^{th} node in layer a with the intralayer coupling terms of its mirror node in layer b. Nicosia *et al.* [26] constructed a multiplex network of random walkers and Kuramoto oscillators such that a random walker in one layer affects the natural frequency of its mirror node in another layer. As hinted by Fig. 1.1 in Section 1.6, another simple way to construct a multiplex network is to put links between mirror nodes in all the layers. For instance, a two-layer multiplex network of Kuramoto oscillators can be realized by

$$\dot{\theta}_i^a = \omega_i^a + \frac{\sigma^a}{N}\sum_{j=1}^{N}\sin(\theta_j^a - \theta_i^a) + \lambda\sin(\theta_i^b - \theta_i^a), \tag{1.23a}$$

$$\dot{\theta}_i^b = \omega_i^b + \frac{\sigma^b}{N}\sum_{j=1}^{N}\sin(\theta_j^b - \theta_i^b) + \lambda\sin(\theta_i^a - \theta_i^b). \tag{1.23b}$$

Here $\theta_i^{a(b)}$ and $\omega_i^{a(b)}$ represent the phase and natural frequency of the i^{th} oscillator in layer $a(b)$. $\sigma^{a(b)}$ represents intralayer coupling among the nodes of layer $a(b)$, and λ represents interlayer coupling strength. The interlayer coupling terms try to synchronize the mirror nodes. Furthermore, a multiplex network of two layers having complex topologies can be constructed by replacing the intralayer coupling terms in Eqs. (1.23a) and (1.23b) by $\sigma^{a(b)}\sum_{j=1}^{N}A_{ij}^{a(b)}\sin(\theta_j^{a(b)} - \theta_i^{a(b)})$. We have $A_{ij}^{a(b)} = 1$ if i and j^{th} nodes are connected in layer $a(b)$ and zero otherwise.

It will be useful to mention here the globally synchronous state for the multiplex networks. In this state, we have $\dot{\theta}_i^{a(b)} = \dot{\theta} \; \forall \; i$. Therefore, summing Eqs. (1.23a) and (1.23b) for all the $2N$ oscillators leads to $\dot{\theta} = \bar{\omega}$, where $\bar{\omega} = \frac{1}{2N}\sum_{j=1}^{N}(\omega_j^a + \omega_j^b)$. Since we can always take $\bar{\omega} = 0$, the globally synchronous state is always a fixed point state, provided that all the coupling terms contain only a difference of phases.

The degree of phase coherence among the oscillators in layer $a(b)$ is measured using an order parameter given by

$$r^{a(b)} e^{i\psi^{a(b)}} = \frac{1}{N}\sum_{j=1}^{N} e^{i\theta_j^{a(b)}}, \tag{1.24}$$

where $0 \leq r^{a(b)} \leq 1$. The minimum and the maximum values are obtained for the cases discussed after Eq. (1.11). The nature of the phase transition—continuous or discontinuous—is determined by plotting the time-averaged $r^{a(b)}$ with respect to σ^a or σ^b.

1.8 Discontinuous Phase Transitions or Explosive Synchronization

The word "phase transition" refers to a change in some state of a system being studied as a result of a change in some control parameter. Real-world is full of phase transitions; for example, melting of ice to water, the transition of metals from a normal state to a superconducting state, Bose-Einstein condensation, appearance of a permanent magnetic moment in a ferromagnet, etc., are some of the celebrated examples which attract significant attention in physical science. Surprisingly, the common thing in all these examples is that a system undergoes a transition from a disordered state to an ordered state or vice versa. While the majority of the phase transitions in real systems are continuous and reversible, a few of them can be discontinuous with irreversibility. By reversible we mean that the same state of the system can be observed by reversing the direction of the control parameter. Some of examples from the continuous phase transitions are melting of ice, boiling of water, and super-cooling or super-heating transitions; while ferromagnetic transitions, superconducting transitions, and superfluid transitions come from the discontinuous phase transitions [33]. In network science also, the coupled dynamical units usually exhibit a smooth and reversible transition from an incoherent state

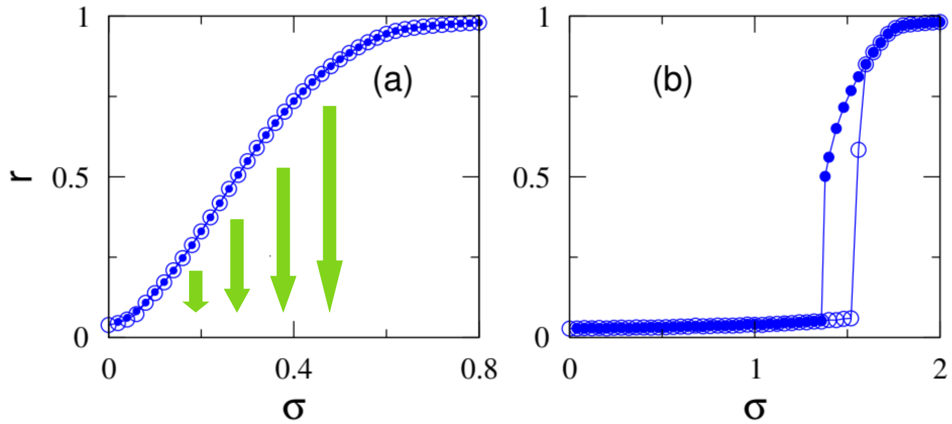

Figure 1.2: The schematic diagrams in (a) and (b) present that suppression of synchronization changes a continuous phase transition to a discontinuous one. x and y axis represent coupling σ and the phase order parameter r. The lines with open and filled circles correspond to the forward and backward continuation of σ.

to a coherent or synchronized state, while in special cases it can be discontinuous and irreversible as well [33, 34]. The latter is also called explosive synchronization (ES). Irreversibility or a hysteresis appears when the final phases at a coupling value are used as initial phases at the next coupling value. It happens that, for continuous phase transitions, a synchronized state is globally stable, i.e., any initial condition will lead to the same synchronized state. However, when the phase transition is discontinuous, the synchronous state is locally stable in the bistable regime, i.e., only those initial conditions which are close to the synchronized state will reach it. As a consequence of this, we get a hysteresis. While a hysteresis appears in most of the discontinuous phase transitions, discontinuity without a hysteresis is also possible [35]. Through extensive analytical and numerical calculations [33,34], it has been realized that any strategy which can suppress the gradual increase in the phase coherence will eventually propel the ensemble towards the ES (Fig. 1.2).

Although the discontinuous phase transitions look very attractive due to the bistability, they are undesired in many real situations. It has been found that while some amount of synchronization among neurons is necessary for the proper functioning of the human brain, an abrupt transition to synchronization may lead to epileptic seizures [36]. Similarly, abrupt episodes of chronic pain in the Fibromyalgia human brain [37] and abrupt cascading of failures in power-grid networks [24] are also unwanted. A few experiments have also been performed to show the presence of ES; for instance, ES in mercury-beating heart oscillators [38] and chaotic oscillators [39]. We hope that, from fundamental understanding to biological applications [40, 41] perspective, it is worthy to explore the discontinuous phase transitions in detail, their underlying causes, and different parameters governing the hysteresis size.

1.8.1 A Survey of Some Important Results on ES

While the research on ES might start a long time back, here we review some important techniques or results from recent years that give birth to ES in Kuramoto oscillators. It has been found that degree frequency correlations [42], frequency-weighted couplings [43–45], adaptive coupling [32, 46], disorder in natural frequencies [47], repulsive coupling [48], and higher-order interactions in the coupling [49] are some of the popular techniques for generating ES in Kuramoto phase oscillators. In almost all of these works, it has been witnessed that the suppression of synchronization eventually leads to ES. A few works have extended ES to multilayer and multiplex networks as well. For example, ES in multiplex networks due to intra or interlayer adaptive coupling [50–52], intertwined coupling [26], inertia [53], repulsive coupling [54], and time-delayed coupling [55], etc.

1.9 A Few Questions This Thesis Revolves Around

This thesis can be seen as investigating two broad questions. The first question one would probably ask while constructing a multiplex network is how to put interlayer connections? And if there is any correlation among the mirror nodes, what is its impact on the synchronization properties of coupled dynamical elements? Secondly, what are different techniques using which one can turn a continuous phase transition on multiplex networks into a discontinuous one or vice versa? What are the underlying causes behind the origin of ES, and what factors govern the width of associated hysteresis, if any?

1.10 Organization of the Thesis

Chapter 2 presents the impact of degree-degree correlations among the intralayer and mirror nodes on the GS of identical phase oscillators on multiplex networks. We show that the degree-degree correlations have a profound impact on the GS, enabling the specification of synchronization by only changing the degree-degree correlations among the mirror nodes while maintaining the connection architecture of the individual layers unaltered. Furthermore, in contrast to single networks where increasing connections always increases the GS of the networks, the multiplex networks may exhibit strange synchronization behavior as determined by degree-degree correlations among the intralayer and mirror nodes.

Chapter 3 presents ES in adaptively coupled multiplex networks. We show that an introduction of adaptation in interlayer links of a two-layer multiplex network of Kuramoto oscillators triggers ES in the layers. The ES emerges along with a hysteresis, and the parameters governing the width of hysteresis are discussed. The robustness of ES against changes in the network topology, natural frequency distribution, and the adaptive scheme is tested. Finally, a rigorous mean-field analysis is provided to support the numerical results.

Chapter 4 presents ES in interlayer phase-shifted multiplex networks. We show that an interlayer phase shift α, with $0 \leq \alpha \leq \pi/2$, can induce ES in a two-layer multiplex network of Kuramoto oscillators. We explore the different factors which govern the hysteresis width. The robustness of ES against changes in the network topology and natural frequency distribution is tested. A mean-field analysis is performed to justify the numerical results. Finally, taking a suggestion from the synchronized state of the multiplex networks, we extend the results to classical single networks in which some specific links are assigned the phase-shifted interactions.

Chapter 5 presents ES in frequency displaced multiplex networks. We demonstrate that a sufficient natural frequency mismatch between two layers of a multiplex network can turn a continuous phase transition into a discontinuous one. The observed phenomenon exists only for a specific arrangement of intra and interlayer couplings. The robustness of ES against changes in network topology, average connectivity, and the number of interlayer links is tested. Finally, the minimum coupling value at which the transition to desynchronization occurs is derived theoretically.

Chapter 6 discusses some important outcomes, limitations, and possible extensions of the results from this thesis.

Chapter 2

Degree-degree Correlations Determine the Synchronizability of Multiplex Networks

2.1 Introduction

Real-world data shows that nodes in networks are not connected randomly with each other. In fact, in many networks, similar or dissimilar degree nodes connect preferentially with each other. Networks where similar (dissimilar) degree nodes are connected with preference are also called assortative (disassortative) networks [56]. For instance, social networks in which people of same age, nationality, education level, religion, or language prefer to interact with each other are assortative, while technological and biological networks are disassortative [56, 57]. The presence of degree-degree correlations in networks plays an important role in the network resilience and spreading of a disease on them [57]. The impact of degree-degree correlations on the global synchronizability (GS) of single networks has already been investigated [58]. It has been found that an increase in disassortativity is beneficial for the GS of the identical oscillators represented by Eq. (1.3). These correlations have also been shown to affect the robustness and controllability of single networks as well as multilayer or multiplex networks [56,57,59,60] (see Fig. 2.1 for schematic diagrams). A few other recent works have demonstrated the effect of degree-degree correlations on various emerging phenomena such as the giant component [61] and disease spreading [62] on multiplex networks.

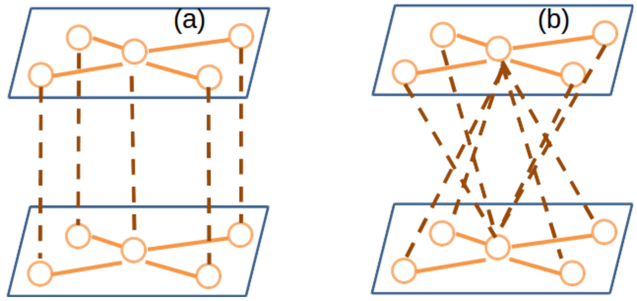

Figure 2.1: The schematic diagrams depict the architecture of multilayer networks in which interlayer degree-degree correlations are (a) assortative and (b) disassortative.

The first question that would pop up naturally in one's mind while thinking about multiplex networks is how to put interlayer links among the mirror nodes, and if there is any correlation in the degrees of mirror nodes, what is its impact on the GS of an identical population? With this motivation, in this Chapter we investigate the role of degree-degree correlations, intralayer as well as interlayer correlations, on the GS of identical phase oscillators on multiplex networks. Throughout the Chapter or the thesis, interlayer degree-degree correlations are also referred as degree-degree correlations among the mirror nodes.

2.2 Theoretical Framework

We consider identical phase oscillators with diffusive coupling on a multiplex network of two layers. The state variable of an i^{th} oscillator evolves with time such that

$$\dot{x}_i = F(x_i) + \sigma \sum_{j=1}^{N} A_{ij}(H(x_j) - H(x_i)). \tag{2.1}$$

The parameters F, σ and H are the same as discussed earlier in Section 1.3. A_{ij} is an element in the i^{th} row and j^{th} column of an adjacency matrix A, which can be represented as

$$A = \begin{pmatrix} A^1 & I \\ I & A^2 \end{pmatrix}. \tag{2.2}$$

Here $A^{1(2)}$ is an adjacency matrix of size $\frac{N}{2} \times \frac{N}{2}$ containing the topology of layer $a(b)$; I is an identity matrix of the same size as $A^{1(2)}$, and it represents the interlayer links. $A_{ij} = 1$ if the nodes i and j are connected and 0 otherwise.

The degree-degree correlation coefficient r is defined as [56]

$$r = \frac{\left\{\frac{1}{N_c}\sum_{i=1}^{N_c} j_i k_i\right\} - \left\{\frac{1}{N_c}\sum_{i=1}^{N_c}\frac{(j_i+k_i)}{2}\right\}^2}{\left\{\frac{1}{N_c}\sum_{i=1}^{N_c}\frac{(j_i)^2+(k_i)^2}{2}\right\} - \left\{\frac{1}{N_c}\sum_{i=1}^{M}\frac{(j_i+k_i)}{2}\right\}^2}, \tag{2.3}$$

where j_i and k_i are the degrees of the nodes connected by an i^{th} link. N_c represents the total number of links in the network. Note that $-1 \leq r \leq 1$, the minimum and the maximum values correspond to a highly disassortative and assortative network. Throughout the Chapter, intralayer degree-degree correlations are represented by r_{intra}, while interlayer or degree-degree correlations among the mirror nodes are denoted by r_m. To vary r_{intra}, two links of a network are chosen randomly together with their adjacent nodes. The nodes are ranked according to their degrees, and they are reconnected based on their degrees in an assortative or disassortative manner with a probability p. For example, to construct an assortative network, out of the four nodes, the higher degree nodes are reconnected among themselves and the remaining lower degree nodes are reconnected among themselves with the probability p. Similarly, for constructing a disassortative network, the highest degree node is reconnected with the lowest degree node and the other two nodes are reconnected among themselves. Networks of different r_{intra} values are generated by varying the parameter p [63]. One can also change r_m values by following the same procedure. Note that after the rewiring of the interlayer links, we can always renumber the nodes in the two layers without changing any physical significance; therefore, the use of identity matrix I for interlayer links in Eq. (2.2) is valid.

2.3 Degree-degree Correlations Determine the GS

To show the impact of r_m and r_{intra} on the GS of the identical phase oscillators, we consider a multiplex network in which the layers represent Barabási and Albert's SF networks. We find that, for moderate r_{intra} values, decreasing r_m value leads to a decrease in λ_N/λ_2 value, and consequently, the GS of the multiplex network increases (Figs. 2.2(b) and 2.2(c)). The phenomenon can be related to the poor synchronization due to the overloading of the oscillators [64]. Going by the same analogy, the more concentrated the traffic is on the mirror nodes (i.e., when the mirror degrees are assortative), the less robust is the whole network in maintaining its synchronous state, leading to reduced GS. A prevalence of mirror nodes having disassortative degree-degree correlations is thus beneficial for synchronization on the multiplex networks. Remember

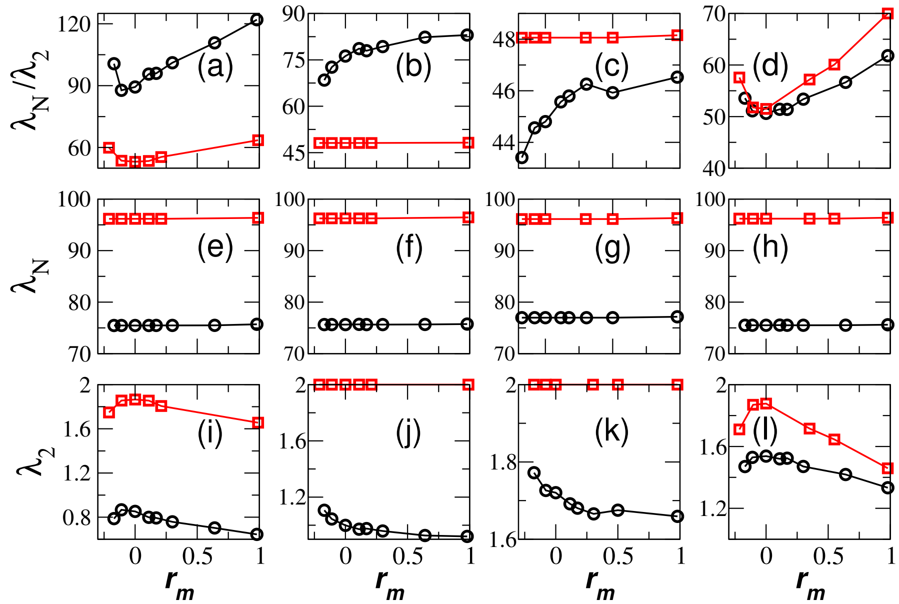

Figure 2.2: (a)-(d), (e)-(h), and (i)-(l) represent changes in λ_N/λ_2, λ_N, and λ_2 with r_m for a multiplex network of different intralayer degree degree correlations. Layers 1 and 2 are SF networks of 500 nodes. The circles represent $\langle k^1 \rangle = \langle k^2 \rangle = 6$, while the squares correspond to $\langle k^1 \rangle = \langle k^2 \rangle = 10$. Here $\langle k^{1(2)} \rangle$ denotes the average degree of layer 1(2). r_{intra} values in (a)-(c) are $r_{intra} = 0.20$, 0.10, -0.2, respectively. To demonstrate that strong intralayer degree-degree correlations are detrimental for GS, we consider $r_{intra} = -0.35$ (the circles) and -0.45 (the squares) in (d). The network parameters for each column of the second and third rows are the same as in the first one. Each data point is averaged over 20 network realizations.

that, if the two layers are connected through a few links only, connections between high degree nodes result in an enhanced synchronizability of the multilayer networks [65]. As realized in an earlier work on single networks [58], changing degree-degree correlations have no impact on λ_N. The present work also reflects that λ_N is constant with respect to changes in r_m values (Figs. 2.2(e)–2.2(h)); it is λ_2 that determines the relationship between GS and r_m. For all values of r_{intra}, Figs. 2.2(i)–2.2(l) exhibit a behavior of λ_2 which is completely in contrast to that of λ_N/λ_2. λ_2, also called the algebraic connectivity of a network, is a measure of the overall connectedness of the nodes in a network. Networks with high algebraic connectivity are difficult to break into disconnected components [1], and thus have better GS. The increase in GS with decreasing r_m, however, happens only for the case of multiplex networks which have moderate r_{intra} values (Figs. 2.2(b) and 2.2(c)). For layers having strong intralayer degree-degree correlations (for instance $r_{intra} = -0.35$ and 0.2), decreasing r_m value beyond a certain point (at around $r_m \approx 0$) proves detrimental for the GS (Figs. 2.2(a) and 2.2(d)). As shown by

Figs. 2.2(i) and 2.2(l), this is because the algebraic connectivity of the layers is affected adversely for strong intralayer degree-degree correlations [66], leading to such synchronization behavior. Note that as the r_{intra} value decreases, changes in λ_N/λ_2 become less significant with changing r_m (Figs. 2.2(a)–2.2(c)). Ref. [66] suggests that increasing disassortativity in a network decreases the diameter of the network; therefore, it can be inferred that the impact of r_m is stronger on multiplex networks having larger diameter or average path length.

Next, we investigate the impact of r_m on the GS of slight dense multiplex networks. For layers with average connectivity $\langle k^{1(2)} \rangle = 10$, the changes in the GS with r_m are invisible unless the layers have strong intralayer degree-degree correlations (the square symbols in Figs. 2.2(a)–2.2(d)). For strong intralayer correlations, the GS exhibits a similar behavior as observed earlier for average degree $\langle k^{1(2)} \rangle = 6$. Figs. 2.2(i)–2.2(l) demonstrate that λ_2 remains constant at 2, except for highly assortative or disassortative layers where it changes; therefore, changing r_m does not cause any change in the algebraic connectivity (and therefore GS) of dense multiplex networks. These observations suggest that changes in r_m may not show any impact on GS after a sufficient high average connectivity of the layers. Later on, from Fig. 2.5 we can check that this is infect correct.

2.4 Fiedler Vector and GS

To have an in-depth understanding of the relationship between the algebraic connectivity and mirror degree correlations, we investigate the eigenvector corresponding to λ_2, also referred as Fiedler vector [67]. The sign of the eigenvector entries can be used for partitioning the network into two disconnected components [1]. Using recursive bisection, one can further partition the network into more components. We construct a layer by joining a globally connected network with a ring network of the same size through a few links (say one). We multiplex this network with its replica as in Fig. 2.3, and vary r_m. An individual layer in this multiplex network is roughly similar to a highly assortative network in terms of edge connectivity, with very few links joining dense and sparse groups of the network.

For very high and very low r_m values, the eigenvector entries are very sparse around 0 (Figs. 2.4(a) and 2.4(c)), and thus making it possible to visualize the network con-

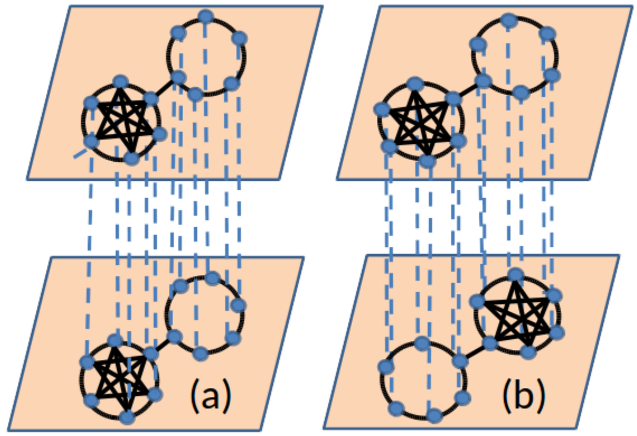

Figure 2.3: The schematic diagrams depict the architecture of a multiplex network in which layers have strong positive degree-degree correlations. (a) and (b) represent assortative and disassortative degree-degree correlations among the mirror nodes.

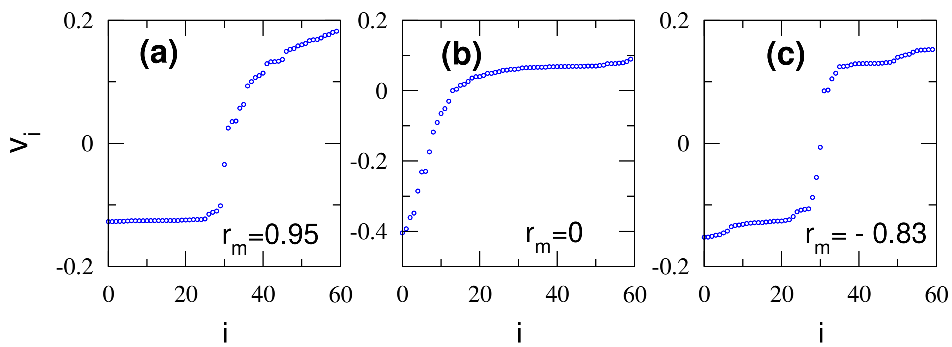

Figure 2.4: (a)-(c) present entries (v_i) of the eigenvector corresponding to the λ_2 eigen value for different r_m values. The number of nodes in both layers is 30 with topology given by Fig. 2.3. Here the nodes are renumbered based on their corresponding v_i values.

sisting of two loosely connected components. One set of nodes corresponds to positive eigenvector entries, while the other set leads to negative eigenvector entries. A close look at Fig. 2.4(a) reveals that half of the nodes have almost same magnitude of the corresponding eigenvector entries, suggesting that the dense parts of both the layers form one group, while the sparse parts form the other group. Similarly, Fig. 2.4(c) shows that eigenvector entries are symmetric around 0, suggesting that the dense part of one layer is accompanied by the sparse part of the other layer. Such partitioning, however, is not obvious in Fig. 2.4(b). Therefore, for highly assortative layers, strong correlations among the mirror nodes turn out to be detrimental for the GS. Note that strong disassortativity also leads to a decrease in the algebraic connectivity of a network [66]; hence, a similar analogy can be used to explain the changes in GS for highly disassortative layers as well.

2.5 Increasing Connectivity is Not Always Good for GS of Multiplex Networks

The multiplex networks manifest a much rich synchronization behavior than the single networks, which is not surprising as there exists another degree of freedom (r_m) associated with them. We find that in contrast to single networks where GS always increases with increasing $\langle k \rangle$ [66], the multiplex networks can exhibit an increase or decrease in GS as determined by r_{intra} values. The GS of single networks increases by a process that not only increases λ_N but also increases λ_2 as well [12, 66]; however, it is λ_2 that dominates the overall changes in λ_N/λ_2.

We find that for multiplex networks with positive r_{intra} values the GS exhibits an increase followed by a decrease (Figs. 2.5(a) and 2.5(b)). However, as r_{intra} value decreases, the GS can show an increase or decrease with an increase in $\langle k \rangle$ (Figs. 2.5(c) and 2.5(d)). The functionality of the GS with respect to $\langle k \rangle$ can be understood by tracing λ_N and λ_2 separately. For multiplex networks with assortative layers, the initial increase in GS is due to a significant increase in λ_2; Figs. 2.5(e) and 2.5(f) manifest that λ_2 increases from around 0.8, 1.2 to 2. It increases first and thereafter gets saturated, letting λ_N drive the overall changes in λ_N/λ_2. The minimum value of λ_N/λ_2 (or the maximum GS) marks the point where λ_2 saturates. Since the algebraic connectivity of the layers increases with increasing disassortativity (unless they are strong disassortative), so, if r_{intra} value is chosen such that λ_2 is already around its maxima, the increase in λ_N can dominate over the increase in λ_2. The same has happened in Fig. 2.5(c) as well. The role of r_m here is that changes in GS becomes more significant for a positive r_m value (Figs. 2.5(a), 2.5(b), and 2.5(d)), which is due to a slightly large increase in λ_2. The major contribution from the multiplex structure is to put a cap on the maximal value of λ_2 that can be achieved for a varying $\langle k \rangle$. In contrast, for single networks, λ_2 is proportional to $\langle k \rangle$, and its maximum value ($\lambda_2 = N$) is achieved only when the network is fully connected.

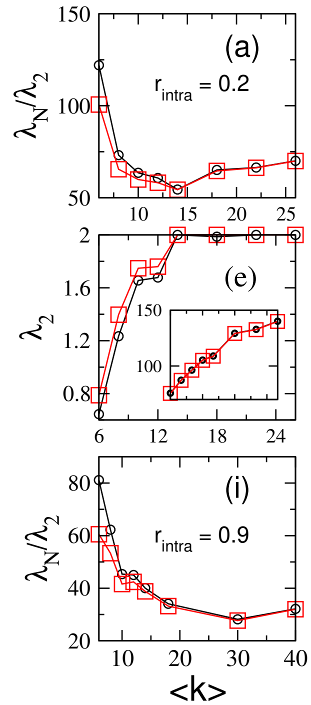

Figure 2.5: For different r_{intra} values, (a)-(d) and (e)-(h) show changes in λ_N/λ_2, λ_2 with $\langle k^1\rangle = \langle k^2\rangle = \langle k\rangle$. The insets show changes in λ_N with $\langle k\rangle$. The circles and the squares correspond to $r_m = 0.98$ and -0.17. The layers are SF networks of 500 nodes. (i)-(l) show changes in λ_N/λ_2 when the layers are ER networks. The circles, squares correspond to $r_m = 0.98, -0.98$.

2.6 Robustness of Results Against Change in Degree Distribution

So far we have presented the results for SF networks which are heterogeneous in degree distribution. Now, we investigate how a changes in the degree distribution alters the role of degree-degree correlations in determining the GS of multiplex networks. We find that homogeneous networks (ER networks) follow a similar synchronization behavior due to changes in r_{intra} and r_m as exhibited by the heterogeneous networks (SF networks) earlier. For moderately correlated layers, strong negative degree-degree correlations among mirror nodes lead to an increase in GS (Figs. 2.6(b)–2.6(e)); while for strongly correlated layers, neutral or small negative mirror degree correlations optimize the GS (Figs. 2.6(a) and 2.6(f)). ER networks show continuous decrease in λ_N/λ_2 even at $r_{intra} = \pm 0.6$ (Figs. 2.6(b) and 2.6(e)), while to find the same phenomenon in SF networks the range of r_{intra} values is small, i.e., 0.1 in Fig. 2.2(b) and -0.2 in Fig. 2.2(c).

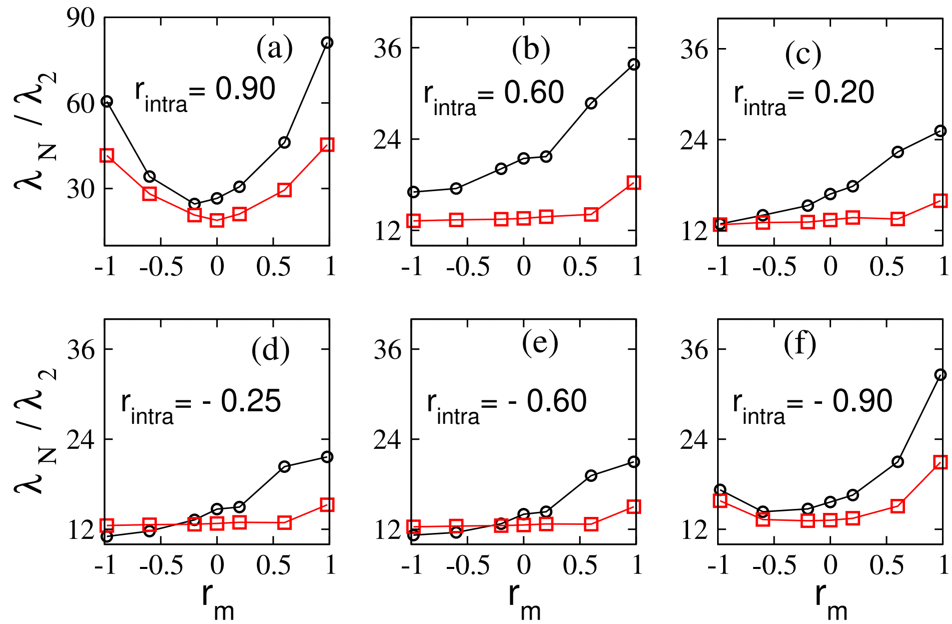

Figure 2.6: (a)-(f) depict variation in λ_N/λ_2 with respect to r_m for a multiplex network of ER layers. The number of nodes in both layers is 500. The circles and the squares correspond to $\langle k^1 \rangle = \langle k^2 \rangle = 6$, 10.

Requirement of high assortativity or disassortativity among the nodes to see a similar effect might be due to the homogeneous degree distribution as it is not easy to set apart the network into sparse and dense groups.

Lastly, we discuss the dependence of GS on the connectivity of the ER layers. Similar to the SF networks, here also, the GS may show an increase or decrease with increasing connectivity. For positive r_{intra} values approaching 1, the GS initially increases and then decreases with an increase in $\langle k \rangle$ value (Fig. 2.5(i)). However, if r_{intra} value decreases, the GS can decrease as well as determined by an r_m value (Figs. 2.5(j)–2.5(l)). Therefore, we conclude that the results obtained for SF networks are valid for ER networks as well.

2.7 Discussion

The flashing of fireflies, the ticking of clocks, the synchronized clapping of a large audience, and the pathologically synchronized firing of brain cells during an epileptic attack can all be modeled as networks of dynamical elements where coupling between the elements drives these systems towards synchronization [68]. Here we have investigated the GS of identical phase oscillators on the multiplex framework where the nodes are connected with preferential attachments. For multiplex networks with sparse layers, our observations reveal that, if the layers are moderately correlated, strong negative degree-degree correlations among mirror nodes lead to an increase in GS, while if the layers have strong correlations, moderate degree-degree correlations among the mirror nodes proved to be beneficial for GS. We also showed that, while increasing average degree, the degree-degree correlations determine whether λ_N or λ_2 will rule the overall changes in λ_N/λ_2. The GS of the multiplex networks, therefore, can increase or decrease. Remember that the eigenvalue λ_2 also determines the time taken by the identical Kuramoto oscillators to synchronize (Section 1.5) or the speed of a diffusion process [27]. Since λ_2 gets saturated after some average connectivity, our results indicate that more connections do not improve the speed of a diffusion process on multiplex networks.

Similar to the social network example in the single network framework (Section 2.1), it is very likely that a highly connected node in one layer will also be highly connected in other layers. For example, being a friendly person, a person who interacts with more people physically is likely to have high connectivity on social media platforms such as Facebook, WhatsApp, Twitter, or Instagram [61]. A city having more number of bus stations is likely to have more airports and railway stations [69]. We hope our findings will be crucial in our attempt to understand the collective behavior in complex systems having multiple types of interactions, i.e., the neural networks [26].

Chapter 3

Interlayer Adaptation Induced Explosive Synchronization in Multiplex Networks

3.1 Introduction

In many real-world networks, it is possible that coupling between connected dynamical units can change with time. The time-dependent coupling is also called adaptive coupling. Adaptation is an inherent feature in the construction of many complex systems. In neural networks, it has been found that a pair of neurons having a higher degree of synchronization are connected with stronger synaptic coupling as compared to those having weaker synchronization. This intelligence of the neurons is called Hebbian learning [52]. Adaptation in the neural networks explains learning or memory processes [70, 71].

Recently, Zhang *et al.* [32] proposed that a fraction of adaptively coupled phase oscillators on single networks gives birth to ES. Further, they have extended their results to a two-layer multilayer network of virtual interlayer links. The multilayer network in their model is realized by controlling the intralayer coupling strength in a layer through the local order parameters from the other layer [32]. Taking the same model, Danziger *et al.* [72] have further shown that ES can coexist with classical synchronization. A few recent studies on ES in multilayer networks have also adopted the adaptive coupling dynamics proposed by them [50, 51]. In this Chapter, we explore if interlayer adaption can also induce ES in a multiplex network. What are the properties of the ES, i.e., what factors govern the onset of ES and the hysteresis size?

3.2 Model

We consider a two-layer multiplex network of globally connected layers. Each layer contains N nodes, representing non-identical Kuramoto oscillators. As we discussed in Section 1.5, identical Kuramoto oscillators exhibit a globally synchronized state for all coupling values, so there is no transition from an incoherent state to a coherent state. Hence, for all works on ES, only non-identical Kuramoto oscillators will be examined. Each node in a layer is adaptively linked with its counterpart in another layer through an interlayer coupling strength, which is a function of phase coherence among nodes of the interacting layers. The time-evolution of phases of oscillators in layer $a(b)$ is ruled by

$$\dot{\theta}_i^a = \omega_i^a + \frac{\sigma}{N}\sum_{j=1}^{N}\sin(\theta_j^a - \theta_i^a) + \lambda r^a r^b \sin(\theta_i^b - \theta_i^a), \tag{3.1a}$$

$$\dot{\theta}_i^b = \omega_i^b + \frac{\sigma}{N}\sum_{j=1}^{N}\sin(\theta_j^b - \theta_i^b) + \lambda r^a r^b \sin(\theta_i^a - \theta_i^b), \tag{3.1b}$$

where $i = 1,2,3,\dots,N$. The parameters $\theta_i^{a(b)}$, $\omega_i^{a(b)}$, and $\sigma^{a(b)} = \sigma$ are the same as explained in Section 1.7. The initial phases, i.e., the phases at time $t = 0$, and the natural frequencies of oscillators in layer $a(b)$ are drawn from uniform random distributions in the range $-\pi \leq \theta_i^{a(b)} \leq \pi$ and $-\gamma \leq \omega_i^{a(b)} \leq \gamma$. Throughout this Chapter we take $\gamma = 0.5$. We mention that natural frequencies to oscillators in layer a and b are assigned randomly, i.e., $\omega_i^a \neq \omega_i^b$ in general. λ represents the static interlayer coupling strength, while $\lambda r^a r^b$ represents the adaptive interlayer coupling. The higher is the phase coherence among oscillators in both the layers, the stronger will be the interlayer coupling strength $\lambda r^a r^b$. Eqs. (3.1a) and (3.1b) are solved numerically using Runge-Kutta fourth order method with time step $dt = 0.01$. To determine the nature of the phase transition (continuous or discontinuous) in layer $a(b)$, the time-averaged $r^{a(b)}$ is plotted with respect to σ. The time average is performed for 10^5 steps after neglecting the initial 10^5 steps, which helps us to observe the steady-state behavior of the oscillators. Throughout the thesis—in the forward, backward continuation of the coupling—the phases at the final time step at a σ value are used as initial phases at $\sigma + d\sigma$, $\sigma - d\sigma$, respectively.

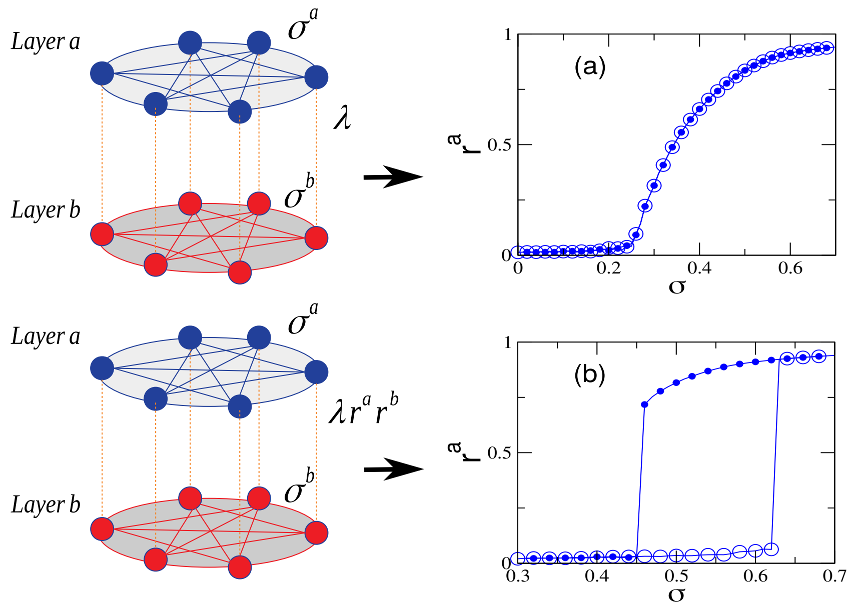

Figure 3.1: (a) Static interlayer coupling λ leads to a continuous phase transition in a multiplex network, while (b) adaptive interlayer coupling $\lambda r^a r^b$ leads to ES. Two different type of transitions (r^a vs σ) are shown in (a) and (b) for a multiplex network of two globally connected layers. Here $N = 5000$ and $\lambda = 0.5$. In all plots showing r^a (or r^b) vs σ, the open and filled symbols correspond to forward and backward continuation of σ, unless stated otherwise, throughout the thesis.

$d\sigma$ here represents a small change in σ.

3.3 Adaptive Interlayer Coupling Triggers ES

Fig. 3.1 presents $r^a - \sigma$ profile for the multiplex network represented by Eqs. (3.1a) and (3.1b). We find that, in the absence of adaptation, the usual static λ gives rise to a continuous phase transition in layer a (Fig. 3.1(a)). However, it unfolds that the presence of adaptive interlayer coupling $\lambda r^a r^b$ strikingly leads to a discontinuous phase transition or ES (Fig. 3.1(b)). To see if there exists any hysteresis along with the discontinuity, we plot r^a values with respect to decreasing σ values. As shown by Fig. 3.1(b), the discontinuity in the phase transition is accompanied by a hysteresis. Since layers a and b are identical in topology, intralayer coupling, and natural frequency distribution, and therefore, the nature of phase transition should also remain the same in both the layers, only r^a values are plotted with respect to σ. Moreover, we do not take the average of r^a over natural frequency realizations or network topology (for random networks) because different realizations may result in different values of forward or backward critical couplings, and an average over them will make the plots continuous. We mention

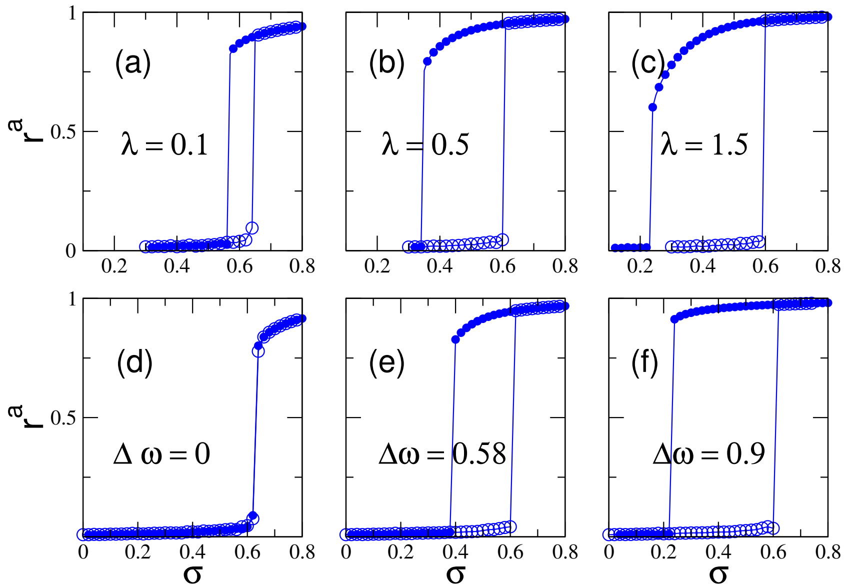

Figure 3.2: Plots in (a)-(c) present r^a vs σ for different λ values with $\Delta\omega$ fixed at 0.58. Plots in (d)-(f) present r^a vs σ for different $\Delta\omega$ values with λ fixed at 0.4. Here $N = 10000$ in all the plots.

that the phase transition, however, remains discontinuous in all the realizations.

3.3.1 Factors Determining Hysteresis Width

Fig. 3.2 further elaborates on how the interlayer coupling and natural frequency mismatch between the mirror nodes affects the transition to synchronization or to desynchronization in layer a. It turns out that an increase in λ increases the hysteresis size (Figs. 3.2(a)–3.2(c)) associated with the emergent ES. Similarly, for a given λ, an increase in natural frequency mismatch between the mirror nodes ($\Delta\omega$) also increases the hysteresis size (Figs. 3.2(d)–3.2(f)). To measure the strength of natural frequency mismatch between the mirror nodes, we consider

$$\Delta\omega = 1 - \frac{1}{2\sum_{i=1}^{N}|\omega_i^a|}\sum_{i=1}^{N}|\omega_i^a + \omega_i^b|, \tag{3.2}$$

where $0 \leq \Delta\omega \leq 1$. In the extreme cases, $\Delta\omega = 0$ if $\omega_i^a = \omega_i^b$, and $\Delta\omega = 1$ if $\omega_i^a = -\omega_i^b$. To obtain a desired value of $\Delta\omega$, starting with $\Delta\omega = 0$, two pairs of the mirror nodes are chosen randomly and the natural frequencies of the chosen nodes in layer b are swapped. After each swapping, $\Delta\omega$ is recalculated and the change is accepted if the newer value of $\Delta\omega$ is closer to the desired value; otherwise, the change is discarded. This process is repeated until we arrive at the desired value of $\Delta\omega$.

Note that the coupling value at which r^a makes the downward jump, σ_c^b, manifests a significant decrease with an increase in λ as well as $\Delta\omega$, while the changes in the forward critical coupling, σ_c^f, are negligible. Hence, appropriate choices of both λ and $\Delta\omega$ determine the threshold of the explosive transition to desynchronization.

3.4 Robustness of ES

3.4.1 Robustness Against Network Topology

The emergence of ES through interlayer adaptation largely remains robust against the changes in the network topology of the individual layers. However, an increase in the degree heterogeneity of one or both of the layers can cause suppression of ES, eventually leading to a continuous phase transition for a very high degree heterogeneity. To demonstrate the impact of network topology or degree heterogeneity, we consider regular-ring (1D) network, ER network, and SF networks with different values of degree heterogeneity (Section 1.2). An arbitrary topology for the layers is realized by considering the following set of equations (Section 1.7).

$$\dot{\theta}_i^a = \omega_i^a + \sigma \sum_{j=1}^{N} A_{ij}^a \sin(\theta_j^a - \theta_i^a) + \lambda r^a r^b \sin(\theta_i^b - \theta_i^a), \tag{3.3a}$$

$$\dot{\theta}_i^b = \omega_i^b + \sigma \sum_{j=1}^{N} A_{ij}^b \sin(\theta_j^b - \theta_i^b) + \lambda r^a r^b \sin(\theta_i^a - \theta_i^b). \tag{3.3b}$$

Figs. 3.3(a) and 3.3(b) depict that the multiplex network comprised of either ER-ER or ER-1D networks exhibits ES along with a hysteresis as depicted earlier by the multiplex network of the globally connected layers (Figs. 3.1(b) and 3.2). However, we find that the ES disappears if both the layers have heterogeneous degree distribution (Fig. 3.3 (c)). To systematically analyze the effect of degree heterogeneity on the nature of phase transition, we fix the layer a to an ER network while the degree heterogeneity of the layer b is varied. Heterogeneous networks having different values of degree heterogeneity are generated by following Section 1.2.5. Figs. 3.3(d) and 3.3(e) show that the hysteresis size decreases with decrease in the α value from 1 to 0. With a further decrease in α to -100, the hysteresis disappears (Fig. 3.3(f)). In heterogeneous networks, it happens that a partially synchronous state or a giant cluster grows in size from almost zero coupling value [12]. Perhaps, the interlayer adaptation could not suppress the formation of

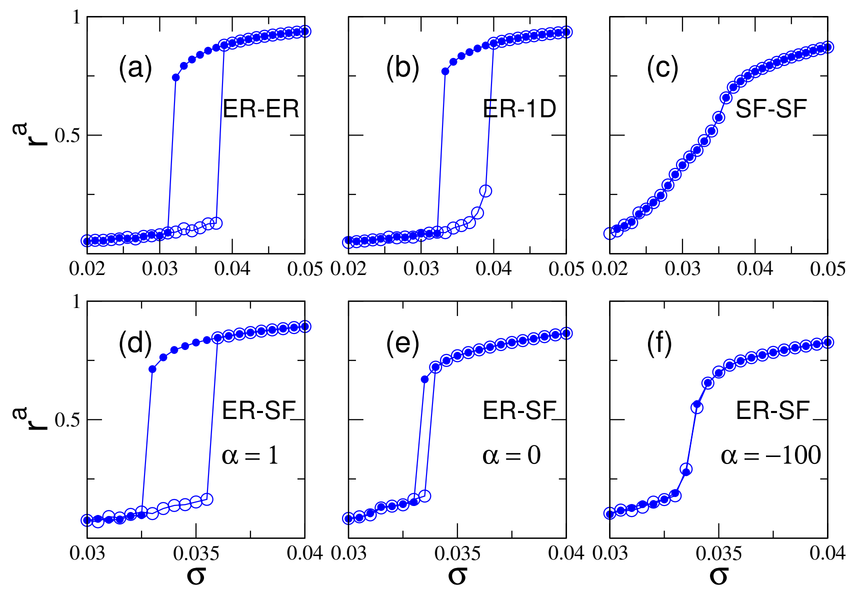

Figure 3.3: Plots of r^a vs σ show robustness of ES against changes in the network topology. Here $N = 1000$, $\lambda = 3$, and the average connectivity ($\langle k^{a(b)} \rangle$) of the two layers is $\langle k^a \rangle = \langle k^b \rangle = 16$.

the giant cluster, and therefore, it could not instigate ES in these networks.

3.4.2 Robustness Against Natural Frequency Distribution

So far, we have presented the results for a uniform distribution of the natural frequencies. Next, we check the robustness of ES against change in the natural frequency distribution. For that, we take a Gaussian natural frequency distribution for the layers; which is given by

$$g(\omega^{a(b)}) = \frac{1}{\mu\sqrt{2\pi}} e^{-\frac{\omega^{a(b)^2}}{2\mu^2}}. \tag{3.4}$$

Note that the mean value of natural frequencies in both the layers is 0, and the standard deviation μ is also same. For globally connected layers, Fig. 3.4 displays that phase transition remains discontinuous along with a hysteresis for the considered non-uniform frequency distribution. Mark that, in the forward direction, the order parameter r^a makes a jump at $\sigma_c^f \approx 0.75$, which can be predicted from Appendix B. It suggests that $\sigma_c^f = 2/(\pi g(0))$. In our case we have $g(0) = \sqrt{(}2/\pi)$, which leads to $\sigma_c^f \approx 0.798$.

3.4.3 Robustness Against the Adaptive Scheme

Finally, we demonstrate that ES exists even if we replace the interlayer multiplication factor $r^a r^b$ in Eqs. (3.1a) and (3.1b) by r^a and r^b, respectively (Fig. 3.5). In the infinite

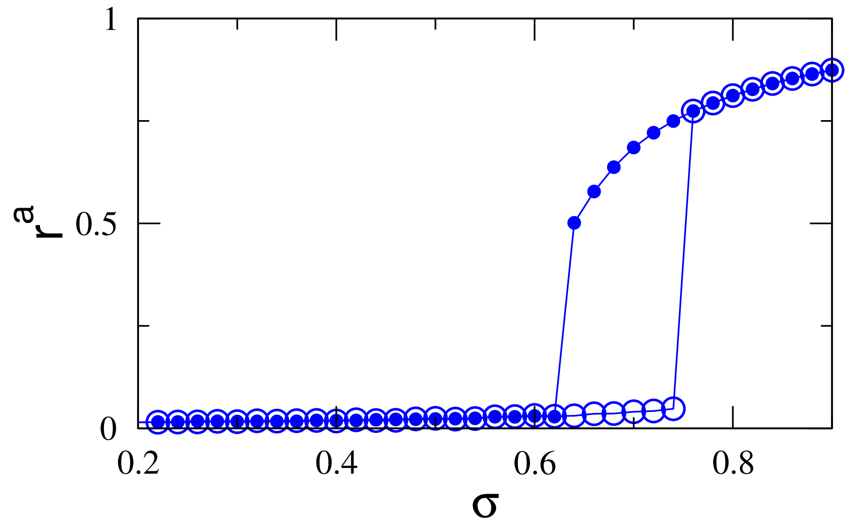

Figure 3.4: r^a vs σ for a Gaussian natural frequency distribution. The mean value of natural frequencies in both the layers is 0 and the standard deviation μ is 0.5. The natural frequencies are assigned randomly. The other parameters are $\lambda = 5$ and $N = 5000$.

size limit, the addition of coupling terms proportional to r^2 does not yield any change in the critical coupling at which the incoherent state becomes unstable. Following an analysis parallel to Ref. [73], Appendix B derives that addition of $\lambda r^a r^b \sin(\theta_i^{a(b)} - \theta_i^{b(a)})$ terms to the isolated layers do not change the critical coupling value at which the incoherent state looses its stability. Therefore, the factor $r^a r^b$ in the interlayer coupling only helps us in fixing σ_c^f at a constant value, which otherwise might be sensitive to the parameter λ or $\Delta\omega$. Mark that in the model of Zhang *et al.*, the intralayer coupling term containing r^2 was shown to be responsible for the occurrence of ES [32]; however, such a condition is not required for the case of adaptive interlayer coupling proposed in this Chapter.

3.5 Mean-field Analysis for $\Delta\omega = 1$

In the infinite network size limit, assuming that $r^{a(b)}$ and $\psi^{a(b)}$ are constant in time after a sufficient time is passed, we analytically derive $r^{a(b)}$ values using the well known mean-field approach [12]. The natural frequency of an i^{th} node in layer a is drawn from a uniform distribution, i.e., $g(\omega^a) = 1/2\gamma$, where $\gamma = 0.5$. Now we take $\Delta\omega = 1$, i.e., $\omega_i^a = -\omega_i^b$. Eqs. (3.1a) and (3.1b) can be rewritten in terms of the order parameter $r^{a(b)}$ (Eq. (1.24)) as

$$\dot{\theta}_i^a = \omega_i^a + \sigma r^a \sin(\psi^a - \theta_i^a) + \lambda A \sin(\theta_i^b - \theta_i^a), \tag{3.5a}$$

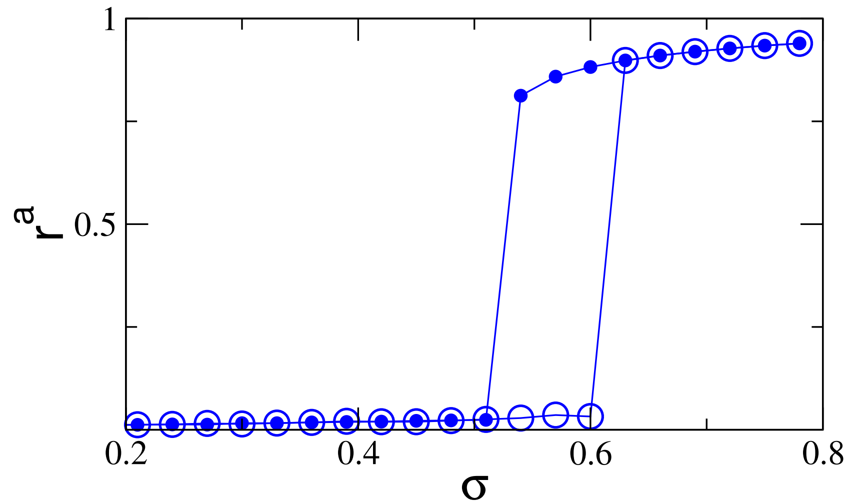

Figure 3.5: r^a vs σ when adaptive interlayer coupling $\lambda r^a r^b$ is replaced by λr^a in Eq. (3.1a) and by λr^b in Eq. (3.1b). Here $\Delta\omega = 0.33$, $\lambda = 0.2$, and $N = 10000$.

$$\dot{\theta}_i^b = -\omega_i^a + \sigma r^b \sin(\psi^b - \theta_i^b) + \lambda A \sin(\theta_i^a - \theta_i^b), \tag{3.5b}$$

where $i = 1, 2, 3, \ldots, N$ and $A = r^a r^b$. Now, due to couplings σ and λ, a fraction of the population in layer a and b synchronize and rotate with some velocity $\dot{\theta}_i^{a(b)} = \dot{\psi}^{a(b)} = \Omega$. Later in Section 3.7.1 we will justify that the statement $\dot{\theta}_i^{a(b)} = \dot{\psi}^{a(b)} = \Omega$ is valid. Note that the time independent $r^{a(b)}$ and the intralyer coupling terms in Eqs. (3.5a) and (3.5b) suggest that the mirror nodes must synchronize simultaneously. Moreover, for every synchronized oscillator of natural frequency ω if there is another synchronized oscillator of natural frequency $-\omega$, we find that $\Omega = \bar{\omega} = 0$ (Section 3.7.1), where $\bar{\omega}$ is the mean value of the natural frequencies for the locked oscillators. Therefore, the synchronous state is a fixed point state. Now, if $r^a = r^b$ and $\psi^a = -\psi^b$, Eqs. (3.5a) and (3.5b) suggest that the values of phases in the fixed point state should be such that $\theta_i^a = -\theta_i^b$. Neglecting the drifting oscillators (Appendix A) and substituting these phase values in Eq. (1.24), one gets $r^a = r^b = r$ and $\psi^a = -\psi^b$, validating the assumptions. On further assuming $\psi^a = -\psi^b = 0$ [14], Eq. (3.5a) becomes

$$\omega_i^a - \sigma r \sin(\theta_i^a) - \lambda A \sin(2\theta_i^a) = 0. \tag{3.6}$$

After substituting $\sin(2\theta_i^a) = \pm 2\sin(\theta_i^a)\sqrt{1-\sin^2(\theta_i^a)}$, Eq. (3.6) converts into a fourth order polynomial $x_i^4 + p_i x_i^3 + q_i x_i^2 + r_i' x_i + s_i = 0$, where $x_i = \sin(\theta_i^a)$, and the coefficients are given as

$$p_i = 0, \qquad q_i = \frac{\sigma^2 r^2}{4\lambda^2 A^2} - 1,$$

$$r'_i = -\frac{2\omega_i^a \sigma r}{4\lambda^2 A^2}, \quad s_i = \frac{(\omega_i^a)^2}{4\lambda^2 A^2}.$$

The roots of the polynomial are [74]

$$\begin{aligned} x_{i_{1,2}} &= \frac{R_i \pm D_i}{2}, \\ x_{i_{3,4}} &= -\frac{(R_i \pm E_i)}{2}, \end{aligned} \tag{3.8}$$

where

$$\begin{aligned} R_i &= \sqrt{z_i - q_i}, \\ D_i &= \begin{cases} \sqrt{-R_i^2 - 2q_i - 2r'_i/R_i} & \text{for } R_i \neq 0 \\ \sqrt{-2q_i + 2\sqrt{z_i^2 - 4s_i}} & \text{for } R_i = 0, \end{cases} \\ E_i &= \begin{cases} \sqrt{-R_i^2 - 2q_i + 2r'_i/R_i} & \text{for } R_i \neq 0 \\ \sqrt{-2q_i - 2\sqrt{z_i^2 - 4s_i}} & \text{for } R_i = 0. \end{cases} \end{aligned} \tag{3.9}$$

Here z_i is a real root of the polynomial $x_i^3 - q_i x_i^2 - 4s_i x_i + 4q_i s_i - r_i'^2 = 0$. Out of the four roots, a root corresponding to the physically accepted solution is selected as follows. Eq. (3.6) suggests that for any two nodes i and j, if $\omega_j^a = -\omega_i^a$, we get $\theta_j^a = -\theta_i^a$. Therefore, for the synchronous solution, we consider only that root of the polynomial which satisfies the above condition for the phases. Eq. (3.9) shows that, if $\omega_j^a = -\omega_i^a$, $R_i = R_j$, because q_i is independent of ω_i^a and the third order polynomial also does not depend on the sign of ω_i^a; therefore, z_i becomes independent of the sign of ω_i^a. Furthermore, for any nonzero value of σ, r, and ω_i^a, $R_i \neq 0$, because if $R_i = 0$ or $z_i = q_i$, the third order polynomial would imply $r'_i = 0$, which is not possible unless λ is infinite. With these facts, Eq. (3.9) returns that $D_i = E_j$; therefore, $x_{i_{1(3)}} = -x_{j_{3(1)}}$ and $x_{i_{2(4)}} = -x_{j_{4(2)}}$. Thus, a physically accepted root is either from x_{i_1} and x_{i_3}, or from x_{i_2} and x_{i_4}. We find that only the r values corresponding to x_{i_2} (for $\omega_i^a > 0$) and x_{i_4} (for $\omega_i^a < 0$) match with those of the numerical simulations (see the solid red line in Fig. 3.6); hence, the physically accepted root is $x_{i_{2(4)}}$.

The summation in the R.H.S. of Eq. (1.24) can be broken into two parts, one containing the locked oscillators and the other one containing the drifting oscillators as follows:

$$r^a e^{i\psi^a} = r_l^a e^{i\psi_l^a} + r_d^a e^{i\psi_d^a}. \tag{3.10}$$

The subscripts l and d represent the locked and the drifting oscillators, respectively. For a given σ and λ, the natural frequency of a locked oscillators must satisfy the following relation

$$|\omega_i^a| \leq max|\sigma r \sin(\theta_i^a) + \lambda A \sin(2\theta_i^a)|. \tag{3.11}$$

If $f(\theta_i^a)$ represents the R.H.S. of Eq. (3.11), it has extrema at

$$\cos(\theta_i^a)_\pm^* = \frac{-\sigma r}{8\lambda A} \pm \sqrt{\frac{\sigma^2 r^2}{64\lambda^2 A^2} + 0.5},$$

obtained from the roots of $df/d\theta_i^a = 0$. Substituting the condition for extrema in Eq. (3.11), we get

$$|\omega_i^a| \leq \left| \sin(\theta_i^a)_\pm^* \left\{ \frac{3\sigma r \pm \sqrt{\sigma^2 r^2 + 32\lambda^2 A^2}}{4} \right\} \right| \tag{3.12}$$

Since $f\{(\theta_i^a)_+^*\} > f\{(\theta_i^a)_-^*\}$, only $\cos(\theta_i^a)_+^*$ is considered to determine all the locked oscillators. Eq. (3.12) manifests that an increase in λ leads to an increase in the R.H.S., indicating that the same number of oscillators can be synchronized even at a smaller σ value, in turn causing a decrease in σ_c^b value (Figs. 3.2(a)–3.2(c)).

Neglecting the drifting oscillators in Eq. (3.10) and taking $\psi^a = 0$ and $r^a = r$, it can be rewritten as

$$r = \int_{-\gamma_c}^{\gamma_c} \sqrt{1 - \sin^2(\theta^a)} g(\omega^a) d\omega^a, \tag{3.13}$$

where $g(\omega^a) = 1$ for $|\omega^a| \leq 0.5$ and 0 for $|\omega^a| > 0.5$. After plugging the values of phases from Eq. (3.8) into Eq. (3.13), we numerically calculate the roots (r values) of Eq. (3.13). Fig. 3.6 demonstrates that the analytical prediction of r^a is in fair agreement with the corresponding numerical estimation. The solid and the dashed lines in Fig. 3.6(b) are two different solutions of Eq. (3.13) corresponding to the root $x_{i_{2(4)}}$, whereas the line with stars is a solution corresponding the root x_{i_1} (for $\omega_i^a > 0$) and x_{i_3} (for $\omega_i^a < 0$). If there exist two values of r^a for a given σ, the line with stars shows only the largest of them. It is obvious that only $x_{i_{2(4)}}$ represents the synchronous state. Fig. 3.6(a) depicts that in the absence of adaptation r^a increases gradually, yielding a partially synchronized state or a giant cluster of all nodes having $\dot{\theta}_i^a = 0$ grows in size by recruiting more and more nodes in it as σ increases. The difference between numerical

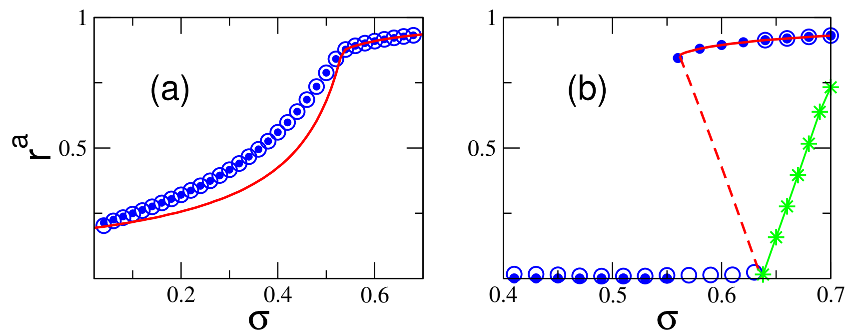

Figure 3.6: r^a vs σ, (a) without adaptive coupling and (b) with adaptive interlayer coupling. The solid line, dashed line, and solid line with stars represent analytically predicted r values from the solutions of Eq. (3.13). In the numerical simulations we take $\omega_i^a = -0.5 + (i-1)/(N-1)$ $(i = 1, \ldots, N)$, $\Delta\omega = 1$, $\lambda = 0.1$, and $N = 10000$.

and analytical predictions at $\sigma \approx 0.4$ is around 0.1, which might be arising due to the drifting oscillators in the numerical simulations. However, the difference is negligible for the smaller and the larger values of σ. In the presence of adaptation, Eq. (3.13) does not have any non-zero solution for $\sigma < \sigma_c^b$, whereas at σ_c^b one observes an abrupt transition to $r^a \approx 0.8$ (Fig. 3.6(b)). The solid line in Fig. 3.6(b) represents the stable synchronized state, and the dashed line joining the stable state to the incoherent state should then represent an unstable state [32, 43, 44, 75]. The unstable state exists due to the simultaneous presence of two stable states: the incoherent state and the coherent state. Although not shown in Fig. 3.6(b), $r^a = r = 0$ is also a solution of Eq. (3.13) for all σ values. The R.H.S. of Eq. (3.13) is zero at $r = 0$; hence, $r = 0$ is always a solution. Fig. 3.7 presents schematic diagrams showing how the stability of the fixed points $r = 0$ and $r = 1$ (which mimics the synchronized state) changes as σ increases.

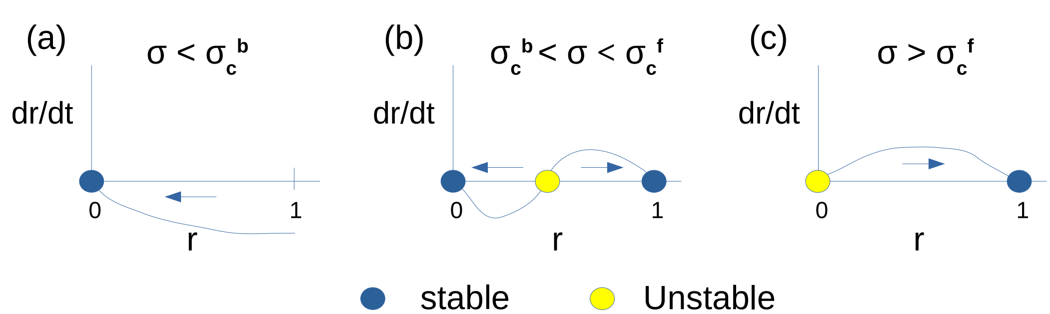

Figure 3.7: (a)-(c) present schematic diagrams showing fixed points $r = 0$ and $r = 1$ for different σ values. The arrows represent directions in which an r value will move with time.

It also displays how the unstable fixed point makes $r = 0$ and $r = 1$ locally stable.

3.5.1 Adaptive Interlayer Coupling Suppresses the Giant Cluster

The introduction of adaptation suppresses the formation of the giant cluster, which in turn leads to ES. To demonstrate this suppression, we evaluate the R.H.S. of Eq. (3.12) at $r = 0$ for two cases: $A = 1$ and $A = r^2 = 0$. Further, to simplify the calculations, we take $\sigma = \lambda$. For $A = 1$ and $A = r^2$, $\cos(\theta_i^a)_+^* \approx 0.7$ and 0, respectively, and therefore, $\sin(\theta_i^a)_+^* \approx 0.7$ and 1. Hence, for both cases, the contribution from this term remains almost same. However, the term in the large curly bracket for the two cases is $\sqrt{2}\lambda$ and 0. Therefore, the R.H.S. of Eq. (3.12) is non-zero and increases gradually for $A = 1$, while it is zero for $A = r^2$. The non-zero value of the R.H.S. in the first case also suggests that our initial statement $r = 0$ is invalid. These observations suggest that the adaptive coupling suppresses the number of oscillators in the synchronous state; in other words, the formation of the giant cluster in the forward continuation is suppressed for all $\sigma < \sigma_c^f$.

3.6 Analytical Prediction of Hysteresis Width

We use the mean-field analysis to prove that the hysteresis width increases with an increase in $\Delta\omega$. For that, first we derive the phases in the globally synchronized state. Rewriting Eqs. (3.1a) and (3.1b) in terms of the order parameter $r^{a(b)}$ leads to

$$\dot{\theta}_i^a = \omega_i^a + \sigma r^a \sin(\psi^a - \theta_i^a) + \lambda r^a r^b \sin(\theta_i^b - \theta_i^a), \tag{3.14a}$$

$$\dot{\theta}_i^b = \omega_i^b + \sigma r^b \sin(\psi^b - \theta_i^b) + \lambda r^a r^b \sin(\theta_i^a - \theta_i^b), \tag{3.14b}$$

where $i = 1, 2, 3, \ldots, N$. Since we have $\bar{\omega} = 0$, the globally synchronous state is a fixed point solution, i.e, $\dot{\theta}_i^{a(b)} = 0 \;\forall\; i$ (Section 1.7). After assuming $\psi^a \approx \psi^b = \psi$ and $r^a \approx r^b = r$, we add Eqs. (3.14a) and (3.14b), yielding

$$\sigma r \sin(\psi - \theta_i^b) = -\omega_i^a - \omega_i^b - \sigma r \sin(\psi - \theta_i^a). \tag{3.15}$$

Now, we substitute Eq. (3.15) in Eq. (3.14b) with the interlayer coupling written as $\sin(\theta_i^a - \theta_i^b) = \sin(\theta_i^a - \psi)\cos(\psi - \theta_i^b) + \cos(\theta_i^a - \psi)\sin(\psi - \theta_i^b)$, where $\cos(\psi - \theta_i^{a(b)}) \approx \pm\{1 - \sin^2(\psi - \theta_i^{a(b)})/2\}$. Note that the higher order terms in $\cos(\psi - \theta_i^{a(b)})$ can be neglected as $r^{a(b)} \approx 1$ in the synchronous state implies that $\theta_i^{a(b)} \approx \psi$ (Eq. (1.24)). It also indicates that only the positive value of $\cos(\psi - \theta_i^{a(b)})$ must be considered. After some mathematical simplifications, Eq. (3.14b) converts into a third order polynomial $x_i^3 + p_i x_i^2 + q_i x_i + r_i' = 0$, where $x_i = \sin(\psi - \theta_i^a)$. The coefficients of the polynomial are

$$\begin{aligned} p_i =& \frac{(\omega_i^a + \omega_i^b)(3\lambda r)}{2\sigma r^2 \lambda}, \\ q_i =& \frac{1}{\lambda r^2}\Big\{ -\sigma r - 2\lambda r^2 + \frac{(\omega_i^a + \omega_i^b)^2 \lambda}{(2\sigma^2)} \Big\}, \\ r_i' =& -\frac{1}{\lambda r^2}\Big\{ \omega_i^a + \frac{(\omega_i^a + \omega_i^b)\lambda r}{\sigma} \Big\}. \end{aligned} \tag{3.16}$$

And the roots of the polynomial are given by [74]

$$x_{i_1} = U_i + V_i - \frac{p_i}{3}, \tag{3.17}$$

$$x_{i_2} = -\frac{(U_i + V_i)}{2} + i\frac{\sqrt{3}}{2}\frac{(U_i - V_i)}{2} - \frac{p_i}{3}, \tag{3.18}$$

$$x_{i_3} = -\frac{(U_i + V_i)}{2} - i\frac{\sqrt{3}}{2}\frac{(U_i - V_i)}{2} - \frac{p_i}{3}, \tag{3.19}$$

where

$$\begin{aligned} U_i &= \Big\{ \frac{-b_i}{2} + \sqrt{\frac{b_i^2}{4} + \frac{a_i^3}{27}} \Big\}^{1/3}, \\ V_i &= \Big\{ \frac{-b_i}{2} - \sqrt{\frac{b_i^2}{4} + \frac{a_i^3}{27}} \Big\}^{1/3}, \end{aligned} \tag{3.20}$$

with $a_i = (3q_i - p_i^2)/3$ and $b_i = (2p_i^3 - 9p_i q_i + 27r_i')/27$. A physically acceptable root should be such that as $\sigma \to \infty$, we have $x_i \to 0$. Moreover, as $\sigma \to \infty$, we get $p_i \to 0$, $q_i \to -\infty$, and $r_i' \to -\omega_i^a/(\lambda r^2)$. Therefore, $a_i \to -\infty$ and $b_i \to (\omega_i^b - \omega_i^a)/2\lambda r^2$; in turn, $\frac{b_i^2}{4} + \frac{a_i^3}{27} \to -\infty$. A negative value of $\frac{b_i^2}{4} + \frac{a_i^3}{27}$ implies that U_i and V_i are complex numbers [74]. Writing the roots in another form leads to

$$x_{i_k} = 2\sqrt{\frac{-a_i}{3}}\cos\Big(\frac{\phi_i}{3} + \frac{2(k-1)\pi}{3}\Big) - \frac{p_i}{3}, \tag{3.21}$$

where $k = 1,2,3$ and $\phi_i = \cos^{-1}\Big(\pm\sqrt{\frac{b_i^2/4}{-a_i^3/27}}\Big)$ for $b_i \lesseqgtr 0$. As $\sigma \to \infty$, $\phi_i \to \pi/2$, and therefore, at infinite coupling we get $x_{i_1} = 2\sqrt{\frac{-a_i}{3}}\cos(\frac{\pi}{6})$, $x_{i_2} = 2\sqrt{\frac{-a_i}{3}}\cos(\frac{5\pi}{6})$, and $x_{i_3} = 2\sqrt{\frac{-a_i}{3}}\cos(\frac{3\pi}{2})$. x_{i_1} and x_{i_2} diverge, while $x_{i_3} \to 0$. Note that, in x_{i_3}, $\sqrt{\frac{-a_i}{3}}$ increases while $\cos(\frac{\phi_i}{3} + \frac{4\pi}{3})$ decreases. Since the decrement is faster (as $\cos(\phi_i)$ is proportional to $a_i^{-3/2}$) than the increment, the overall product experiences a decrement as well. Hence, the physically accepted root is x_{i_3}. In summary, using three assumptions $r^a = r^b = r$, $\psi^a = \psi^b = \psi$, and $\cos(\psi - \theta_i^{a(b)}) = \{1 - \sin^2(\psi - \theta_i^{a(b)})/2\}$, the phases in the globally synchronous state can be written in the form of Eq. (3.19).

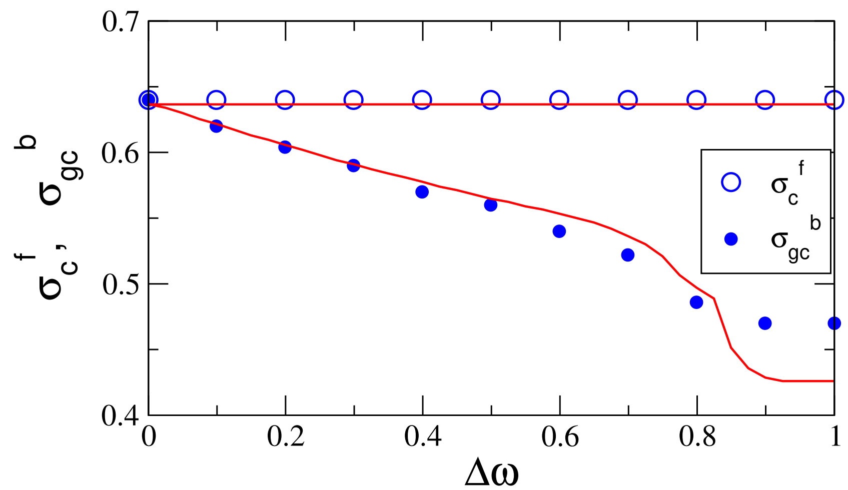

Figure 3.8: σ_c^f and σ_{gc}^b as a function of $\Delta\omega$. Here $\omega_i^a = -0.5+(i-1)/(N-1)$ ($i = 1,2,\ldots,N$), $\lambda = 0.2$, and $N = 10000$. The upper red line represents the value $4\gamma/\pi$, where $\gamma = 0.5$; the lower red line represents σ_{gc}^b values from the analytical calculations.

Next, we proceed to calculate σ_{gc}^b, the minimum σ value below which a globally synchronous state can not exist. Note that in general $\sigma_{gc}^b \geq \sigma_c^b$, but the transition to desynchronization from a high $r^{a(b)}$ value, unless λ is high (Fig. 3.2), implies that $\sigma_{gc}^b \approx \sigma_c^b$. To find σ_{gc}^b, Eq. (1.24) is solved numerically after substituting $\sin(\psi - \theta_i^a)$ values from Eq. (3.19). Fig. 3.8 corroborates that an increase in $\Delta\omega$ increases the hysteresis width ($\sigma_c^f - \sigma_{gc}^b$). Notice that σ_c^f remains independent of $\Delta\omega$. Appendix B predicts that $\sigma_c^f = 4\gamma/\pi \approx 0.636$, matching excellently with the numerical simulations.

Fig. 3.8 reveals that the difference between numerically and analytically found values of σ_{gc}^b decreases as $\Delta\omega \to 0$. We justify this as follows: For $\Delta\omega = 0$, the phases given by Eq. (3.19) are exact (Section 3.7.1), and therefore, the error due to the approximations is zero. For $\Delta\omega = 1$, the difference between the numerically and analytically obtained σ_{gc}^b values is around 0.05. As $\Delta\omega \to 1$, Figs. 3.10(d)–3.10(g) in Section 3.7.2 convey that the analytically calculated r^a values are slightly higher than the numerical ones. Moreover, Eq. (3.22) of Section 3.7.1 reveals that the natural frequencies of the locked oscillators must satisfy the relation

$$(\omega_i^{a(b)})^2 > \frac{4(\sigma r^{1/3} + 2\lambda r^{4/3})^3}{27\lambda}.$$

The relation above suggests that σ_{gc}^b should be smaller if r is higher, and therefore, the observation in Fig. 3.8 is justified.

3.7 Validity of Assumptions

In this section we justify all those assumptions that have been used throughout this Chapter.

3.7.1 Validity of the Assumptions at $\Delta\omega = 0, 1$

Firstly, we prove that the assumptions (a) $r^a = r^b = r$ and (b) $\psi^a = \psi^b = \psi$ in Section 3.6 are valid. At $\Delta\omega = 0$, i.e., for $\omega_i^a = \omega_i^b = \omega_i$, we get $a_i < 0$ and $b_i = 0$. Therefore, $b_i^2/4 + a_i^3/27$ is negative and the roots can be represented in the form given by Eq. (3.21). The first term in Eq. (3.21) is zero because $\phi_i = \pi/2$, and therefore, $\sin(\psi - \theta_i^a) = -p_i/3 = -\omega_i/\sigma r$. Putting this in Eq. (3.15), we get $\sin(\psi - \theta_i^b) = -\omega_i/\sigma r$. Therefore, we have $\theta_i^a = \theta_i^b$. For an identical distribution of phases, Eq. (1.24) returns $r^a = r^b = r$ and $\psi^a = \psi^b = \psi$. The interlayer coupling terms in Eqs. (3.14a) and (3.14b) get cancelled due to $\theta_i^a = \theta_i^b$, and thus, the phase values in this case are exact. Mark that the synchronized state for the multiplex network and for the isolated layers are same [35].

To prove that assumptions (a) and (b) are valid for $\Delta\omega = 1$, we proceed as follows: The quantity $\frac{b_i^2}{4} + \frac{a_i^3}{27}$ can not be positive because it would imply that

$$(\omega_i^{a(b)})^2 > \frac{4(\sigma r^{1/3} + 2\lambda r^{4/3})^3}{27\lambda}. \tag{3.22}$$

The relation above shows that oscillators with natural frequencies farther from $\bar{\omega} = 0$ are locked, while the oscillators closer to $\bar{\omega} = 0$ are not, which is contrary to Eq. (3.12). Therefore, $\frac{b^2}{4} + \frac{a^3}{27} \leq 0$, and the phases can be written in the from of Eq. (3.21). For the considered natural frequency distribution in Fig. 3.8, we have $\omega_i^a = -\omega_{N-i+1}^a$, where $i = 1, 2, \ldots, N/2$. From Eq. (3.21) it can be checked that $\sin(\psi - \theta_i^a) = -\sin(\psi - \theta_{N-i+1}^a)$. Eq. (3.15) now returns $\sin(\psi - \theta_i^a) = -\sin(\psi - \theta_i^b)$, and therefore, $\theta_i^b = \theta_{N-i+1}^a$. Similarly, it can be checked that $\theta_{N-i+1}^b = \theta_i^a$. The distribution of phases is identical in the layers; hence, Eq. (1.24) returns $r^a = r^b = r$ and $\psi^a = \psi^b = \psi$.

Secondly, we prove that, at $\Delta\omega = 1$, the velocity of $\psi^{a(b)}$ and the synchronized oscillators are same, i.e., $\dot{\theta}_i^{a(b)} = \dot{\psi}^{a(b)} = \Omega$. After this we will show that $\Omega = 0$. We know from Eq. (1.24) that

$$\tan\psi^{a(b)} = \frac{\sum\limits_{locked} \sin(\theta_j^{a(b)})}{\sum\limits_{locked} \cos(\theta_j^{a(b)})}. \tag{3.23}$$

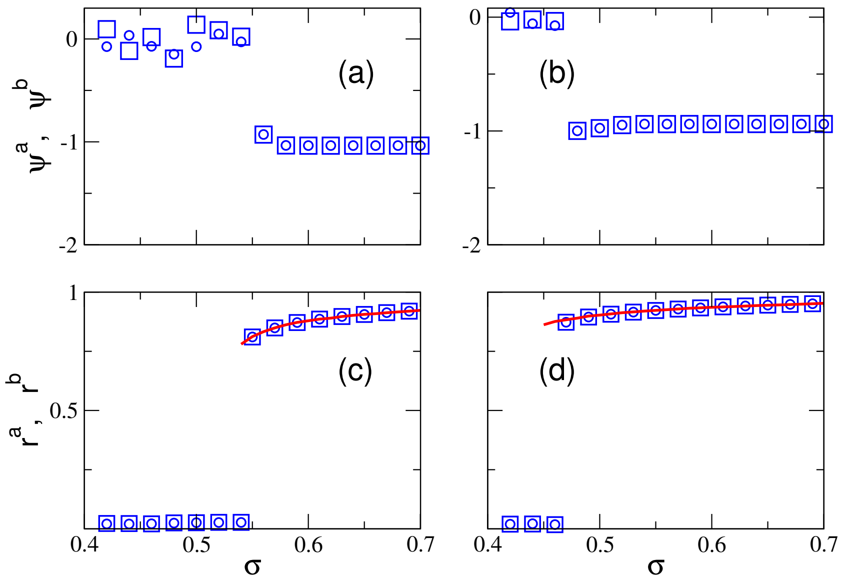

Figure 3.9: (a) and (b) show time averaged ψ^a (the circles) and ψ^b (the squares) in the backward continuation of σ; (c) and (d) show r^a (the circles) and r^b (the squares) in the same direction. Here $\Delta\omega = 0.381$ in (a) and (c), while it is 0.781 in (b) and (d). All plots have $\lambda = 0.2$ and $N = 10000$. The continuous red lines in (c) and (d) represent analytically predicted r^a values.

If a group of oscillators rotates with a velocity $\dot{\theta}_i^{a(b)} = \Omega$, differentiating Eq. (3.23) will leads to

$$\dot{\psi}^{a(b)} = \frac{\Omega}{\sec^2(\psi^{a(b)})}\left\{1 + \left(\frac{\sum_{locked} \sin(\theta_j^{a(b)})}{\sum_{locked} \cos(\theta_j^{a(b)})}\right)^2\right\}. \tag{3.24}$$

The term in the curly bracket is nothing but $\sec^2(\psi^{a(b)})$. Therefore, the relation $\dot{\theta}_i^{a(b)} = \dot{\psi}^{a(b)} = \Omega$ holds. Now, we show that the synchronized oscillators agree with the assumption $\Omega = 0$. Comparing the imaginary terms of Eq. (1.24) leads to

$$\sum_{locked} \sin(\theta_i^a - \psi^a) = 0. \tag{3.25}$$

Taking $\dot{\theta}_i^{a(b)} = \Omega$ and along with Eq. (3.5a), Eq. (3.25) can be rewritten as

$$\Omega = \frac{1}{N_l}\sum_{locked} \omega_i^a + \frac{\lambda A}{N_l}\sum_{locked} \sin(\theta_i^b - \theta_i^a), \tag{3.26}$$

where N_l represents the total number of locked oscillators. As suggested by Eq. (3.12), the natural frequencies of the synchronized oscillators are symmetric around 0; therefore, the first term in the R.H.S. of Eq. (3.26) is zero. Now, as discussed in Section 3.5, we have $\theta_i^b = -\theta_i^a$. And for every synchronized ω_i^a with phase θ_i^a there is a synchro-

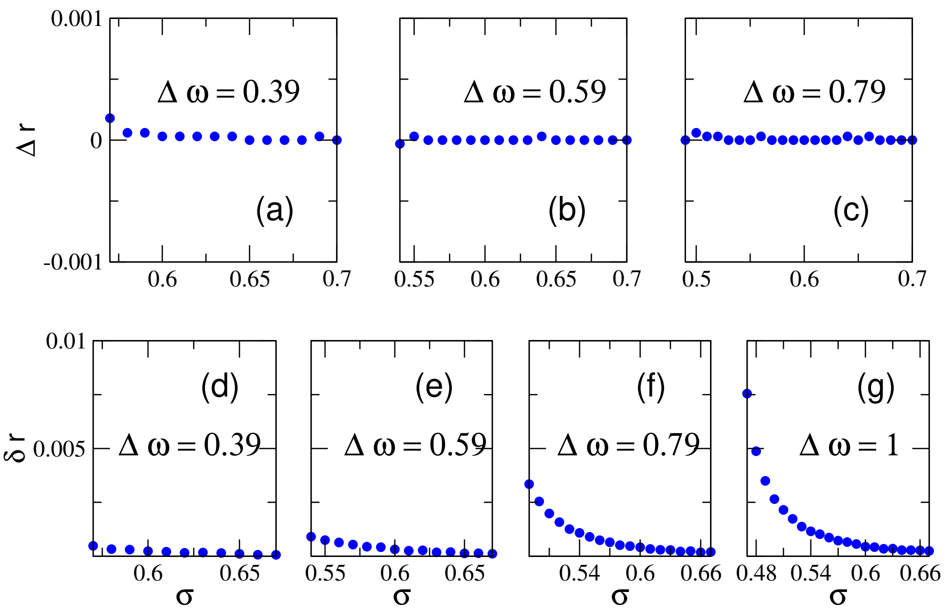

Figure 3.10: (a)-(c) show Δr vs σ, while (d)-(g) show δr vs σ. Δr represents the difference between analytically calculated r values for layer a and layer b; δr represents the difference between analytically and numerically calculated r values for layer a. The network parameters are the same as in Fig. 3.8.

nized $-\omega_i^a$ with phase $-\theta_i^a$. So the second term in the R.H.S. also gets canceled, and we get $\Omega = 0$.

3.7.2 Validity of the Assumptions for $0 < \Delta\omega < 1$

For intermediate $\Delta\omega$ values, numerically or analytically we prove that the assumptions (a) $r^a = r^b = r$, (b) $\psi^a = \psi^b = \psi$, and (c) $\cos(\psi - \theta_i^{a(b)}) = \{1 - \sin^2(\psi - \theta_i^{a(b)})/2\}$ are valid. Fig. 3.9 reveals that numerical calculations agree with assumptions (a) and (b). Moreover, analytically and numerically calculated r^a values are also in fair agreement (Figs. 3.9(c) and 3.9(d)). Analytical evaluation of r^a and r^b further elaborates on the validity of assumption (a) (Figs. 3.10(a)–3.10(c)). Finally, we prove the validity of assumption (c). Note that $\cos(\psi - \theta_i^{a(b)}) \leq 1 - \sin^2(\psi - \theta_i^{a(b)})/2$; here equality holds only for $\theta_i^{a(b)} = \psi$. Therefore, assumption (c) shifts the phases closer to ψ, and hence, we should get a higher r^a value from the analytical calculations. Figs. 3.10(d)–3.10(g) reveal that the difference between analytically and numerically found r^a values, δr, is marginally positive. δr grows as $\Delta\omega \to 1$, and at $\Delta\omega = 1$, we get maximum $\delta r \approx 0.01$. An increment in the σ value leads to a decrement in δr value. As expected, this is due to the fact that $\theta_i^{a(b)} \to \psi$ as $\sigma \to \infty$.

3.8 Conclusion

In a system of networked oscillators, any microscopic strategy that can suppress the formation of the giant cluster will eventually lead to ES. It was earlier reported that intralayer adaptive coupling through local order parameters triggers ES in a multilayer network of virtual interlayer links [32]. The present work showed that an adaptive interlinked setup between the mirror nodes by means of the global order parameters can also trigger ES in the layers.

Since ES here arises due to interlayer links, its properties are also different than intralayer adaptation-induced ES. Firstly, shuffling of natural frequencies or correlations among natural frequencies of mirror nodes affect the phase transition. The mean-field analysis indicates that, if $\Delta\omega = 0$, one would not observe ES for non-uniform natural frequency distributions, i.e., Gaussian, Lorentzian, etc. Secondly, nonlinearity in the power of order parameter is not required, i.e., simple $\lambda r^{a(b)}$ is also sufficient to incite ES. Thirdly, we have an additional control parameter λ to shape the hysteresis size. The independence of the forward critical coupling from the network parameters is also possible due to the factor $r^a r^b$.

The occurrence of ES through interlayer adaptation largely remains robust against changes in the topology of the layers, except for a very high degree heterogeneity of either of the layers. A mean-field analytical treatment has been provided to ground the perceived outcomes, and the analytical predictions are in fair agreement with the numerical estimations. Our model may be relevant to real-world systems having a multilayer underlying network structure. For example, large-scale multilayer brain networks can be defined based on the functional interdependence of the brain regions [29].

Chapter 4

Explosive Synchronization in Interlayer Phase-shifted Multiplex Networks

4.1 Introduction

A phase-shift in the coupling terms of the Kuramoto model (Eq. (1.10)) was introduced by Sakaguchi and Kuramoto a long time back [15]. For single networks, it has been witnessed that a simple setup of uniformly phase-shifted oscillators does not exhibit any ES. The same can also be verified from Eq. (1.17a) that gives $r = \sqrt{1 - \frac{2\gamma}{\sigma \cos(\alpha)}}$. The relation reveals that an increase in σ causes a continuous increase in the order parameter r. For specific natural frequency distributions, Omelchenko and Wolfrum [76] have shown some strange synchronization transitions where bi-stability (which suggest that ES may exist as well) exists in the phase-shifted Kuramoto oscillators; however, they also observed that the phase transition remains continuous for a simple symmetric natural frequency distribution. Similarly, to the best of our knowledge, we do not find any study showing the emergence of ES due to distributed phase shifts [20].

Due to its similarity with the multilayer networks, it is worthy to mention here the model of multiple populations of phase oscillators. The model has shown different kinds of phenomena like chimera, chaos due to a phase shift in the intra or interlayer couplings [77–82]. However, ES has not been mentioned in the populations due to phase-shifted couplings. Notably, a few works have taken the same model as ours but with identical oscillators; they have found the presence of chimera states due to a phase shift in the intra or interlayer couplings [83, 84].

The phase-shifted Kuramoto oscillators on single networks have attracted significant attention in the past (Section 1.4.3), and therefore, it is worthy to investigate if a phase-shift in the coupling terms can instigate ES in these oscillators. Although different methods have been proposed in past years to incite ES in first-order Kuramoto oscillators on single and multilayer networks, none of them have shown a phase-shift to be a parameter responsible for ES (Section 1.8). In Section 1.4.1, we saw that a uniform phase-shift suppresses the onset of the synchronized state. It gives us a hint that if both kinds of couplings, with and without phase-shift, are present in a network, we may get ES. In this Chapter we show that, indeed, a phase shift in the interlayer coupling terms of a multiplex network of Kuramoto oscillators triggers ES in the layers. As $\alpha \to \pi/2$, the ES emerges along with a hysteresis. Finally, for a particular arrangement of phase-shifted couplings, we extend our results to single networks, showing that our results are framework-independent.

4.2 Model

We take a multiplex network of two globally connected layers where each node in a layer is represented by a Kuramoto oscillator. An i^{th} node in layer $a(b)$ is connected with its mirror node in layer $b(a)$ through an interlayer coupling having a phase shift α, i.e., the angular velocity of an i^{th} oscillator in layer $a(b)$ is given by

$$\dot{\theta}_i^a = \omega_i^a + \frac{\sigma}{N}\sum_{j=1}^{N}\sin(\theta_j^a - \theta_i^a) + \lambda\sin(\theta_i^b - \theta_i^a + \alpha), \tag{4.1a}$$

$$\dot{\theta}_i^b = \omega_i^b + \frac{\sigma}{N}\sum_{j=1}^{N}\sin(\theta_j^b - \theta_i^b) + \lambda\sin(\theta_i^a - \theta_i^b + \alpha), \tag{4.1b}$$

where $i = 1, 2, 3, \ldots, N$. Initial phases of the oscillators are drawn from a uniform random distributions in the range $-\pi \leq \theta_i^{a(b)} \leq \pi$. To keep the natural frequency distribution identical for the layers, $\omega_i^{a(b)}$ are taken from the relation $\omega_i^{a(b)} = -0.5 + (i-1)/(N-1)$, where $i = 1, 2, 3, \ldots, N$. However, the mirror nodes have different natural frequencies in general, i.e., $\omega_i^a \neq \omega_i^b$. σ denotes the intralayer coupling strength among the oscillators in layer $a(b)$, while λ represents the interlayer coupling strength. Except Figs. 4.2(a)–4.2(c), the ES is induced by varying the phase shift α from 0 to $\pi/2$.

Eqs. (4.1a) and (4.1b) are solved numerically using the Runge-Kutta 4^{th} order method with adaptive step size. Specifically, we use ode45 solver in MATLAB. Although the relative and absolute error tolerances vary in different numerical simulations, their maximum values are 10^{-7} and 10^{-6}, respectively. The nature of the phase transition is identified by plotting the time-averaged order parameter r^a as a function of σ. The time average is performed over 1000 time interval after neglecting the initial 1000 time interval. We find that the introduction of a phase shift α in interlayer coupling terms of a multiplex network instigates ES in the layers.

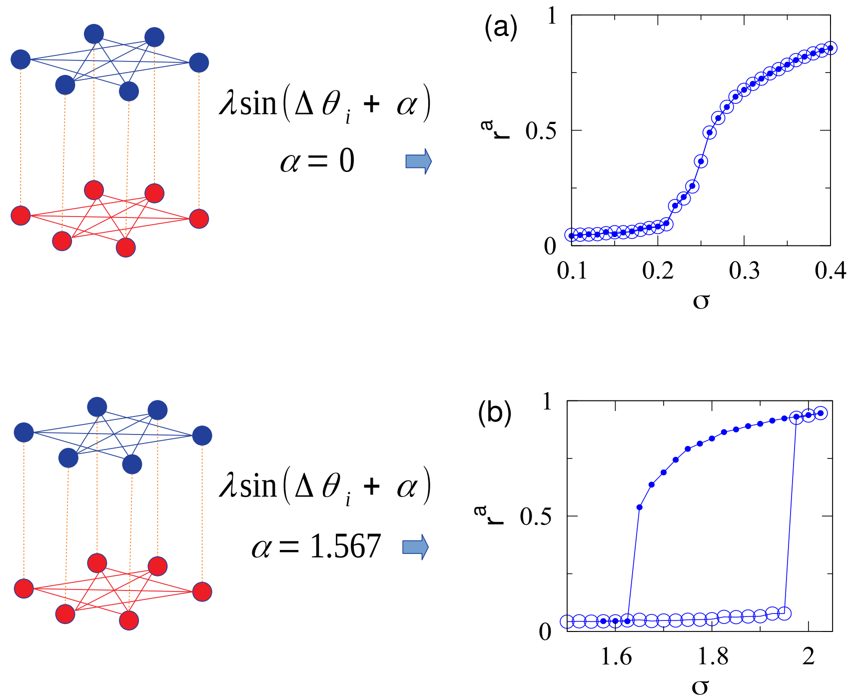

Figure 4.1: (a) and (b) present r^a with respect to σ, showing that an increase in α turns a continuous phase transition into a discontinuous one. The schematic diagrams of the multiplex networks on the L.H.S. are shown only for presentation. The layers are globally connected networks. Here $N = 1000$, $\lambda = 10$, and $\Delta\omega \approx 0.8$.

4.3 Interlayer Phase Shift Gives Rise to ES

Fig. 4.1(a) shows that, at $\alpha = 0$, r^a increases continuously with increase in σ, while an increase in α to 1.567 turns the phase transition into a discontinuous one (Fig. 4.1(b)). Similar to the previous Chapter, the discontinuity in the phase transition is accompanied by a hysteresis. As explained later, the term $\lambda \sin(\alpha) \cos(\theta_i^{a(b)} - \theta_i^{b(a)})$ accounts for the occurrence of ES. Since the layers are identical in all network parameters, i.e., topology, natural frequency distribution, and intralayer couplings are the same, the nature of the phase transition should also remain the same in both the layers; therefore, only r^a values are plotted with respect to σ.

4.3.1 Factors Determining the Hysteresis Width

Along with α values, we find that the hysteresis width ($\Delta\sigma$) depends on the interlayer coupling strength (λ) and a parameter $\Delta\omega$ governing the natural frequency mismatch between the mirror nodes. It is defined as

$$\Delta\omega = \frac{1}{2\sum_{i=1}^{N}|\omega_i^a|}\sum_{i=1}^{N}|\omega_i^a - \omega_i^b|, \tag{4.2}$$

where $0 \leq \Delta\omega \leq 1$. It is a measure of the total distance between the natural frequencies of the mirror nodes. The minimum value 0 corresponds to $\omega_i^a = \omega_i^b$ (the same natural frequencies for the mirror nodes), while the maximum value 1 corresponds to $\omega_i^a = -\omega_i^b$. We mention that other random configurations of natural frequencies may also satisfy the relation $\Delta\omega = 1$, but we only take $\omega_i^a = -\omega_i^b$. Remember that a different natural frequency mismatch parameter was defined earlier in Chapter 3 (Eq. (3.2)). For both parameters it can be checked that, as $\Delta\omega \to 1$, $\omega_i^a \to -\omega_i^b$. The difference between the two parameters is as follows: Eq. (3.2) shows that $\omega_i^a = -\omega_i^b$ is the only configuration that can satisfy $\Delta\omega = 1$, while in case of Eq. (4.2) other configurations may also exist. Similarly, for $\Delta\omega = 0$, Eq. (4.2) returns only one configuration, $\omega_i^a = \omega_i^b$, while Eq. (3.2) may return other configurations as well. In this Chapter, we realized that Eq. (4.2) is a much-simple representation of natural frequency mismatch between the mirror nodes, so we switched to this. Starting with $\Delta\omega = 0$, a desired $\Delta\omega$ value is achieved by following the same procedure as we discussed in Section 3.3.1.

Figs. 4.2(a)–4.2(c) exhibit that, at $\Delta\omega = 1$, an increase in λ results in a larger hysteresis width. This observation is expected because if $\lambda\sin(\alpha)\cos(\theta_i^{a(b)} - \theta_i^{b(a)})$ is responsible for ES, an increase in its magnitude should have a favorable impact on ES. Interestingly, the hysteresis width does not increase monotonically as we approach $\alpha = \pi/2$. For small λ values, the hysteresis width is maximum if $0 < \alpha < \pi/2$ or $\pi/2 < \alpha < \pi$ (Fig. 4.2(a)), while for large λ values it is maximum at $\alpha = \pi/2$ (Fig. 4.2(c)). Since $\Delta\sigma$ values are symmetric around $\alpha = \pi/2$, and hence, for a better view of the plots here we present the results for $0 < \alpha < \pi$. The rest of the Chapter presents results for

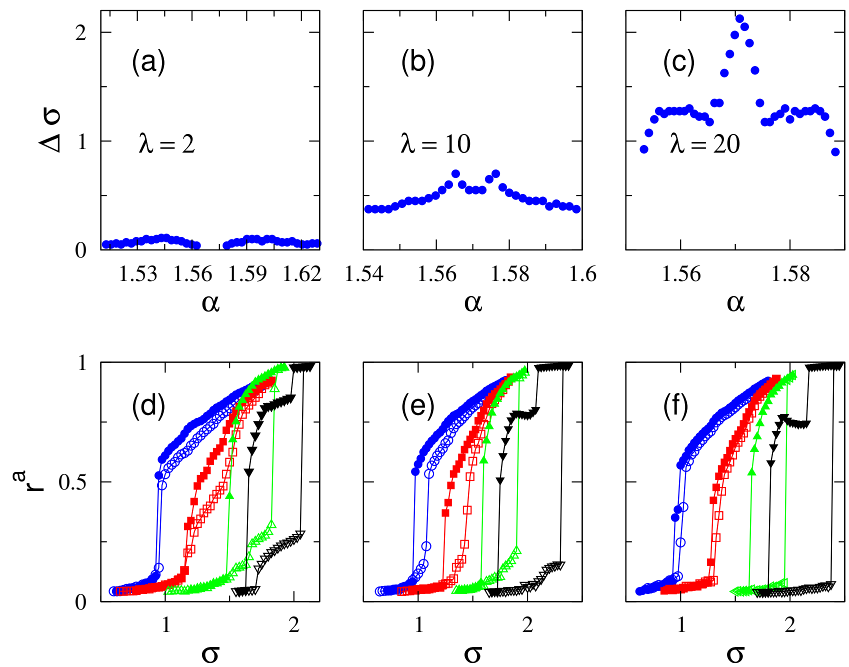

Figure 4.2: (a)-(c) $\Delta\sigma$ versus α displays a favourable impact of λ on the hysteresis width. Here $\Delta\omega$ is fixed at 1. (d)-(f) r^a vs σ shows the dependence of ES or the hysteresis width on $\Delta\omega$. Here (d)-(f) represent the plots for $\alpha \approx 1.5561$, 1.5634, 1.5671, respectively; in each figure, the lines with circles, squares, upper-triangles, and lower-triangles correspond to $\Delta\omega \approx 0.4$, 0.6, 0.8, 1, respectively. In all these figures, the layers are globally connected with $N = 1000$.

$0 \leq \alpha \leq \pi/2$ only. Another parameter which affects the ES or hysteresis width is $\Delta\omega$. Figs. 4.2(d)–4.2(f) reveal that for a given λ and α values, an increase in $\Delta\omega$ changes a continuous or almost continuous phase transition into a discontinuous one. Using a mean-field analysis, Section 4.5 will justify the impact of $\Delta\omega$ on ES.

We find that jump size in the backward continuation of σ is not significant in some numerical simulations; therefore, there is no critical coupling at which a discontinuity in the backward transition occurs. To follow a consistent approach to measure the hysteresis width, $\Delta\sigma$ in Figs. 4.2(a)–4.2(c) represents difference between couplings corresponding to the meeting points of r values in the forward and backward directions. Furthermore, only $\Delta\sigma$ values close to $\alpha = \pi/2$ are plotted in Figs. 4.2(a)–4.2(c) because we do not find ES for other α values in the range 0 to π. As shown later in Fig. 4.5(c), although for some α values there can exist a bistable regime without any jump. Since such a hysteresis is not associated with ES, it has been neglected in Figs. 4.2(a)–4.2(c). Similarly, it is also possible that along with a hysteresis consisting of a significant jump,

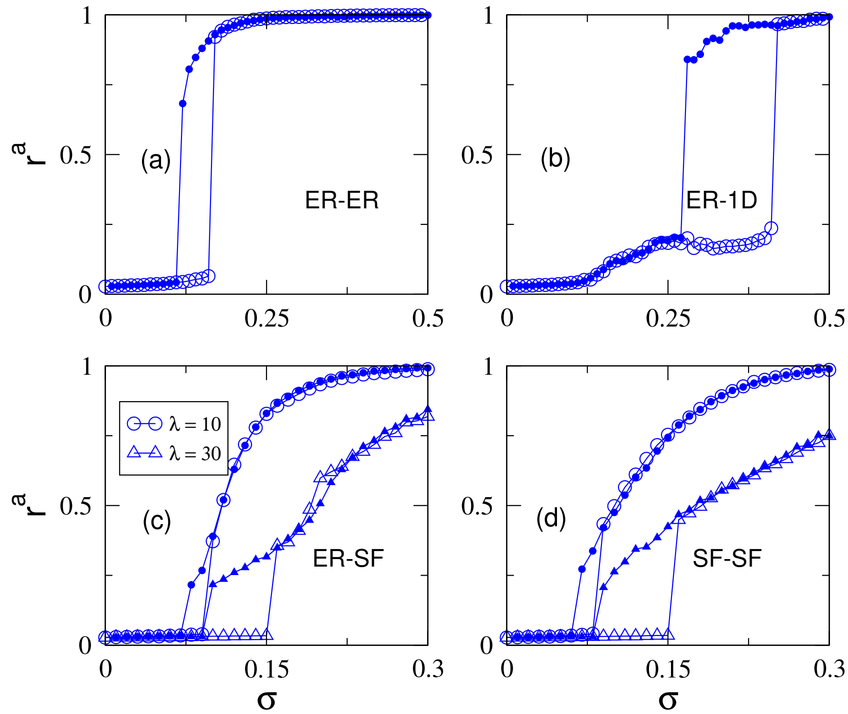

Figure 4.3: (a)-(d) r^a versus σ displays the effect of change in network topology on ES. The network parameters are $N = 1000$ and $\lambda = 10$. The natural frequencies are assigned randomly, which leads to $\Delta\omega \approx 0.67$. The average connectivity ($< k^{a(b)} >$) of both the layers is $< k^a >=< k^b >= 16$. To reduce the time taken by the numerical simulations, here we have used Runga-Kutta fourth order method with a fixed step size of 0.01.

another hysteresis without a sizable jump can also exist (Fig. 4.5(d)), which is also neglected in Figs. 4.2(a)–4.2(c).

4.4 ES for Complex Networks and Non-uniform Frequency Distributions

Besides the globally connected networks, the phase-shifted coupling can induce ES in complex networks having a homogeneous degree distribution. However, we find that if the degree distribution is heterogeneous, the jump size is reduced significantly. To show this, we consider ER network, regular-ring (1D) network, and Bárabasi and Albert's SF network for the multiplexed layers. As adopted earlier in Chapter 3, the intralayer coupling $\frac{\sigma}{N}\sum_{j=1}^{N}\sin(\theta_j^{a(b)} - \theta_i^{a(b)})$ in Eqs. (4.1a) and (4.1b) is replaced by $\sigma\sum_{j=1}^{N}A_{ij}^{a(b)}\sin(\theta_j^{a(b)} - \theta_i^{a(b)})$. Figs. 4.3(a) and 4.3(b) depict that, similar to the globally connected layers, a multiplex network consisting of ER-ER and ER-1D networks exhibits ES along with a hysteresis. Although the position of hysteresis and its width

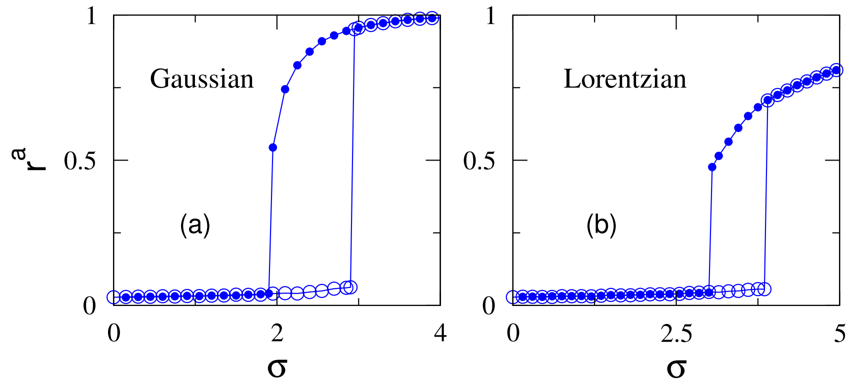

Figure 4.4: (a) and (b) present r^a vs σ, showing that ES exists for the non-uniform frequency distributions. The mean value of natural frequencies is 0 in both the distributions; the standard deviation for Gaussian distribution and the half-width at half maxima for Lorentzian distribution are both 0.5. The layers are globally connected with $N = 1000$ (for Gaussian), $N = 998$ (for Lorentzian), $\lambda = 10$, and $\alpha = \pi/2$. The natural frequencies to the oscillators are assigned randomly.

may change with a change in topology. Keeping all the network parameters same, next we multiplex a homogeneous network (ER network) with a heterogeneous network (SF network), or take both layers as SF networks. Although a hysteresis exists for these topologies, the jump size is decreased significantly (Figs. 4.3(c) and 4.3(d)). Since an increase in λ has a favorable impact on ES, we increase the λ value from 10 to 30 to see if an explosive transition can be generated. As shown by Figs. 4.3(c) and 4.3(d) the jump size remains almost the same. Therefore, we conclude that heterogeneous networks have an adverse impact on ES. We encountered the same in Chapter 3 as well, SF networks favor the onset of a partially synchronized state from almost zero coupling value. Therefore, here also, the phase-shifted model could not suppress the gradual rise in synchronization, and consequently, it failed to generate a significant jump in ES.

So far we have shown ES for a uniform natural frequency distribution. Now, we explore the effect of change in the natural frequency distribution on ES. Keeping the layers globally connected and the natural frequency distribution for the layers identical, we consider two important but symmetric natural frequency distributions: Gaussian and Lorentzian. Figs. 4.4(a) and 4.4(b) present that the phase transition remains discontinuous along with a hysteresis. Therefore, the interlayer phase shift is capable of inducing ES for uniform as well as non-uniform natural frequency distributions. We mention that the Lorentzian frequencies are generated using inverse transform sampling, i.e., using the formula $(1/2)\tan(\pi(w-0.5))$. Here w is a vector containing uniformly distributed numbers $w_i = (i-1)/(N-1)$, with $i = 2,3...N-1$. The numerical simulations for the Lorentzian distribution take an unusually long time due to two natural frequencies of the order of 10^{15}; therefore, these natural frequencies are deleted from the distribution.

4.5 Mean Field Analysis

Assuming that $r^{a(b)}$ and $\dot{\psi}^{a(b)}$ are constant in time after a steady state is reached, we derive $r^{a(b)}$ values using the mean-field approach. In terms of $r^{a(b)}$ and $\psi^{a(b)}$, Eqs. (4.1a) and (4.1b) can be rewritten as

$$\dot{\theta}_i^a = \omega_i^a + \sigma r^a \sin(\psi^a - \theta_i^a) + \lambda \sin(\theta_i^b - \theta_i^a + \alpha), \tag{4.3a}$$

$$\dot{\theta}_i^b = \omega_i^b + \sigma r^b \sin(\psi^b - \theta_i^b) + \lambda \sin(\theta_i^a - \theta_i^b + \alpha), \tag{4.3b}$$

where $i = 1,2,3,\ldots,N$. Now, we assume that $r^a = r^b = r$. As shown later in Section 4.8.1, this is a valid assumption for identical natural frequency distribution for the layers and for high λ values. Furthermore, similar to the mean-field analysis in Chapter 3, a group of synchronized oscillators in layer a and b rotates with some velocity $\dot{\theta}_i^{a(b)} = \dot{\psi}^{a(b)} = \Omega$. With these facts, Eqs. (4.3a) and (4.3b) for a locked oscillator become

$$\Omega = \omega_i^a + \sigma r \sin(\psi^a - \theta_i^a) + \lambda \sin(\theta_i^b - \theta_i^a + \alpha), \tag{4.4a}$$

$$\Omega = \omega_i^b + \sigma r \sin(\psi^b - \theta_i^b) + \lambda \sin(\theta_i^a - \theta_i^b + \alpha). \tag{4.4b}$$

Sum and difference of Eqs. (4.4a) and (4.4b) lead to

$$\begin{aligned} 2\Omega = {} & \omega_i^a + \omega_i^b + 2\sigma r \sin\left(\frac{\psi^a + \psi^b - \theta_i^a - \theta_i^b}{2}\right) \cos\left(\frac{\psi^a - \psi^b + \theta_i^b - \theta_i^a}{2}\right) \\ & + 2\lambda \sin(\alpha) \cos(\theta_i^b - \theta_i^a), \end{aligned} \tag{4.5a}$$

$$\begin{aligned} 0 = {} & \omega_i^a - \omega_i^b + 2\sigma r \cos\left(\frac{\psi^a + \psi^b - \theta_i^a - \theta_i^b}{2}\right) \sin\left(\frac{\psi^a - \psi^b + \theta_i^b - \theta_i^a}{2}\right) \\ & + 2\lambda \cos(\alpha) \sin(\theta_i^b - \theta_i^a). \end{aligned} \tag{4.5b}$$

After putting $\cos\left(\frac{\psi^a + \psi^b - \theta_i^a - \theta_i^b}{2}\right)$ from Eq. (4.5b) in Eq. (4.5a), we get

$$\begin{aligned} & \{\omega_i^b - \omega_i^a + 2\lambda \cos(\alpha) \sin(\Delta\theta_i)\}^2 \cos^2\left(\frac{\Delta\psi - \Delta\theta_i}{2}\right) + \\ & \{2\Omega - \omega_i^b - \omega_i^a - 2\lambda \sin(\alpha) \cos(\Delta\theta_i)\}^2 \sin^2\left(\frac{\Delta\psi - \Delta\theta_i}{2}\right) = \sigma^2 r^2 \sin^2(\Delta\psi - \Delta\theta_i), \end{aligned} \tag{4.6}$$

where $\Delta\psi$ and $\Delta\theta_i$ represent $\psi^a - \psi^b$ and $\theta_i^a - \theta_i^b$, respectively. Now we find the roots of Eq. (4.6). Here onward, we restrict the mean-field analysis to $0 \le \alpha \le \pi/2$ only; however, as explained later in Section 4.5.3, it can be extended to any α value. We further assume that $\psi^a = \psi^b$. Therefore, Eq. (4.6) becomes

$$\begin{aligned}&\{\omega_i^b - \omega_i^a + 2\lambda\cos(\alpha)\sin(\Delta\theta_i)\}^2\cos^2\left(\frac{\Delta\theta_i}{2}\right) + \\ &\{2\Omega - \omega_i^b - \omega_i^a - 2\lambda\sin(\alpha)\cos(\Delta\theta_i)\}^2\sin^2\left(\frac{\Delta\theta_i}{2}\right) - \sigma^2 r^2\sin^2(\Delta\theta_i) = 0. \qquad (4.7)\end{aligned}$$

For $0 \le \alpha < \pi/2$, Eq. (4.7) can be re-written as a sixth order polynomial in $\cos(\theta_i^b - \theta_i^a)$, while it reduces to a third order polynomial at $\alpha = \pi/2$. To our knowledge, the roots of a sixth order polynomial are not known in terms of a formula, so we find its roots numerically. Out of the multiple roots, a physically accepted root is selected as follows: For finite σ values, the L.H.S. of Eq. (4.7) is positive at $\theta_i^b - \theta_i^a = 0, \pm\pi$, suggesting that Eq. (4.6) has even number of roots in the range 0 to $\pm\pi$. Numerically, it can be checked that Eq. (4.7) has two real roots in the range 0 to $\pm\pi$. With λ being fixed, dividing Eq. (4.7) by σ^2 and increasing it infinitesimally shows that $\theta_i^b - \theta_i^a \to 0$ or $\pm\pi$; therefore, the roots closer to 0 should approach towards it. Here we have taken into account the fact that Ω (Eq. (4.15)) remains bounded as σ increases. Since an increase in σ should bring the phases in layer $a(b)$ closer to ψ, and therefore, $\theta_i^b - \theta_i^a$ should decrease, only the roots closer to 0 should be accepted. Next, for $\omega_i^b - \omega_i^a \gtrless 0$, we only take a root such that $\theta_i^b - \theta_i^a \gtrless 0$, which can be justified easily from Eq. (4.5b). It can be re-written as

$$2\sin\left(\frac{\theta_i^b - \theta_i^a}{2}\right)\cos\left(\frac{2\psi - \theta_i^a - \theta_i^b}{2}\right) + \frac{2\lambda\cos(\alpha)\sin\left(\theta_i^b - \theta_i^a\right)}{\sigma r} = \frac{\omega_i^b - \omega_i^a}{\sigma r}. \qquad (4.8)$$

Again, as $\sigma \to \infty$, Eq. (4.8) reveals that either $\theta_i^b - \theta_i^a \to 0$ or $(2\psi - \theta_i^a - \theta_i^b) \to \pm\pi$. Considering only the first case, the roots approach to 0 such that $\theta_i^b - \theta_i^a \gtrless 0$ for $\omega_i^b - \omega_i^a \gtrless 0$. Therefore, out of four roots, a physically accepted root is selected by using these arguments.

Note that, if $\Delta\omega = 0$, $\theta_i^b - \theta_i^a = 0$ is a root of Eq. (4.7). The identical phases of the mirror nodes also justify the impact of $\Delta\omega$ on ES (Figs. 4.2(d)–4.2(f)). The interlayer coupling terms in this case becomes $\lambda\sin(\alpha)$. The addition of a constant term to all oscillators makes the synchronized state for a multiplex network the same as for an isolated network. Since an isolated globally connected network with uniform natural frequency distribution exhibits a discontinuous phase transition without any hysteresis [35], we can expect no hysteresis with a decrease in $\Delta\omega$.

At $\alpha = \pi/2$, as mentioned above, Eq. (4.7) reduces to a third order polynomial $x_i^3 + p_i x_i^2 + q_i x_i + r_i' = 0$, where $x_i = \cos(\theta_i^b - \theta_i^a)$. The coefficients of the polynomial are given by

$$p_i = \frac{-\sigma^2 r^2 - 2\lambda^2 + 2\lambda(\omega_i^a + \omega_i^b - 2\Omega)}{2\lambda^2},$$

$$q_i = \frac{-(\omega_i^b - \omega_i^a)^2 - 4\lambda(\omega_i^a + \omega_i^b - 2\Omega)}{4\lambda^2} + \frac{(\omega_i^a + \omega_i^b - 2\Omega)^2}{4\lambda^2},$$

$$r_i' = \frac{2\sigma^2 r^2 - (\omega_i^b - \omega_i^a)^2 - (\omega_i^a + \omega_i^b - 2\Omega)^2}{4\lambda^2}.$$

And the roots of the polynomial are [74]

$$x_{i_1} = U_i + V_i - \frac{p_i}{3}, \tag{4.9}$$

$$x_{i_2} = -\frac{(U_i + V_i)}{2} + i\frac{\sqrt{3}}{2}\frac{(U_i - V_i)}{2} - \frac{p_i}{3}, \tag{4.10}$$

$$x_{i_3} = -\frac{(U_i + V_i)}{2} - i\frac{\sqrt{3}}{2}\frac{(U_i - V_i)}{2} - \frac{p_i}{3}, \tag{4.11}$$

where U_i and V_i are the same as defined earlier in Eq. (3.20). By calculating x_i values numerically, we demonstrate that the physically accepted root is x_{i_3}. For example, taking $\Delta\omega = 1$, $\omega_i^a = -0.5$, and $\lambda = 1$, we calculate x_i values at $\sigma = 2$ and 20. As $\sigma \to \infty$, $r \to 1$ and $\Omega \to \lambda$; therefore, r, Ω can be taken as $1, \lambda$, respectively. We find that, at $\sigma = 2$, x_{i_1}, x_{i_2}, x_{i_3} are approximately 4.32, -0.19, 0.87, respectively, while at $\sigma = 20$ they are approximately 202, -0.98, 0.99, respectively. The root x_{i_1} is greater than 1, and therefore, it is physically un-acceptable. Out of the remaining two roots, x_{i_2} causes $\theta_i^b - \theta_i^a$ to approach towards $\pm\pi$; hence, it can not be the root as well.

Having achieved $\theta_i^b - \theta_i^a$ value, now we move to Eq. (1.24) to find $r^{a(b)}$ values. A comparison of the real and imaginary terms of Eq. (1.24) leads to

$$r^a = \frac{1}{N}\sum_{locked}\cos(\theta_j^a - \psi^a) + \frac{1}{N}\sum_{drifting}\cos(\theta_j^a - \psi^a), \tag{4.12}$$

$$\sum_{locked}\sin(\theta_j^a - \psi^a) + \sum_{drifting}\sin(\theta_j^a - \psi^a) = 0. \tag{4.13}$$

Here the locked oscillators are those for which Eq. (4.6) has roots, while the remaining are the drifting oscillators. As discussed above, the results are already known at $\Delta\omega = 0$, and therefore, we ignore this case. At $\Delta\omega = 1$, Eq. (4.7) has roots for both natural frequencies $\pm\omega_i^a$, so the locked oscillators are placed symmetrically around the mean value of the natural frequencies. With this fact, the drifting oscillators in Eqs. (4.12) and (4.13) can be neglected in the limit $N \to \infty$ (Appendix A). For $0 < \Delta\omega < 1$, an excellent match between the numerical and analytical calculations (Section 4.8.2) indicate that, here also, we can neglect the drifting oscillators in Eqs. (4.12) and (4.13). Therefore, Eq. (4.12) reduces to

$$r^a = r = \frac{1}{N} \sum_{locked} \cos(\theta_j^a - \psi^a). \tag{4.14}$$

And Eq. (4.13), with the help of Eq. (4.4a), reduces to

$$\Omega = \frac{1}{N_l} \sum_{locked} \{\omega_j^a + \lambda \sin(\theta_j^b - \theta_j^a + \alpha)\}. \tag{4.15}$$

Here N_l represents the total number of locked oscillators. Using Eqs. (4.4a) and (4.7), we find r, Ω values by solving Eqs. (4.14) and (4.15) numerically for $N = 5000$. In the mean field analysis, the larger is N value, the better are the results, but we find that the solutions of Eqs. (4.14) and (4.15) do not show any notable change if we compare them for $N = 1000$ and $N = 5000$. The trianlges in Fig. 4.5(b) represent r values for $N = 1000$, while the continuous green line corresponds to $N = 5000$. The two r values are indistinguishable, suggesting that we can safely take $N = 5000$.

4.5.1 Comparison of Numerical and Analytical Results

Here we compare the predictions from the mean-field analysis with the numerical simulations for $\Delta\omega = 1$ only while Section 4.8.2 presents the comparison for $0 < \Delta\omega < 1$. Although not shown in Fig. 4.5, at $\alpha = 0$, a globally synchronized state exists for all σ values. Eq. (3.12) shows that, at $\sigma = 0$, the natural frequencies of locked oscillator's satisfy the relation $\omega_i^a \le \lambda$; therefore, all oscillators in layer a or b are locked for any $\lambda \ge 0.5$. An increase in σ will only bring the phases closer to each other; hence, the globally synchronized state prevails for all σ values. Considering $\alpha = 0$ case and Figs. 4.5(a)–4.5(f), we can conclude that an increase in α from 0 to $\pi/2$ suppresses the synchronization among the oscillators, and the globally synchronized state converts into an incoherent state. In Figs. 4.5(a)–4.5(c), r^a increases continuously from 0 to 1 by including more and more oscillators in the locked state; a further increase in α turns the phase transition into a discontinuous one (Figs. 4.5(d)–4.5(f)). Interestingly, multiple

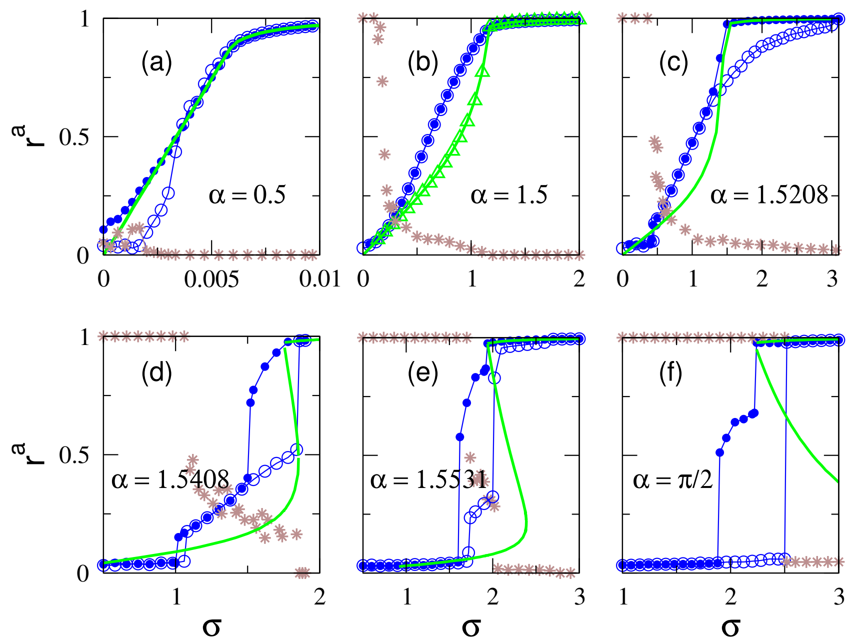

Figure 4.5: (a)-(f) compare r values from mean field analysis (the continuous green lines) with the corresponding r values from numerical simulations (the lines with circles). The stars represent maximum fluctuation in $|\sin(\psi^a - \psi^b)|$ in the forward continuation of σ after the initial transient time is passed. The triangles in (b) represent mean-field predicted r values when Eqs. (4.14) and (4.15) are solved for $N = 1000$. The network parameters in the numerical simulations are $N = 1000$, $\lambda = 10$, and $\Delta\omega = 1$.

$\psi^{a(b)}$ values (and therefore multiple r^f values for the full multiplex network) can exist at $\alpha = \pi/2$ (Section 4.6), where $r^f e^{i\psi^f} = (r^a e^{i\psi^a} + r^b e^{i\psi^b})/2$. However, we do not find any notable difference in the corresponding $r^{a(b)}$ values. Around the bistable regime, the mean field analysis predicts three non-zero r values in Figs. 4.5(d) and 4.5(e) and two non-zero r values in Fig. 4.5(f). Similar to Chapter 3, the upper and lower r values in Figs. 4.5(d) and 4.5(e) should represent the stable synchronized states, while those in the middle should correspond to an unstable state. We mention that we have neglected $r = \Omega = 0$ solution of Eqs. (4.14) and (4.15) for $0 < \alpha \leq \pi/2$. Remember that it can not be a solution at $\alpha = 0$ (Section 3.5.1).

4.5.2 Justification of Discrepancy Between Numerical and Analytical Results

As revealed by Fig. 4.5, the mean-field predictions do not match with the numerical simulations. In the following we justify these discrepancies. Firstly, at $\alpha = 0.5$, Fig. 4.5(a) demonstrates that r^a values for $\sigma \approx 0$ do not match with the mean-field predictions, which is due to the sensitivity of r^a values to initial conditions and not due to failure of the mean-field analysis. Ignoring intralayer coupling terms for $\sigma \approx 0$, the frequency synchronization between the mirror nodes leads to the relation $\sin(\theta_i^b - \theta_i^a) \approx (\omega_i^b - \omega_i^a)/2\lambda\cos(\alpha)$; therefore, synchronization among mirror nodes requires $|\omega_i^a| \leq \lambda\cos(\alpha) \approx 8.77$. $\theta_i^b - \theta_i^a = \theta_i^{b^*} - \theta_i^{a^*}$ is constant (or almost constant) in time for all oscillators and the phases in layer a can be written as $\theta_i^a(t) \approx \int_0^t (\omega_i^a + \lambda\sin(\theta_i^{b^*} - \theta_i^{a^*} + \alpha))dt + \theta_i^a(t=0)$. This relation reveals that, depending on the initial phase distribution, multiple r^a values can exist.

Secondly, as $\alpha \to \pi/2$, r^a values in the partially synchronized state do not match with the numerical simulations. Also, if the unstable state is an indicator of the presence of a hysteresis, the mean-field analysis does not project the position of the hysteresis correctly (Figs. 4.5(d)–4.5(f)). To find the reason behind the failure of the mean-field predictions, we examine the validity of the assumptions. For example, in the forward continuation, we plot the maximum fluctuation in $|\sin(\psi^a - \psi^b)|$ after the initial transient time is passed. The stars in Figs. 4.5(b)–4.5(f) reveal that $\psi^a - \psi^b$ is not constant in the incoherent and partially synchronized regime; therefore, the statements $\psi^a = \psi^b$ and $\dot{\psi}^{a(b)} = \Omega$ do not hold exactly, and a disagreement between the mean-field and the numerical results can occur.

4.5.3 Mean-field Analysis for Other α and λ Values

We mention that a similar mean-field analysis can also be performed for the remaining α values, i.e., for $\pi/2 < \alpha \leq 2\pi$. If $\pi/2 < \alpha < 3\pi/2$, the coefficient of $\sin(\theta_i^{a(b)} - \theta_i^{b(a)})$ is negative and therefore $\psi^a - \psi^b \neq 0$. $\Delta\omega = 0$ case suggests that $\theta_i^b - \theta_i^a = \pm\pi$ and $\psi^a - \psi^b = \pm\pi$ is a solution of Eq. (4.6). For $0 < \Delta\omega \leq 1$, by following a parallel analysis as in Section 4.8.2 one can check that $\psi^a - \psi^b \simeq \pi$; also, the roots of Eq. (4.6) which are closer to $\pm\pi$ should be selected. Likewise, due to the same sign of $\sin(\theta_i^{a(b)} - \theta_i^{b(a)})$ term, the mean-field analysis for $3\pi/2 < \alpha \leq 2\pi$ should remain the same as for $0 \leq \alpha < \pi/2$. Finally, for the only left value of α, i.e., for $\alpha = 3\pi/2$, Section 4.6 next shows that the mean-field analysis is the same as for $\alpha = \pi/2$, only the sign of interlayer coupling term in Eq. 4.17 will change. Mark that here we have performed the mean-field analysis for $\lambda = 10$ only. Fig. 3.6(a) in Chapter 3 compared the mean-field predictions with the numerical simulations for $\alpha = 0$ and $\lambda = 0.1$. A fair agreement there manifests that the mean-field analysis is valid for small λ values as well, as long as $\alpha = 0$ or remains close to it.

4.6 Multi-stability at $\alpha = \frac{\pi}{2}$

We find that, besides $\psi^a = \psi^b$, other relations between ψ^a and ψ^b can also exist if α is $\pi/2$. Multiple $\psi^a - \psi^b$ values at $\alpha = \pi/2$ can exist since there is no attractive coupling (sine coupling) between the layers which can decide the interlayer position of the oscillators. Eqs. (4.1a) and (4.1b) claim that the phases in layers a and b must satisfy the relation

$$\sum_{i=1}^{N}(\theta_i^a - \theta_i^b)_t = \sum_{i=1}^{N}(\theta_i^a - \theta_i^b)_{t=0}. \tag{4.16}$$

Denoting the R.H.S in Eq. (4.16) by k, note that in this Chapter we take $k = 0$, but an addition of $2n\pi$ to k, where $n = \pm 1, \pm 2, \ldots$, does not make any difference physically. Next, in the synchronous state, Eqs. (4.4a) and (4.4b) at $\alpha = \pi/2$ can be re-written as

$$\theta_i^{a(b)} = \psi^{a(b)} - \sin^{-1}\Big\{\frac{\Omega - \omega_i^{a(b)} - \lambda\cos(\theta_i^{b(a)} - \theta_i^{a(b)})}{\sigma r}\Big\}. \tag{4.17}$$

First, we prove the existence of the multiple states for $\Delta\omega = 0,\ 1$. In the first case, Eq. (4.6) shows that $\theta_i^b - \theta_i^a = \psi^b - \psi^a$ is a root. Putting $\theta_i^b - \theta_i^a$ values in Eq. (4.15), it returns $\Omega = \lambda\cos(\psi^b - \psi^a)$. Therefore, Eq. 4.17 becomes

$$\theta_i^{a(b)} = \psi^{a(b)} + \sin^{-1}\big(\frac{\omega_i}{\sigma r}\big), \tag{4.18}$$

where $\omega_i^a = \omega_i^b = \omega_i$. After putting k and $\theta_i^{a(b)}$ values in Eq. (4.16), we get $\psi^a - \psi^b = 2n\pi/N$. For $\Delta\omega = 1$, the natural frequencies satisfy the relation $\omega_i^a = \omega_{N-i+1}^b$, where $i = 1, 2, \ldots, N$. Therefore, from Eq. (4.6), it can be easily perceived that irrespective of the α value, we have $\theta_i^b - \theta_i^a = \theta_{N-i+1}^a - \theta_{N-i+1}^b$. It makes the second term in the R.H.S of Eq. (4.17) same for oscillators of natural frequencies ω_i^a and ω_{N-i+1}^b; therefore, we have $\theta_i^a = \theta_{N-i+1}^b$. With this fact, again putting $\theta_i^{a(b)}$ and k values in Eq. (4.16), we get $\psi^a - \psi^b = 2n\pi/N$. Fig. 4.6 presents some of these states corresponding to $n = 0,\ 1,\ 2,\ -3$ from the numerical simulations. For $0 < \Delta\omega < 1$ also, the same relation between $\psi^{a(b)}$ can be derived in the limit $\sigma \to \infty$. As σ increases, we know that $\theta_i^{a(b)} \to \psi^{a(b)}$; therefore, $\theta_i^b - \theta_i^a \to \psi^b - \psi^a$, which is the same what we found for $\Delta\omega = 0$. Hence, for large σ values, we get the same relation between ψ^a and ψ^b for any $\Delta\omega$ value.

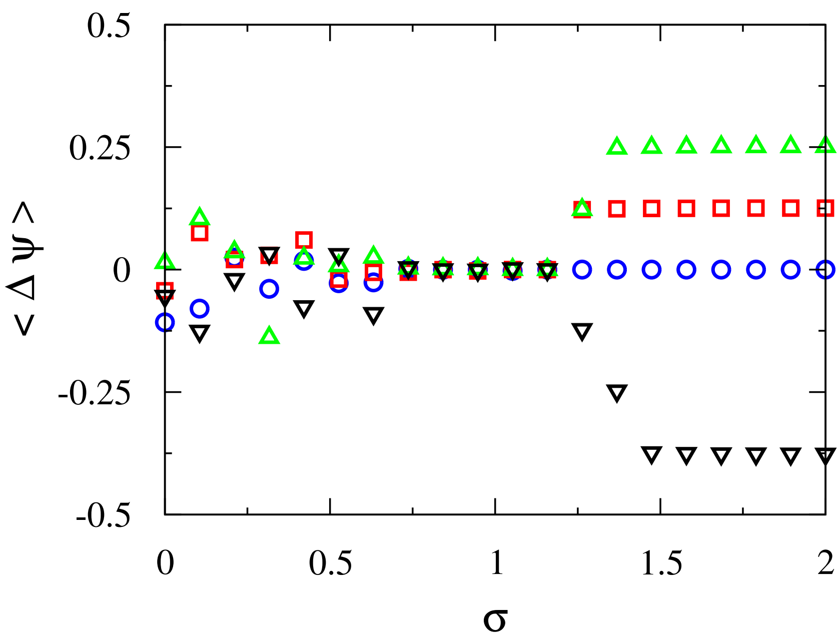

Figure 4.6: The time averaged $\Delta\psi$ ($\psi^a - \psi^b$) values demonstrate multiple synchronized states. The circles, squres, upper-triangles, and lower-triangles correspond to $\Delta\psi = 0$, $\pi/25$, $2\pi/25$, $-3\pi/25$, respectively. The layers are globally connected with $N = 50$, $\lambda = 1$, $\alpha = \pi/2$, and $\Delta\omega = 1$.

4.6.1 Linear Stability Analysis in the Limit $\sigma \to \infty$

By performing a linear stability analysis for the globally synchronous state, we prove that the multiple states represented by $\psi^a - \psi^b = 2n\pi/N$, where $i = 1, 2, \ldots, N$, are stable in the limit $\sigma \to \infty$. Rewriting Eqs. (4.1a) and (4.1b) for $\alpha = \pi/2$, we get

$$\dot{\theta}_i^a = \omega_i^a + \frac{\sigma}{N}\sum_{j=1}^{N}\sin(\theta_j^a - \theta_i^a) + \lambda\cos(\theta_i^b - \theta_i^a), \tag{4.19a}$$

$$\dot{\theta}_i^b = \omega_i^b + \frac{\sigma}{N}\sum_{j=1}^{N}\sin(\theta_j^b - \theta_i^b) + \lambda\cos(\theta_i^a - \theta_i^b). \tag{4.19b}$$

Now, we give a small perturbation to each phase, i.e., $\theta_i^{a*} \to \theta_i^{a*} + \varepsilon_i^a$, $\theta_i^{b^*} \to \theta_i^{b^*} + \varepsilon_i^b$, were θ_i^{a*} and $\theta_i^{b^*}$ are the phases of i^{th} node in the globally synchronous state. A Taylor expansion of Eqs. (4.19a) and (4.19b) around the fixed point, with considering only the first order terms in $\varepsilon_i^{a(b)}$, leads to

$$\begin{aligned}\dot{\varepsilon}_i^a = \frac{\sigma}{N}\sum_{j=1}^{N}\cos(\theta_j^{a*} - \theta_i^{a*})\varepsilon_j^a - \frac{\sigma}{N}\sum_{j=1}^{N}\cos(\theta_j^{a*} - \theta_i^{a*})\varepsilon_i^a - \lambda\varepsilon_i^b\sin(\theta_i^{b^*} - \theta_i^{a*}) \\ +\lambda\varepsilon_i^a\sin(\theta_i^{b^*} - \theta_i^{a*}),\end{aligned} \tag{4.20a}$$

$$\dot{\varepsilon}_i^b = \frac{\sigma}{N}\sum_{j=1}^{N}\cos(\theta_j^{b*}-\theta_i^{b*})\varepsilon_j^b - \frac{\sigma}{N}\sum_{j=1}^{N}\cos(\theta_j^{b*}-\theta_i^{b*})\varepsilon_i^b - \lambda\varepsilon_i^a\sin(\theta_i^{a*}-\theta_i^{b*}) \\ +\lambda\varepsilon_i^b\sin(\theta_i^{a*}-\theta_i^{b*}). \tag{4.20b}$$

Eqs. (4.20a) and (4.20b) can be re-written in a short form as

$$\dot{\varepsilon} = J\varepsilon. \tag{4.21}$$

Here J represents a Jacobian matrix of size $2N \times 2N$. For a better presentation, we denote the fixed point $(\theta_1^{a*},\ldots,\theta_N^{a*},\theta_1^{b*},\ldots,\theta_N^{b*})$ by $(\theta_1^*,\ldots,\theta_N^*,\theta_{N+1}^*,\ldots,\theta_{2N}^*)$. Eqs. (4.20a) and (4.20b) suggest that the non-diagonal intralayer entries of the Jacobian are such that $J_{ij} = (\sigma/N)\cos(\theta_j^* - \theta_i^*)$, where $i,j = 1,2,\ldots,N$ for the links in layer a, and $i,j = N+1,N+2,\ldots,2N$ for the links in layer b. The interlayer entries are such that $J_{i,i+N} = -J_{i+N,i} = -\lambda\sin(\theta_{i+N}^* - \theta_i^*)$, where $i = 1,2,\ldots,N$ and 0 otherwise. Finally, the diagonal entries are $J_{ii} = -\sum_{j=1,j\neq i}^{2N} J_{ij}$, where $i = 1,2,\ldots,2N$. Now, as $\sigma \to \infty$, intra and interlayer entries approach σ/N and $\pm\lambda\sin(\psi^b - \psi^a)$, respectively. It can be easily checked that the eigenvalues of the Jacobian matrix are $0,0,-\sigma,-\sigma,...,-\sigma$. Since the Jacobian is a zero-row sum matrix, the entries of the eigenvector corresponding to the eigenvalue 0 are all 1. Note that independence of Jacobian eigenvalues from the interlayer entries is perhaps due to the opposite signs in them, i.e., $J_{i,i+N} = -J_{i+N,i}$, which makes the trace of the matrix independent of the interlayer entries, hinting that the eigenvalues should not depend on the orientation of ψ^a and ψ^b.

Now, we solve Eq. (4.21) to see whether the perturbations decay or grow in time. As discussed in Section 1.3, let say a transformation from the coordinates ε_i to η_i is such that

$$\varepsilon = E\eta, \tag{4.22}$$

where E is a matrix whose columns contain eigenvectors of the Jacobian eigenvalues. Putting Eq. (4.22) in Eq. (4.21) and after applying E^{-1} on both sides, we get

$$\dot{\eta} = E^{-1}JE \;\; \eta. \tag{4.23}$$

$E^{-1}JE$ is a diagonal matrix with diagonal elements representing the Jacobian eigenvalues. So the solution of Eq. (4.23) for an i^{th} variable is $\eta_i = \eta_i(t=0)e^{\lambda_i t}$, where λ_i denotes an eigenvalue. If $J_{11} = J_{22} = 0$, as $t \to \infty$, we get $\eta_1(t) = \eta_1(t=0)$ and $\eta_2(t) = \eta_2(t=0)$ while all other η_i will decay to zero. Therefore, from Eq. (4.22), we get $\varepsilon_i = \eta_1 + \eta_2 \ \forall \ i$. Which means that, as $t \to \infty$, $\theta_i^{a*} \to \theta_i^{a*} + \eta_1 + \eta_2$ and $\theta_i^{b*} \to \theta_i^{b*} + \eta_1 + \eta_2$. A constant term has been added to all phases in the fixed point state. Since Eqs. (4.1a) and (4.1b) are invariant with respect to a constant shift in all the phases, the multiple states represented by $\psi^a - \psi^b = 2n\pi/N$ are linearly stable.

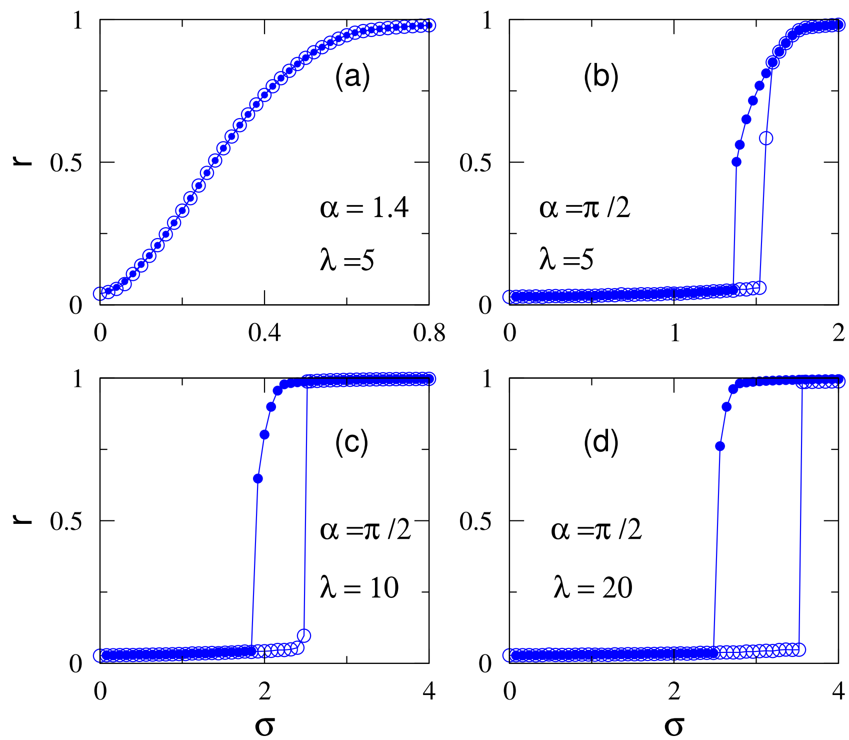

Figure 4.7: (a) and (b) show the emergence of ES due to a phase shift in the single layer network given by Eq. 4.24. (c) and (d) show a favourable impact of λ on hysteresis size. The network size (N) in all the figures is 1000.

4.7 An Extension to Single Networks

As shown later in Section 4.8.1, the phases in the synchronized state at $\Delta\omega = 1$ satisfy the relation $\theta_i^a = \theta_{N-i+1}^b$, which shows that a phase-shifted coupling between the opposite natural frequencies of a single network should also result in an ES. Therefore, the model should be

$$\dot{\theta}_i = \omega_i + \frac{\sigma}{N} \sum_{\substack{j=1 \\ j \neq N-i+1}}^{N} \sin(\theta_j - \theta_i) + \lambda \sin(\theta_{N-i+1} - \theta_i + \alpha), \tag{4.24}$$

where $\omega_i = -\omega_{N-i+1}$ and $i = 1, 2, \ldots, N$ (even). Eq. (4.24), infact, represents a globally connected network of heterogeneous couplings. Fig. 4.7 reveals that, indeed, the model presented by Eq. (4.24) exhibits ES along with a hysteresis. Figs. 4.7(c) and 4.7(d) further show that, similar to the multiplex networks, an increase in λ has a favorable impact on the hysteresis width. Other choices of natural frequencies for phase-shifted couplings and their impact on ES may be explored further elsewhere. The obtained results here demonstrate that our results are framework independent.

4.8 Validity of the Assumptions

In this section, we justify the assumptions that have been used throughout this Chapter.

4.8.1 Validity for $\Delta\omega = 0, 1$

Except the time dependence of $\psi^{a(b)}$ or $r^{a(b)}$ as $\alpha \to \pi/2$, the assumptions (a) $r^a = r^b$ and (b) $\psi^a = \psi^b$ are valid. First we discuss the case of $0 \leq \alpha < \pi/2$. For $\Delta\omega = 0$, we have $\theta_i^a = \theta_i^b$ (Eq. (4.7)), and therefore, the assumptions (a) and (b) are valid from Eq. (1.24). For $\Delta\omega = 1$, as discussed earlier in Section 4.6, we have $\omega_i^a = \omega_{N-i+1}^b$, where $i = 1, 2, \ldots, N$. Eq. (4.7) suggests that $\theta_i^b - \theta_i^a = -(\theta_{N-i+1}^b - \theta_{N-i+1}^a)$; therefore, Eqs. (4.4a) and (4.4b) return $\theta_i^a = \theta_{N-i+1}^b$. Since the distribution of phases is identical for layers a and b, the assumptions (a) and (b) are valid. Finally, we prove that the only assumption (a) is valid at $\alpha = \pi/2$. Eq. (4.18) reveals that $\psi^a - \theta_i^a = \psi^b - \theta_i^b$ (for $\Delta\omega = 0$), while Eqs. (4.4a) and (4.4b) lead to $\psi^a - \theta_i^a = \psi^b - \theta_{N-i+1}^b$ (for $\Delta\omega = 1$). Therefore, Eq. (1.24) returns $r^a = r^b$.

4.8.2 Validity for $0 < \Delta\omega < 1$

For $0 < \Delta\omega < 1$, with the help of the numerical simulations and by showing a good match between the numerical and mean field predicted r values, we demonstrate that the assumptions (a) $r^a = r^b$, (b) $\psi^a = \psi^b$, and (c) the exclusion of drifting oscillators in Eqs. (4.14) and (4.15) are valid. Since $\psi^{a(b)}$ starts depending on time as $\alpha \to \pi/2$, here we prove the validity of the assumptions only for α values far from $\pi/2$. Note that, for $0 \leq \alpha < \pi/2$, the assumptions (a) and (b) are motivated from the fact that an increase in λ increases the *sine* coupling between the mirror nodes which causes $\theta_i^a \to \theta_i^b$, and therefore, $r^a \to r^b$ and $\psi^a \to \psi^b$.

Figs. 4.8(a)–4.8(d) demonstrate that there is no visible difference between r^a and r^b values from the numerical simulations, validating the assumption $r^a = r^b$. Further-

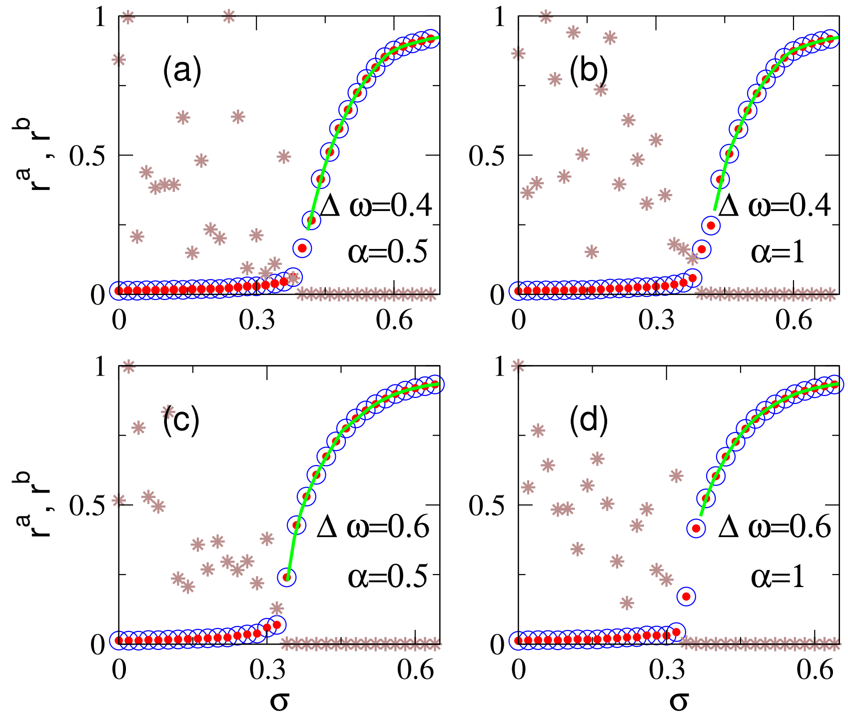

Figure 4.8: (a)-(d) show a comparison of r^a (the open blue circles) and r^b (the filled red circles) values from the numerical simulations. The stars represent maximum fluctuation in $|\sin(\psi^a - \psi^b)|$ after the initial transient time is passed. The continuous green lines represent mean-field predicted r^a values. In both the numerical and analytical calculations, the multiplex networks contain globally connected layers with $N = 5000$ and $\lambda = 10$.

more, the analytically predicted r values are in excellent agreement with the numerical ones. The stars in Figs. 4.8(a)–4.8(d) reveal that the assumption (b) also holds in the synchronized regime.

For assumption (c), only based on the excellent agreement between the numerical and mean-field predicted r values, we claim that the exclusion of drifting oscillators is a fair choice. Also, mark that the drifting oscillators decrease as $r \to 1$, and therefore, assumption (c) holds automatically for large r values.

As demonstrated by Figs. 4.8(a)–4.8(d), Eqs. (4.14) and (4.15) do not have any solution for small r values. A possible cause behind this observation can be as follows: If we compare the R.H.S. in Eq. (4.15) for layers a and b, the terms $\sum \omega_i^{a(b)}$ and $\sum \sin(\theta_i^{b(a)} - \theta_i^{a(b)})$ may not be same for a very small number of locked oscillators and for a finite N value, indicating the non-validity of the statement $\dot{\psi}^{a(b)} = \Omega$. We hope that, in the limit $N \to \infty$, one may observe an averaging over these terms, making their values same for both layers. Furthermore, we find that the R.H.S. of Eqs. (4.14) and (4.15) is not a smooth function for a very small r value, so multiple solutions of Eqs. (4.14) and (4.15) can exist. While plotting Figs. 4.8(a)–4.8(d), we have selected only the largest of multiple r values for $0 < r \lesssim 0.3$. Remember that, if $\Delta\omega = 0, 1$, the R.H.S. of Eqs. (4.14) and (4.15) is smooth for all r values because the locked oscillators add to the synchronized state systematically, i.e., smaller natural frequencies synchronize first and than the larger ones. It is due to this reason we primarily focused on the mean-field analysis only for $\Delta\omega = 1$.

4.9 Conclusion

While different techniques have been proposed in the past years to incite ES in connected phase oscillators, none of them presents a phase shift as a parameter responsible for ES. We have demonstrated that a phase shift in interlayer coupling terms of a multiplex network of Kuramoto oscillators triggers ES in the layers. As $\alpha \to \pi/2$, ES emerges along with a hysteresis. The different parameters, i.e., the phase shift, the interlayer coupling strength, and the natural frequency mismatch between the mirror nodes, governing the hysteresis width are discussed in detail. The robustness of the ES against changes in the network topology and natural frequency distribution has been tested as well. Homogeneous random networks manifest a significant jump in the phase transition, while for the heterogeneous networks the jump size is negligible. A strong discontinuity in the phase transition for globally connected layers suggests that an increase in the average connectivity of the layers should have a favorable impact on the jump size, and therefore, heterogeneous layers may show a sizable jump for sufficient high average connectivity. Our mean-field analysis shows a fair agreement with the numerical simulations if the α value remains close to 0. By extending the results to single networks, we have hinted that the basic framework of networks is within the reach of the phase-shift α to achieve ES.

Since Sakaguchi and Kuramoto proposed the phase-shifted coupling in 1986, extensive work on phase-shifted Kuramoto oscillators on single networks proves their relevance to real-world systems (Section 1.4.3). The proposed interlayer phase-shifted model in this Chapter may be relevant to real systems. One such example comes from neural networks. It has been found that the neural dynamics represented by Wilson-

Cowan oscillators can be reduced to a multilayer network of Kuramoto oscillators having phase-shifted interlayer couplings [23, 85].

Chapter 5

Explosive Synchronization in Frequency Displaced Multiplex Networks

5.1 Introduction

As discussed in the earlier Chapters also, the field where the multiplex framework has become particularly important is network neuroscience. The description of brain networks in terms of multilayer structures has very recently helped in revealing how the anatomical layer relates to the functional one [29, 86] and in the development of frequency-based brain networks [87]. In the last description, the different frequency bands of the original signal (that can be correlated to different functions) are used separately to construct a multilayer functional network that offers a deep insight into the relationship between structure, functioning, and dynamics of the brain. Taking motivation from these examples, in this Chapter we investigate if explosive synchronization can be induced in a two-layer multiplex network of Kuramoto oscillators where the natural frequencies in the layers are displaced. It turns out that a sufficient natural frequency mismatch between two layers incites ES in the layers. The displacement between the natural frequencies frustrates the formation of the giant cluster, eventually giving birth to ES.

5.2 Model

We consider a multiplex network of two layers—each one containing N Kuramoto oscillators. The angular velocity of an i^{th} oscillator in layer $a(b)$ is given by

$$\dot{\theta}_i^a = \omega_i^a + \sigma^a \sum_{j=1}^{N} A_{ij}^a \sin(\theta_j^a - \theta_i^a) + \sigma^{ab} \sin(\theta_i^b - \theta_i^a), \tag{5.1a}$$

$$\dot{\theta}_i^b = \omega_i^b + \sigma^b \sum_{j=1}^{N} A_{ij}^b \sin(\theta_j^b - \theta_i^b) + \sigma^{ab} \sin(\theta_i^a - \theta_i^b). \tag{5.1b}$$

Here $\sigma^{a(b)}$ represents intralayer coupling among the oscillators in layer $a(b)$, while σ^{ab} represents the interlayer coupling strength. Initial phases of the oscillators in layer $a(b)$ are chosen from a uniform random distribution in the range $-\pi \leq \theta_i^{a(b)} \leq \pi$. Similarly, the natural frequencies of the oscillators in layer $a(b)$ are also chosen from a uniform random distribution in the range $\omega_i^{a(b)}$=$[\omega_o^{a(b)} - \delta\omega, \omega_o^{a(b)} + \delta\omega]$. The parameter $\Delta\omega = \omega_o^b - \omega_o^a$ represents the mismatch between the mean values of the natural frequencies in the layers, while $\delta\omega$ denotes the dispersion among natural frequencies in each layer. Natural frequencies to oscillators in layer $a(b)$ and the interlayer links are assigned randomly, which ensures that there is no preferred correlation between natural frequencies and degrees of the mirror nodes. Throughout the Chapter, we choose the mean natural frequencies symmetric around zero, i.e., $\omega_o^{a(b)} = -(+)\Delta\omega/2$. Additionally, σ^b is kept fixed, while $\sigma^a = \sigma^{ab} = \sigma$ is varied.

5.3 Natural Frequency Displacement Between the Layers Provokes ES

We find that a sufficient natural frequency mismatch between the layers turns a continuous phase transition into a discontinuous one. This can be observed from Fig. 5.1(a), which plots the values of r^b when the layers have ER topologies. For increasing values of $\Delta\omega$, the system transits from a second-order like synchronization transition to a hybrid transition, where the initially continuous transition ends in a discontinuous and irreversible phase transition. The sudden change in the nature of the phase transition happens when the order parameter reaches $r^b \simeq 0.5$, and we also observe a hysteresis loop whose width increases with $\Delta\omega$. Notice that σ^b remains unchanged at a small value much below the synchronization threshold for the isolated layer, but the multiplexation

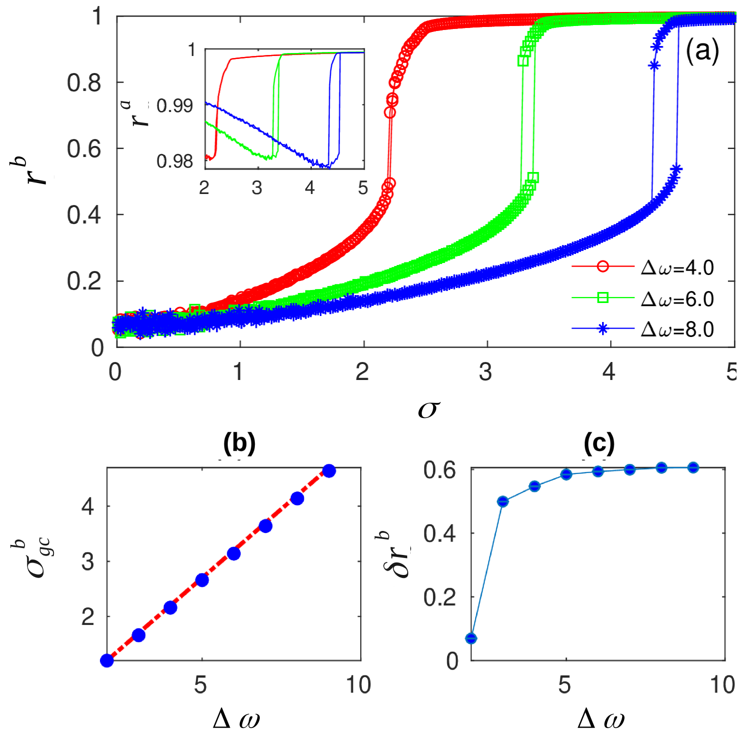

Figure 5.1: (a) Dependence of order parameter r^b on σ for several values of $\Delta\omega$. The inset shows r^a vs σ. (b) Numerically observed backward critical coupling σ^b_{gc} as a function of $\Delta\omega$ (the blue dots) and the corresponding theoretical prediction (the dotted red line). (c) The maximal jump δr^b in the order parameter vs $\Delta\omega$. In all these figures, the multiplex network consists of two ER layers with $N = 200$, $\langle k^a \rangle = 3$, $\langle k^b \rangle = 6$, $\sigma^b = 0.01$, and $\delta\omega = 0.5$.

allows indirect coupling and therefore increases the phase coherence. As can be seen from the inset in Fig. 5.1(a), at the same value of σ, layer a also jumps to full synchrony through a discontinuous transition. Having a stronger intralayer coupling strength, layer a is already close to complete intralayer synchronization (i.e., $r^a \approx 1$) when the sudden transition occurs. The blue dots in Fig. 5.1(b) display that the backward critical coupling (σ^b_{gc}) for the explosive transition depends linearly on detuning $(\Delta\omega/2) + \delta\omega$ (the dotted red line), which will be derived later in Section 5.6. Fig. 5.1(c) plots the dependence of the largest jump size on $\Delta\omega$, evaluated as $\delta r^b = max(r^b(\sigma + \delta\sigma) - r^b(\sigma))$, the maximal difference in the order parameter for two consecutive values of coupling σ and $\sigma + \delta\sigma$ along the backward transition. Large values of δr^b correspond to a sharp ES, while smaller ones indicate the evolution towards a second order transition. The increase in δr^b reflects that the change in the nature of the phase transition occurs progressively.

Along with $\Delta\omega$ value, we find that the hysteresis width is also sensitive to dispersion

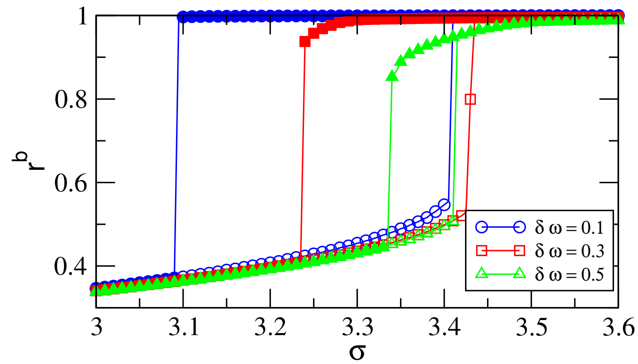

Figure 5.2: The dependence of order parameter r^b on σ for increasing values of natural frequency dispersion $\delta\omega$. The layers are ER networks with $N = 200$, $\langle k^a \rangle = \langle k^b \rangle = 6$, $\sigma^b = 0.001$ and $\Delta\omega = 6.0$.

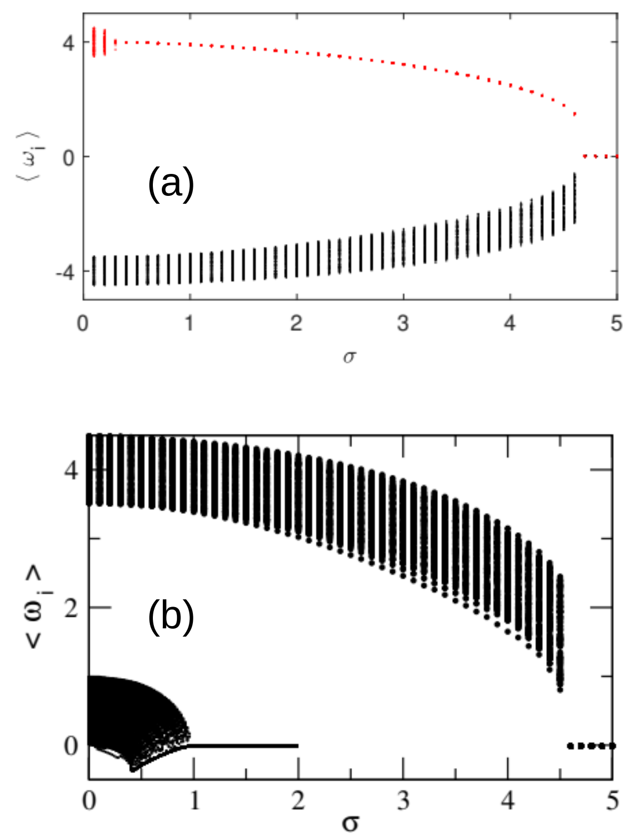

Figure 5.3: (a) The distribution of time averaged frequencies $\langle \omega_i \rangle$ vs σ at $\Delta\omega = 8.0$. The red (black) dots represent oscillators in layer $a(b)$. (b) The distribution of $\langle \omega_i \rangle$ in layer b with respect to σ at $\Delta\omega = 1$ and 8. The network parameters are the same as in Fig. 5.1.

$\delta\omega$ in the natural frequencies (Fig. 5.2). To show this, we fix $\Delta\omega$ at some value and vary the $\delta\omega$ value. While the forward critical coupling remains almost unaffected, a smaller

$\delta\omega$ value decreases the threshold of the transition to backward desynchronization, and therefore, the hysteresis width increases. Thus, a larger $\Delta\omega$ and a smaller $\delta\omega$ both are in favor of ES.

During the continuous part of the phase transition, the time averaged instantaneous frequencies of oscillators ($\langle\omega_i\rangle$) suffer a slow drift before suddenly collapsing to the mean natural frequency $\bar{\omega}$ (Fig. 5.3(a)). As depicted by Fig. 5.3(b), for $\Delta\omega = 1$, the spread in $\langle\omega_i\rangle$ in layer b decreases with an increase in σ, while for $\Delta\omega = 8$ the spread even increases a little bit until all $\langle\omega_i\rangle$ suddenly jump to the mean natural frequency. These observations confirm that a sufficiently large natural frequency mismatch between the layers suppresses the formation of a giant cluster in layer b [88].

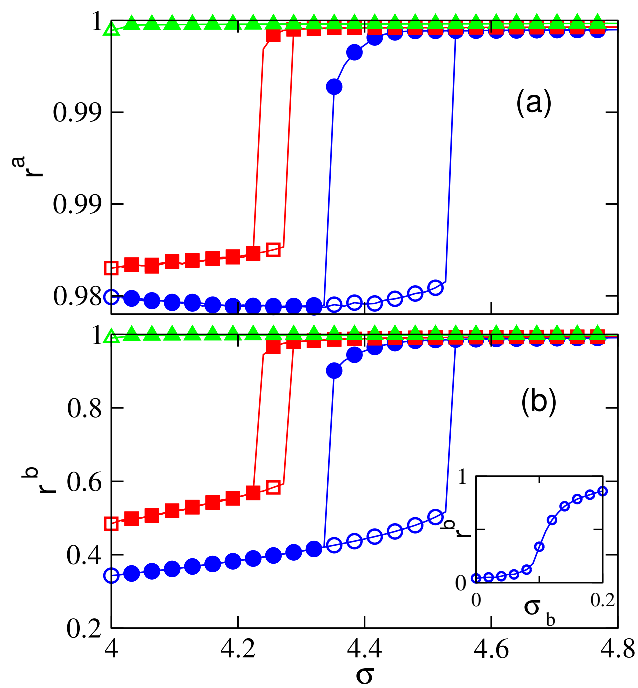

Figure 5.4: The dependence of order parameters r_a and r^b on σ when $\sigma^b = 0.01$ (the circles), $\sigma^b = 0.1$ (the squares), and $\sigma^b = 1$ (the triangles). The multiplex network consists of two ER layers of $N = 500$, $\langle k^a\rangle = \langle k^b\rangle = 6$, $\delta\omega = 0.5$, and $\Delta\omega = 8.0$.

5.4 Different Coupling Arrangements and ES

5.4.1 ES for Different σ^b Values

Fixing σ^b at a small value is essential to achieve ES. We find that ES disappears if we increase the σ^b value. As depicted from the inset of Fig. 5.4(b), in isolation, layer $a(b)$

attains a globally synchronous state for a coupling value around 0.2. In the multiplex case also, we find that r^a reaches to a value close to 1 around the same intralayer coupling value; therefore, the jump size in r^a cannot be large (Fig. 5.4(a)), whereas layer b exhibits a significant jump with an increase in σ (Fig. 5.4(b)). With an increase in σ^b, the order parameter of layer b increases and the jump size in ES as well as the hysteresis width both decreases, getting extinct as σ^b attains a sufficiently large value (Fig. 5.4(b)). The extinction of ES or hysteresis with increasing σ^b values should be due to the fact that the oscillators in layer b do not feel the suppression of synchronization caused by the natural frequency mismatch.

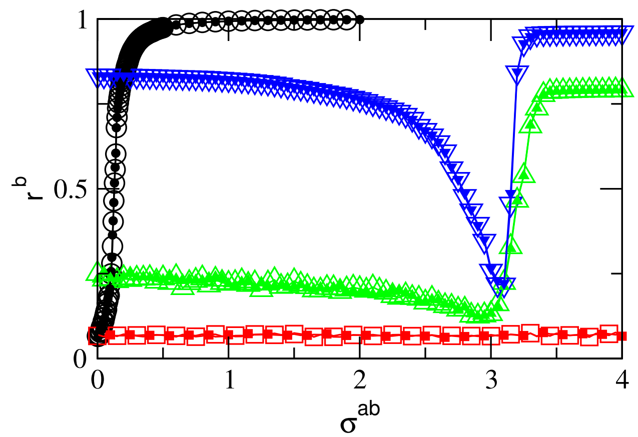

Figure 5.5: r^b vs σ^{ab} for the cases of $\sigma^a = \sigma^b = \sigma^{ab}$ (the circles), $\sigma^a = \sigma^b = 0.01$ (the squares), $\sigma^a = \sigma^b = 0.1$ (the upper triangles), and $\sigma^a = \sigma^b = 0.2$ (the lower triangles). The layers are ER networks with $N = 200$, $\langle k^a \rangle = \langle k^b \rangle = 6$, $\delta\omega = 0.5$, and $\Delta\omega = 6.0$.

5.4.2 Equal Intralayer Couplings

We find that ES does not exist for a homogeneous arrangement of the couplings as well, i.e., $\sigma^a = \sigma^b = \sigma^{ab} = \sigma$ (Fig. 5.5). The same is also observed for the case of symmetric intralayer couplings when $\sigma^a = \sigma^b$ is fixed at some value while σ^{ab} is varied. To show this, we explore the evolution to coherence with respect to σ^{ab} for three values of fixed $\sigma^a = \sigma^b$. The chosen values are representative of three different regimes for the isolated layer: incoherent, intermediate, and coherent regime. At $\sigma^{a(b)} = 0.01$, none of the layers depicts any synchrony in isolation, which was also observed earlier in the inset of Fig. 5.4(b). As multiplexing is introduced, it has no impact on the synchronization behavior of the individual layers for such a small intralayer coupling. At an intermediate coupling, i.e., $\sigma^{a(b)} = 0.1$, an increase in σ^{ab} leads to a smooth synchronization in both

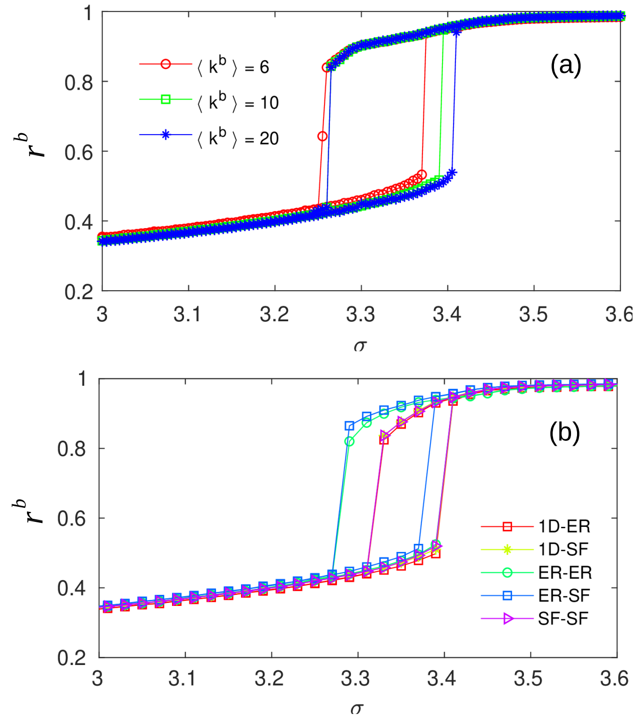

Figure 5.6: (a) Order parameter r^b vs σ for several values of $\langle k^b \rangle$. The multiplex network consists of ER-SF networks with $N = 200$, $\langle k^a \rangle = 4$, $\sigma^b = 0.01$, $\delta\omega = 0.5$, and $\Delta\omega = 6.0$. (b) Order parameter r^b vs σ for several combinations of intralayer topologies: including 1D, ER, and SF networks. Here $\langle k^b \rangle = 6$ and the rest of parameters are the same as in (a).

the layers. This transition to synchronization as a consequence of multiplexing was also shown in [89]. Finally, when $\sigma^{a(b)} = 0.2$, a value which is high enough to observe synchronization in the isolated layers, the multiplexing enhances the phase coherence in both the layers, but the increase in synchrony is mediated by desynchronization, which was also reported earlier in Ref. [90].

5.5 Robustness of ES

As we saw in the last section, the ES exists only for a specific arrangement of couplings, i.e., when $\sigma^a = \sigma^{ab}$ and σ^b is small. Taking this coupling arrangement in this Section we explore the dependence of ES on different network parameters, i.e., the average connectivity, network topology, and the number of interlayer links.

We find that ES does not depend on the difference in the average degrees of the layers. We show this fact in Fig. 5.6(a) by varying the value of $\langle k^b \rangle$ while conserving the rest of the network parameters. Fig. 5.6(a) manifests that, even for $\langle k^b \rangle >> \langle k^a \rangle$,

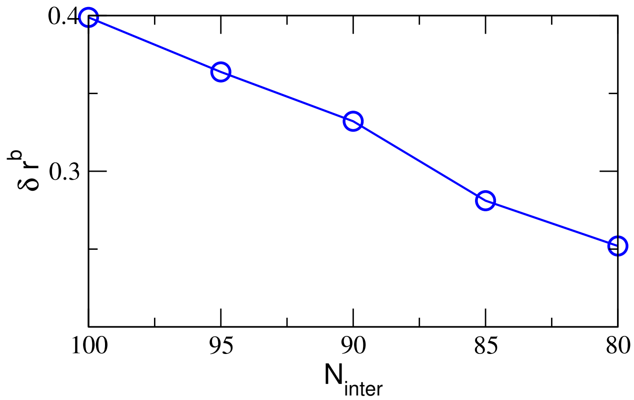

Figure 5.7: In the forward continuation of σ, the figure presents the maximal jump (δr^b) in order parameter with respect to the number of interlinks (N_{inter}). The layers are ER networks with $N = 100$, $\langle k^a \rangle = \langle k^b \rangle = 4$. The parameters $\delta\omega$, and $\Delta\omega$ are the same as in Fig. 5.6. The interlinks are removed randomly while demultiplexing.

the phase transition remains discontinuous. Next, we check that the explosive transition is unaffected by the intralayer topology. Fig. 5.6(b) provides the order parameter r^b for several combinations of the intralayer topologies—including 1D network, ER network, and Barabasi-Albert's SF network. The critical couplings and the positions of hysteresis are very similar in all the cases where $\langle k^a \rangle$ and $\langle k^b \rangle$ are maintained. The robustness of ES against changes in intralayer topology may be arising due to the following fact: σ^b is very small; therefore, the particular topology of layer b is not very relevant as witnessed in Fig. 5.6(b). On the other hand side, layer a is very close to intralayer synchronization as $\sigma^a = \sigma^{ab} = \sigma$ is very large; therefore, it may be treated as a single oscillator for large σ values (see Fig. 5.3(a) where all dots for layer a are almost one-pointed). Thus, the topology of layer a should also have an insignificant impact on ES.

Finally, we check the robustness of ES against a change in the number of interlayer links because the condition of full multiplexation is a very strong one and may not be found in real-world systems [91]. We check this by removing the interlayer links one by one and recalculating the jump size. An example of the process is shown in Fig. 5.7 where δr^b is plotted as a function of the remaining interlayer links N_{inter}; δr^b decreases continuously along with the demultiplexing, suggesting the ES character does not disappear suddenly and a small percentage of interlayer links can be removed from the network.

Note that the numerical simulations in this Chapter are performed for $N = 100$, 200, and 500, hinting that the size of layers should not be a factor in achieving ES—the phenomenon depends only on the mismatch between the natural frequencies.

5.6 Backward Critical Coupling

Using a mean-field analysis, we derive the backward critical coupling σ_{gc}^b. For a multiplex network of two arbitrary layers, Eqs. (5.1a) and (5.1b) can be rewritten as

$$\dot{\theta}_i^a = \omega_i^a + \sigma k_i^a r_i^a \sin(\psi_i^a - \theta_i^a) + \sigma \sin(\theta_i^b - \theta_i^a), \tag{5.2a}$$

$$\dot{\theta}_i^b = \omega_i^b + \sigma^b k_i^b r_i^b \sin(\psi_i^b - \theta_i^b) + \sigma \sin(\theta_i^a - \theta_i^b), \tag{5.2b}$$

where we have already considered $\sigma^a = \sigma^{ab} = \sigma$. $r_i^{a(b)}$ in Eqs. (5.2a) and (5.2b) is a local order parameter for an i^{th} node in layer $a(b)$. It is defined as

$$r_i^{a(b)} e^{i\psi_i^{a(b)}} = \frac{1}{k_i^{a(b)}} \sum_{j=1}^{N} A_{ij}^{a(b)} e^{i\theta_j^{a(b)}}, \tag{5.3}$$

where $k_i^{a(b)}$ is the degree of the i^{th} node in layer $a(b)$, i.e., $k_i^{a(b)} = \sum_{j=1}^{N} A_{ij}^{a(b)}$. In the globally synchronized state, we have $\dot{\theta}_i^{a(b)} = \bar{\omega} \; \forall \; i$. As mentioned earlier, the natural frequency distribution for the full multiplex network is symmetric around 0, i.e., $\bar{\omega} = 0$. Therefore, the globally synchronous state is a fixed point state. Now, Eqs. (5.2a) and (5.2b) can be re-written as

$$\theta_i^a = \psi_i^a + \sin^{-1}\left\{\frac{\omega_i^a + \sigma \sin(\theta_i^b - \theta_i^a)}{\sigma k_i^a r_i^a}\right\}, \tag{5.4a}$$

$$\theta_i^b = \psi_i^b + \sin^{-1}\left\{\frac{\omega_i^b + \sigma \sin(\theta_i^a - \theta_i^b)}{\sigma^b k_i^b r_i^b}\right\}. \tag{5.4b}$$

Using Eqs. (5.2a) and (5.4a), we obtain

$$\theta_i^a = \psi_i^a + \sin^{-1}\left\{\frac{\omega_i^a + \omega_i^b + \sigma^b k_i^b r_i^b \sin(\psi_i^b - \theta_i^b)}{\sigma k_i^a r_i^a}\right\}. \tag{5.5}$$

While Eq. (5.4b) can be rewritten as

$$\theta_i^b = \theta_i^a + \sin^{-1}\left\{\frac{\omega_i^b + \sigma^b k_i^b r_i^b \sin(\psi_i^b - \theta_i^b)}{\sigma}\right\}. \tag{5.6}$$

Since σ^b is very small and $r^b \approx 1$ (and therefore $\psi_i^b \approx \theta_i^b$) in the synchronous state, this implies that $\sigma^b \sin(\psi_i^b - \theta_i^b) << 1$. Therefore, we can neglect the term $\sigma^b k_i^b r_i^b \sin(\psi_i^b - \theta_i^b)$ in Eq. (5.6). It suggests that $\sigma \geq \sigma_{gc}^b = max|\omega_i^b|$, which is the minimum σ value below which the globally synchronous state can not exist. In our numerical simulations, the natural frequencies in layer b are in the range $\omega_i^b = [\Delta\omega/2 - \delta\omega, \Delta\omega/2 + \delta\omega]$; therefore, we can estimate the backward critical coupling as $\sigma_{gc}^{b} \approx \Delta\omega/2 + \delta\omega$. We check our predictions in Fig. 5.1(b) (the red dotted line); even if the network is relatively small and sparse and hence it is far from the thermodynamic limit, the analytical prediction provides a fair approximation of σ_{gc}^{b} values.

Mark that, while the backward continuation of σ, r^b may show jump at a lower σ value than σ_{gc}^{b}. For example, exact frequency synchronization in Fig. 5.2 (for $\delta\omega = 0.5$) is not possible below $\sigma = 3.5$ (neglecting the second term in the numerator of Eq. 5.6), whereas r^b shows a backward jump at $\sigma \approx 3.35$. We find that, at a given $\Delta\omega$ value, the difference between the coupling values at which frequency and phase desynchronization take place decreases with decreasing $\delta\omega$ values (Fig. 5.2).

With $\delta\omega$ being fixed, an increase in $\Delta\omega$ leads to an increase in σ; therefore, Eqs. (5.5) and (5.6) hint that $\theta_i^a \to \psi_i^a$ and $\theta_i^b \to \theta_i^a + \sin^{-1}\frac{\omega_i^b}{\sigma}$. From Eq. (5.3), it follows that $\psi_i^a \approx \psi_j^a \approx \psi \;\forall\; i,j$. Therefore, r^a and r^b should increase, demonstrating a favourable impact of increase in $\Delta\omega$ on ES. Notice that for the special case of $\sigma^b = 0$ and for symmetric natural frequencies of the mirror nodes, i.e., for $\omega_i^a + \omega_i^b = 0$, Eqs. (5.5) and (5.6) suggest that all the phases are confined within $\pi/2$ angular distance; therefore, the synchronized state is linearly stable as well [92]. We can also calculate r^b values from the mean-field analysis. Eqs. (5.2a) and (5.2b) demand that

$$\sum_{j=1}^{N} (\theta_j^a + \theta_j^b)_t = (\theta_j^a + \theta_j^b)_{t=0} = k. \tag{5.7}$$

Since we have $\theta_i^a \approx \psi \;\forall\; i$, and $\theta_i^b = \theta_i^a + \sin^{-1}(\omega_i^b/\sigma)$. Putting these values in Eq. (5.7) with $k = 0$, we get $\psi = -\frac{1}{2N}\sum_{j=1}^{N}\sin^{-1}(\omega_j^b/\sigma)$. At $\Delta\omega = 6$, $\delta\omega = 0.1$, $\sigma_{gc}^{b} = 3.1$, and for the considered natural frequency distribution in Fig. 5.2, Eq. (1.24) returns $r^b = 0.996$. The predicted r^b value is in fair agreement with the numerical one in Fig. 5.2.

5.7 Conclusion

The synchronization of oscillators in an ensemble with multi-modal natural frequency distribution has attracted increasing interest very recently [93, 94]. It is useful for the description of biological collectives where interaction between different frequencies of dynamical processes occurs [26, 95]. In this Chapter we have shown that a sufficient natural frequency mismatch between the layers generates explosive synchronization in multiplex networks. The natural frequency mismatch creates a mutual frustration in the completion of the synchronization process, generating a hybrid transition without requiring any specific structure-dynamics correlation. The specific coupling arrangement to achieve ES is discussed—it turned out that intralayer coupling strength for layer *b* should be small enough. The phenomenon is insensitive to the structure and average degree; also, it is robust against demultiplexing of a few interlayer links.

Chapter 6

Conclusions and Discussion

Most of the studies on synchronization and explosive synchronization so far are limited to single networks where all links are of the same type. However, as we discussed in Section 1.6, the same set of nodes can have different types of interactions among them. The multiplex framework can accommodate each type of interaction in different layers, and therefore, offers a correct representation of such systems.

For identical phase oscillators, we have discussed in detail the impact of degree-degree correlations among intralayer and mirror nodes on the GS of multiplex networks. Our work shows that by keeping the layers unaltered one can change the GS of sparse multiplex networks by simply tuning the degree-degree correlations among the mirror nodes. While λ_N remains constant, it is λ_2 (or the algebraic connectivity of the network) that determines the changes in GS. We have also shown that, depending on the degree-degree correlations, the functionality of GS with respect to changing connectivity can be drastically different than the GS of the classical single networks. During the initial increase in connectivity, degree-degree correlations determine whether λ_N or λ_2 will rule the overall changes in λ_N/λ_2. However, after some value of average connectivity, the GS decreases irrespective of degree-degree correlations because the multiplex structure itself puts a cap on λ_2 while λ_N can increase continuously with increasing connectivity.

For non-identical phase oscillators on multiplex networks, we have presented three techniques to induce ES in the layers and they are interlayer adaptation, interlayer phase-shifted interactions, and natural frequency displacement between the layers. In our all encounters with ES, it appeared along with a hysteresis. Our numerical calculations as well as analytical predictions both verify that suppression of synchronization propels the ensemble towards discontinuity. The different factors governing the width of hysteresis are discussed in detail. As witnessed in Chapters 3 and 4, the interlayer coupling strength and the natural frequency mismatch between the mirror nodes (in Chapter 5 as well) are two key parameters that can turn a continuous phase transition into a discontinuous one or vice versa. Note that since the ES in Chapter 3 arises due to the interlayer links, its properties are also different than the earlier observed ES due to intralayer links [32]. Firstly, the interlayer adaptation does not require the presence of r^2 in the coupling terms. Secondly, the ES is sensitive to natural frequency assignment among the mirror nodes. In the limit $N \to \infty$, the factor $r^a r^b$ leaves the forward critical coupling unchanged. To the best of our knowledge, we are the first to report ES due to a phase shift in the couplings. The extension of our results to classical single networks widens the scope of the technique to achieve ES in single networks.

We have tried to generalize the results by testing the robustness of ES against different network parameters. While the ES in Chapter 5 is robust against all network typologies, Chapters 3 and 4 reveal that ES prevails only in random topologies having a homogeneous degree distribution. For heterogeneous single networks, it has been observed that a partially synchronous state grows continuously from almost zero coupling value [12]; perhaps the models in Chapters 3 and 4 could not suppress the gradual increase in synchronization, and hence, they failed to incite ES in these networks.

Wherever possible, a mean-field analysis has been performed to justify the numerical simulations. Identical intralyer couplings and natural frequency distributions for the layers in Chapters 3 and 4 made it possible to take $r^a = r^b$ and $\psi^a = \psi^b$, which in turn simplified the mean-field analysis a lot. Remember that, as mentioned in Section 4.8.2, the mean-field analysis does not predict any r value close to 0 if $0 < \Delta\omega < 1$. Hence, a detailed mean-field analysis plotting all r values from 0 to 1 could be applied for $\Delta\omega = 0, 1$ only. The first case turned out to be trivial, and therefore, did not give us any new insight. We hope that—for $0 < \Delta\omega < 1$ also—the smaller r values may be achieved for a sufficient large N value.

Next, we discuss some potential extensions of our findings. The phase-shifted interactions in Section 4.7 were assigned to some specific links only; other choices of links for the phase-shifted couplings and their impact on ES may be a potential subject for further investigation. Likewise, the synchronized state for $\Delta\omega = 1$ in Chapter 3 also hints that a similar extension to single networks is possible there as well. As we observed in Chapter 5, the removal of a small fraction of interlayer links does not have much impact on ES; we hope our results of Chapters 3 and 4 should also be robust against the removal of a small fraction of the interlayer links, suggesting the relevance of our results to the more general multilayer networks. Note that different types of interactions were at the core of our need to switch to the multiplex framework. But for the ease of the mean-field applicability, we only focused on symmetric layers in Chapters 3 and 4 where intralayer couplings, natural frequency distributions, and coupling functions remained the same for both the layers. The robustness of our results against changes in these parameters may be worthy to explore. One such example of different dynamical rules for the layers could be the first-order Kuramoto dynamics on one layer and the second-order dynamics [53] on another layer. Lastly, an extension of the results from two to general M layers and from phase oscillators to more general oscillators, i.g, Stuart Landau oscillators having amplitude dynamics, can be a few more potential extensions.

The phenomenon of synchronization is ubiquitous, from a simple setup of synchronized coupled pendulums to the coherent firing of neurons in extremely complex neural systems. Furthermore, the discontinuous phase transitions are very intriguing due to the wealth of new phenomena they carry with them. The abnormal hypersensitivity in discontinuous phase transitions is undesired in several real-world systems (Section 1.8), so the need for control over them inspires us to explore their underlying causes thoroughly. As mentioned at appropriate places in different Chapters, we hope the multiplex models presented in the thesis are relevant to real-world systems. In conclusion, from fundamental understanding to applicability to real systems, we hope the thesis will strengthen our current understanding of synchronization and explosive synchronization on the novel multiplex framework.

Appendices

Appendix A

Contribution of Drifting Oscillators to the Order Parameter

We prove that the drifting oscillators can be neglected in Eq. (3.10). The assumption that $r^{a(b)}$ and $\psi^{a(b)}$ are time independent in the limit $N \to \infty$ suggests that we can look for steady state solutions. Similar to the single networks [14], conservation of oscillators leads to following continuity equations for layers a and b

$$\frac{\partial \rho^{a(b)}}{\partial t} = -\frac{\partial (\rho^{a(b)} v^{a(b)})}{\partial \theta^{a(b)}}, \tag{A.1}$$

where $\rho^{a(b)}(\theta^a, \theta^b, \omega^{a(b)}, t)$ is the probability of finding an oscillator having natural frequency ω^a, phase θ^a, and its mirror node's phase being θ^b. $v^{a(b)}$ is the angular velocity given by Eqs. (3.5a) and (3.5b). $\rho^{a(b)}(\theta^a, \theta^b, \omega^{a(b)}, t)$ satisfy the normalization condition

$$\int_{-\pi}^{\pi}\int_{-\pi}^{\pi} \rho^{a(b)}(\theta^a, \theta^b, \omega^{a(b)}) d\theta^a d\theta^b = 1. \tag{A.2}$$

In the steady state regime, $\frac{\partial \rho^{a(b)}}{\partial t} = 0$; therefore, the solution of Eq. (A.1) for the drifting oscillators is such that

$$\rho^{a(b)} = \frac{C(\omega^{a(b)})}{|v^{a(b)}|}. \tag{A.3}$$

Here $C(\omega^{a(b)})$ is a constant, which is determined from the relation

$$C(\omega^{a(b)}) = \left\{ \int_{-\pi}^{\pi}\int_{-\pi}^{\pi} \frac{1}{|v^{a(b)}|} d\theta^a d\theta^b \right\}^{-1}. \tag{A.4}$$

With $\rho^{a(b)}$ given by Eq. (A.3), it follows that the integral version of second term in the R.H.S. of Eq. (3.10) is such that

$$r_d^a e^{i\psi_d^a} = \int_{-\pi}^{\pi}\int_{-\pi}^{\pi}\int_{|\omega^a|>\gamma_c} \frac{C(\omega^a)e^{i\theta^a}g(\omega^a)d\theta^a d\theta^b d\omega^a}{|\omega^a - \sigma r\sin(\theta^a) + \lambda A\ \sin(\theta^b - \theta^a)|}. \tag{A.5}$$

Breaking the integration over ω^a in Eq. (A.5) in two parts such that

$$\begin{aligned} r_d^a e^{i\psi_d^a} = &\int_{-\pi}^{\pi}\int_{-\pi}^{\pi}\int_{-0.5}^{-\gamma_c} \frac{C(\omega^a)e^{i\theta^a}g(\omega^a)d\theta^a d\theta^b d\omega^a}{|\omega^a - \sigma r\sin(\theta^a) + \lambda A\ \sin(\theta^b - \theta^a)|} \\ &+ \int_{-\pi}^{\pi}\int_{-\pi}^{\pi}\int_{\gamma_c}^{0.5} \frac{C(\omega^a)e^{i\theta^a}g(\omega^a)d\theta^a d\theta^b d\omega^a}{|\omega^a - \sigma r\sin(\theta^a) + \lambda A\ \sin(\theta^b - \theta^a)|}. \end{aligned} \tag{A.6}$$

The γ_c in Eqs. (A.5) and (A.6) is equal to the R.H.S. of Eq. (3.12). Additionally, $g(-\omega^a) = g(\omega^a)$, $\rho^a(\theta^a + \pi, \theta^b, -\omega^a) = \rho^a(\theta^a, \theta^b, \omega^a)$, and $e^{i(\theta^a+\pi)} = -e^{i(\theta^a)}$. Similar to the single networks [14], it can be checked that the first term in the R.H.S. of Eq. (A.6) is negative to the second term; therefore, we get $r_d^a = 0$. Note that the outcome $r_d^a = 0$ makes $r^{a(b)}$ and $\psi^{a(b)}$ constant in time.

Appendix B

Forward Critical Coupling

From linear stability analysis of the incoherent state $r^{a(b)} = 0$, we derive σ_c^f values observed in Fig. 3.8. Eq. (A.4) shows that, if $r^{a(b)} = 0$, $C(\omega^{a(b)}) = 1/(4\pi^2)$. Putting this in Eq. (A.3), we get $\rho^{a(b)} = 1/(4\pi^2)$. Now, we give a small perturbation to this state, which leads to

$$\rho^{a(b)}(\theta^a, \theta^b, \omega^{a(b)}) = \frac{1}{4\pi^2} + \varepsilon^{a(b)}\eta^{a(b)}(\theta^a, \theta^b, \omega^{a(b)}),$$

where $\varepsilon^{a(b)} << 1$. Furthermore, Eq. (1.24) changes to

$$r^{a(b)}e^{i\psi^{a(b)}} = \int_{-\pi}^{\pi}\int_{-\pi}^{\pi}\int_{-0.5}^{0.5}\Big(\frac{1}{4\pi^2} + \varepsilon^{a(b)}\eta^{a(b)}(\theta^a, \theta^b, \omega^{a(b)})\Big)e^{i\theta^{a(b)}}g(\omega^{a(b)})d\theta^a d\theta^b d\omega^{a(b)}. \tag{B.1}$$

The first term on the R.H.S. of Eq. (B.1) is 0, while the second term can be rewritten as $\varepsilon^{a(b)}r^{a(b)'}e^{i\psi^{a(b)}}$. Therefore, $r^{a(b)} = \varepsilon^{a(b)}r^{a(b)'}$. With this fact, putting $\rho^{a(b)}$ and $v^{a(b)}$ in Eq. (A.1) leads to

$$\frac{\partial}{\partial t}\Big\{\frac{1}{4\pi^2} + \varepsilon^{a(b)}\eta^{a(b)}(\theta^a, \theta^b, \omega^{a(b)})\Big\} = -\frac{\partial}{\partial \theta^{a(b)}}\Big\{\Big(\frac{1}{4\pi^2} + \varepsilon^{a(b)}\eta^{a(b)}(\theta^a, \theta^b, \omega^{a(b)})\Big) \\ \Big(\omega^{a(b)} + \sigma\varepsilon^{a(b)}r^{a(b)'}\sin(\psi^{a(b)} - \theta^{a(b)}) + \lambda\varepsilon^a\varepsilon^b r^{a\prime}r^{b\prime}\sin(\theta^{b(a)} - \theta^{a(b)})\Big)\Big\}. \tag{B.2}$$

Since $\varepsilon^{a(b)} << 1$, the terms containing $\{\varepsilon^{a(b)}\}^2$ and $\varepsilon^a\varepsilon^b$ will be even smaller, so we can neglect them. With this, we get

$$\frac{\delta\eta^{a(b)}}{\delta t} = -\frac{\sigma r^{a(b)'}\cos(\psi^{a(b)} - \theta^{a(b)})}{4\pi^2} - \omega^{a(b)}\frac{\delta\eta^{a(b)}}{\delta\theta^{a(b)}}. \tag{B.3}$$

Note that η^a and η^b are independent of each other. Eq. (B.3) is the same as studied earlier by Ref. [73], except that 2π in Eq. 2.12 of Ref. [73] is now replaced by $4\pi^2$. So we prove that this change does not affect the stability criteria. Since $\eta^{a(b)}(\theta^a, \theta^b, \omega^{a(b)})$ is 2π periodic in θ^a and θ^b, we can write it in terms of Fourier series as

$$\eta^{a(b)}(\theta^a, \theta^b, \omega^{a(b)}) = \sum_{m=-\infty}^{+\infty} \sum_{n=-\infty}^{+\infty} c_{m,n}^{a(b)}(\omega^{a(b)}, t) e^{im\theta^a} e^{in\theta^b} \tag{B.4}$$

Where $c_{m,n}^{a(b)}$ are given by

$$c_{m,n}^{a(b)} = \frac{1}{4\pi^2} \int_{-\pi}^{\pi} \int_{-\pi}^{\pi} \eta^{a(b)}(\theta^a, \theta^b, \omega^{a(b)}) e^{-im\theta^a} e^{-in\theta^b} d\theta^a d\theta^b \tag{B.5}$$

Eq. (A.2) ensures that $c_{0,0}^{a(b)}$ is 0. Also, $c_{-1,0}^{a(b)} = c_{1,0}^{a(b)^*}$ and $c_{0,-1}^{a(b)} = c_{0,1}^{a(b)^*}$. Now, we calculate the first term on the R.H.S. of Eq. (B.3). For that, we first calculate $r^{a(b)'} e^{\psi^{a(b)}}$. Rewriting Eq. (B.1) as

$$r^{a(b)'} e^{i\psi^{a(b)}} = \int_{-\pi}^{\pi} \int_{-\pi}^{\pi} \int_{-0.5}^{0.5} \Big(\sum_{m=-\infty}^{+\infty} \sum_{n=-\infty}^{+\infty} c_{m,n}^{a(b)}(\omega^{a(b)}, t) e^{im\theta^a} e^{in\theta^b} \Big) e^{i\theta^{a(b)}} g(\omega^{a(b)}) d\theta^a d\theta^b d\omega^{a(b)}. \tag{B.6}$$

For layer a, the integration in Eq. (B.6) survives for $m = -1$ and $n = 0$ only, and we get

$$r^{a\prime} e^{i\psi^a} = 4\pi^2 \int_{-0.5}^{0.5} c_{-1,0}^{a}(\omega^a, t) g(\omega^a) d\omega^a. \tag{B.7}$$

Similarly, the term containing $c_{0,-1}$ survives for layer b. Since the real part of a complex function f can be rewritten as $\frac{f+f^*}{2}$, we can write

$$\frac{\sigma r^{a\prime} \cos(\psi^a - \theta^a)}{4\pi^2} = \frac{\sigma\{(r^{a\prime} e^{i\psi^a} e^{-i\theta^a}) + (r^{a\prime} e^{i\psi^a} e^{-i\theta^a})^*\}}{8\pi^2}. \tag{B.8}$$

Except that coefficient $c_{\pm 1}$ of the Fourier series is now replaced by $c_{\pm 1,0}^{a}$, Eq. (B.8) is the same what was derived earlier from the third term in the R.H.S. of Eq. 2.12 in Ref. [73]. From here onward, we can proceed in the same manner as followed by Ref. [73]. Therefore, the linear stability analysis for the incoherent state predicts $\sigma_c^f = 2/(\pi g(\bar{\omega}))$, here $g(\bar{\omega})$ is the value of probability distribution function $g(\omega)$ at the mean value of natural frequencies.

References

[1] Newman M. E. J. (2010), Networks: an introduction, Oxford University Press, New York (ISBN:9780199206650).

[2] Albert R. and Barabási A.-L. (2002), Statistical mechanics of complex networks, Rev. Mod. Phys. **74**, 47-97 (DOI:10.1103/RevModPhys.74.47).

[3] Erdös P. and Rényi A. (1959), On random graphs, Publ. Math. Debrecen **6**, 290-297.

[4] Barabási A.-L. and Albert R. (1999), Emergence of Scaling in Random Networks, Science **286**, 509-512 (DOI:10.1126/science.286.5439.509).

[5] Dorogovtsev S. N. and Mendes J. F. F. (2000), Evolution of networks with aging of sites, Phys. Rev. E **62**, 1842-1845 (DOI:10.1103/PhysRevE.62.1842).

[6] Barahona M. and Pecora L. M. (2002), Synchronization in Small-World Systems, Phys. Rev. Lett. **89**, 054101 (DOI:10.1103/PhysRevLett.89.054101).

[7] Mattuck A. (2011), Decoupling Systems, available at: `https://math.mit.edu/~jorloff/suppnotes/suppnotes03/ls4.pdf`

[8] Eroglu D. *et al.* (2017), Synchronisation of chaos and its applications, Contemporary Physics **58**, 207-243 (DOI:10.1080/00107514.2017.1345844).

[9] Wiener N. (1958), Nonlinear Problems in Random Theory, MIT Press, Cambridge, MA (ISBN:9780262230049).

[10] Wiener N. (1961), Cybernetics, 2nd Edition, MIT Press, Cambridge, MA (ISBN:9780262230070).

[11] Winfree A. T. (1967), Biological Rhythms and the Behavior of Populations of Coupled Oscillators, J. Theoret. Biol. **16**, 15-42 (DOI:10.1016/0022-5193(67)90051-3).

[12] Arenas A. *et al.* (2008), Synchronization in complex networks, Phys. Rep. **469**, 93-153 (DOI:10.1016/j.physrep.2008.09.002).

[13] Kuramoto Y. (1984), Chemical Oscillations, Waves, and Turbulence, Springer, Berlin (ISBN:13:978-3-642-69691-6).

[14] Strogatz S. H. (2000), From Kuramoto to Crawford: exploring the onset of synchronization in populations of coupled oscillators, Physica D **143**, 1-20 (DOI:10.1016/S0167-2789(00)00094-4).

[15] Sakaguchi H. and Kuramoto Y. (1986), A Soluble Active Rotater Model Showing Phase Transitions via Mutual Entertainment, Prog. Theor. Phys. **76**, 576-581 (DOI:10.1143/PTP.76.576).

[16] Ott E. and Antonsen T. M. (2008), Low dimensional behavior of large systems of globally coupled oscillators, Chaos: An Interdisciplinary Journal of Nonlinear Science **18**, 037113 (DOI:10.1063/1.2930766).

[17] Hannay K. M. (2017), Macroscopic Models and Phase Resetting of Coupled Biological Oscillators, Ph.D. Dissertation, University of Michigan.

[18] Acebron J. A. *et al.* (2005), The Kuramoto model: A simple paradigm for synchronization, Rev. Mod. Phys. **77**, 137-185 (DOI:10.1103/RevModPhys.77.137).

[19] English L. Q. *et al.* (2016), Emergence and analysis of Kuramoto-Sakaguchi-like models as an effective description for the dynamics of coupled Wien-bridge oscillators, Phys. Rev. E **94**, 062212 (DOI:10.1103/PhysRevE.94.062212).

[20] Lohe M. A. (2015), Synchronization control in networks with uniform and distributed phase lag, Automatica **54**, 114-123 (DOI:10.1016/j.automatica.2015.01.034).

[21] Kivelä M. *et al.* (2014), Multilayer networks, Journal of Complex Networks **2**, 203-271 (DOI:10.1093/comnet/cnu016).

[22] Nicosia V. and Latora V. (2015), Measuring and modeling correlations in multiplex networks, Phys. Rev. E **92**, 032805 (DOI:10.1103/PhysRevE.92.032805).

[23] Sadilek M. and Thurner S. (2015), Physiologically motivated multiplex Kuramoto model describes phase diagram of cortical activity, Sci Rep **5**, 10015 (DOI:10.1038/srep10015).

[24] Buldyrev S. V. *et al.* (2010), Catastrophic cascade of failures in interdependent networks, Nature **464**, 1025-1028 (DOI:10.1038/nature08932).

[25] Granell C. *et al.* (2013), Dynamical Interplay between Awareness and Epidemic Spreading in Multiplex Networks, Phys. Rev. Lett. **111**, 128701 (DOI:10.1103/PhysRevLett.111.128701).

[26] Nicosia V. *et al.* (2017), Collective Phenomena Emerging from the Interactions between Dynamical Processes in Multiplex Networks, Phys. Rev. Lett. **118**, 138302 (DOI:10.1103/PhysRevLett.118.138302).

[27] Gómez S. *et al.* (2013), Diffusion Dynamics on Multiplex Networks, Phys. Rev. Lett. **110**, 028701 (DOI:10.1103/PhysRevLett.110.028701).

[28] Soriano-Paños D. *et al.* (2019), Explosive transitions induced by interdependent contagion-consensus dynamics in multiplex networks, Phys. Rev. E **99**, 062311 (DOI:10.1103/PhysRevE.99.062311).

[29] Domenico M. D. *et al.* (2016), Mapping Multiplex Hubs in Human Functional Brain Networks, Frontiers in Neuroscience **10**, 326 (DOI:10.3389/fnins.2016.00326).

[30] Zhao D.-W. *et al.* (2016), The robustness of multiplex networks under layer node-based attack, Sci Rep **6**, 24304 (DOI:10.1038/srep24304).

[31] Solé-Ribalta A. *et al.* (2016), Congestion Induced by the Structure of Multiplex Networks, Phys. Rev. Lett. **116**, 108701 (DOI:10.1103/PhysRevLett.116.108701).

[32] Zhang X. *et al.* (2015), Explosive Synchronization in Adaptive and Multilayer Networks, Phys. Rev. Lett. **114**, 038701 (DOI:10.1103/PhysRevLett.114.038701).

[33] Boccaletti S. *et al.* (2016), Explosive transitions in complex networks' structure and dynamics: Percolation and synchronization, Phys. Rep. **660**, 1-94 (DOI:10.1016/j.physrep.2016.10.004).

[34] D'Souza R. M. *et al.* (2019), Explosive phenomena in complex networks, Advances in Physics **68**, 123-223 (DOI:10.1080/00018732.2019.1650450).

[35] Pazó, D. (2005), Thermodynamic limit of the first-order phase transition in the Kuramoto model, Phys. Rev. E **72**, 046211 (DOI:10.1103/PhysRevE.72.046211).

[36] Adhikari, B. M. *et al.* (2013), Localizing epileptic seizure onsets with Granger causality, Phys. Rev. E **88**, 030701 (DOI:10.1103/PhysRevE.88.030701).

[37] Lee U. *et al.* (2018), Functional Brain Network Mechanism of Hypersensitivity in Chronic Pain, Sci Rep **8**, 243 (DOI:10.1038/s41598-017-18657-4).

[38] Kumar P. *et al.* (2015), Experimental evidence of explosive synchronization in mercury beating-heart oscillators, Phys. Rev. E **91**, 062909 (DOI:10.1103/PhysRevE.91.062909).

[39] Leyva I. *et al.* (2012), Explosive First-Order Transition to Synchrony in Networked Chaotic Oscillators, Phys. Rev. Lett. **108**, 168702 (DOI:10.1103/PhysRevLett.108.168702).

[40] Kim M. *et al.* (2015), Functional and Topological Conditions for Explosive Synchronization Develop in Human Brain Networks with the Onset of Anesthetic-Induced Unconsciousness, Frontiers in Computational Neuroscience **10**, 1 (DOI:10.3389/fncom.2016.00001).

[41] Kim M. *et al.* (2017), Relationship of Topology, Multiscale Phase Synchronization, and State Transitions in Human Brain Networks, Frontiers in Computational Neuroscience **11**, 55 (DOI:10.3389/fncom.2017.00055).

[42] Gómez-Gardeñes J. *et al.* (2011), Explosive Synchronization Transitions in Scale-Free Networks, Phys. Rev. Lett. **106**, 128701 (DOI:10.1103/PhysRevLett.106.128701).

[43] Zhang X. *et al.* (2013), Explosive synchronization in a general complex network, Phys. Rev. E **88**, 010802 (DOI:10.1103/PhysRevE.88.010802).

[44] Leyva I. *et al.* (2013), Explosive synchronization in weighted complex networks, Phys. Rev. E **88**, 042808 (DOI:10.1103/PhysRevE.88.042808).

[45] Xiao Y. *et al.* (2017), Synchronization of phase oscillators in the generalized Sakaguchi-Kuramoto model, Europhys. Lett. **118**, 60005 (DOI:10.1209/0295-5075/118/60005).

[46] Khanra P. *et al.* (2020), Amplification of explosive width in complex networks, Chaos: An Interdisciplinary Journal of Nonlinear Science **30**, 031101 (DOI:10.1063/5.0003410).

[47] Skardal P. S. *et al.* (2014), Disorder induces explosive synchronization, Phys. Rev. E **89**, 062811 (DOI:10.1103/PhysRevE.89.062811).

[48] Hong H. and Strogatz S. H. (2011), Kuramoto Model of Coupled Oscillators with Positive and Negative Coupling Parameters: An Example of Conformist and Contrarian Oscillators, Phys. Rev. Lett. **106**, 054102 (DOI:10.1103/PhysRevLett.106.054102).

[49] Skardal, P. S. and Arenas A. (2019), Abrupt Desynchronization and Extensive Multistability in Globally Coupled Oscillator Simplexes, Phys. Rev. Lett. **122**, 248301 (DOI:10.1103/PhysRevLett.122.248301).

[50] Danziger M. M. *et al.* (2019), Dynamic interdependence and competition in multilayer networks, Nature Physics **15**, 178-185 (DOI:10.1038/s41567-018-0343-1).

[51] Khanra P. *et al.* (2018), Explosive synchronization in phase-frustrated multiplex networks, Phys. Rev. E **98**, 052315 (DOI:10.1103/PhysRevE.98.052315).

[52] Kachhvah A. D. *et al.* (2020), Interlayer Hebbian plasticity induces first-order transition in multiplex networks, New J. Phys. **22**, 122001 (DOI:10.1088/1367-2630/abcf6b).

[53] Kachhvah A. D. and Jalan S. (2017), Multiplexing induced explosive synchronization in Kuramoto oscillators with inertia, Europhys. Lett. **119**, 60005 (DOI:10.1209/0295-5075/119/60005).

[54] Jalan S. *et al.* (2019), Inhibition-induced explosive synchronization in multiplex networks, Phys. Rev. E **99**, 062305 (DOI:10.1103/PhysRevE.99.062305).

[55] Kachhvah A. D. and Jalan S. (2019), Delay regulated explosive synchronization in multiplex networks, New J. Phys. **21**, 015006 (DOI:10.1088/1367-2630/aaff0e).

[56] Newman M. E. J. (2002), Assortative Mixing in Networks, Phys. Rev. Lett. **89**, 208701 (DOI:10.1103/PhysRevLett.89.208701).

[57] Newman M. E. J. (2003), Mixing patterns in networks, Phys. Rev. E **67**, 026126 (DOI:10.1103/PhysRevE.67.026126).

[58] Barnardo M. D. *et al.* (2007), Effects of degree correlation on the synchronization of networks of oscillators, International Journal of Bifurcation and Chaos **17**, 3499-3506 (DOI:10.1142/S0218127407019263).

[59] Min B. *et al.* (2014), Network robustness of multiplex networks with interlayer degree correlations, Phys. Rev. E **89**, 042811 (DOI:10.1103/PhysRevE.89.042811).

[60] Nie S. *et al.* (2015), Effect of degree correlation on exact controllability of multiplex networks, Physica A: Statistical Mechanics and its Applications **436**, 98-102 (DOI:10.1016/j.physa.2015.05.038).

[61] Lee K.-M. *et al.* (2012), Correlated multiplexity and connectivity of multiplex random networks, New J. Phys. **14**, 033027 (DOI:10.1088/1367-2630/14/3/033027).

[62] Arruda G. F. D. *et al.* (2016), On degree–degree correlations in multilayer networks, Physica D: Nonlinear Phenomena **323-324**, 5-11 (DOI:10.1016/j.physd.2015.11.004).

[63] Xulvi-Brunet R. and Sokolov I. M. (2004), Reshuffling scale-free networks: From random to assortative, Phys. Rev. E. **70**, 066102 (DOI:10.1103/PhysRevE.70.066102).

[64] Nishikawa T. *et al.* (2003), Heterogeneity in Oscillator Networks: Are Smaller Worlds Easier to Synchronize?, Phys. Rev. Lett. **91**, 014101 (DOI:10.1103/PhysRevLett.91.014101).

[65] Aguirre J. *et al.* (2014), Synchronization of Interconnected Networks: The Role of Connector Nodes, Phys. Rev. Lett. **112**, 248701 (DOI:10.1103/PhysRevLett.112.248701).

[66] Jalan S. *et al.* (2016), Interplay of degree correlations and cluster synchronization, Phys. Rev. E. **94**, 062202 (DOI:10.1103/PhysRevE.94.062202).

[67] Fiedler M. (1973), Algebraic connectivity of graphs, Czechoslovak Mathematical Journal **23**, 298-305.

[68] Pikovsky A. *et al.* (2003), Synchronization A universal concept in nonlinear sciences, Cambridge University Press, New York (ISBN:9780521592857).

[69] Parshani R. *et al.* (2011), Inter-similarity between coupled networks, Europhys. Lett. **92**, 68002 (DOI:10.1209/0295-5075/92/68002).

[70] Zhou C. and Kurths J. (2006), Dynamical Weights and Enhanced Synchronization in Adaptive Complex Networks, Phys. Rev. Lett. **96**, 164102 (DOI:10.1103/PhysRevLett.96.164102).

[71] Gutiérrez R. *et al.* (2011), Emerging Meso- and Macroscales from Synchronization of Adaptive Networks, Phys. Rev. Lett. **107**, 234103 (DOI:10.1103/PhysRevLett.107.234103).

[72] Danziger M. M. *et al.* (2016), Explosive synchronization coexists with classical synchronization in the Kuramoto model, Chaos: An Interdisciplinary Journal of Nonlinear Science **26**, 065307 (DOI:10.1063/1.4953345).

[73] Strogatz S. H. and Mirollo R. E. (1991), Stability of incoherence in a population of coupled oscillators, Journal of Statistical Physics **63**, 613-635 (DOI:10.1007/BF01029202).

[74] Jia Y.-B. (2020), Roots of Polynomials, available at: `http://web.cs.iastate.edu/~cs577/handouts/polyroots.pdf`.

[75] Vlasov V. *et al.* (2015), Explosive synchronization is discontinuous, Phys. Rev. E **92**, 012904 (DOI:10.1103/PhysRevE.92.012904).

[76] Omel'chenko, O. E. and Wolfrum M. (2012), Nonuniversal Transitions to Synchrony in the Sakaguchi-Kuramoto Model, Phys. Rev. Lett. **109**, 164101 (DOI:10.1103/PhysRevLett.109.164101).

[77] Abrams D. M. *et al.* (2008), Solvable Model for Chimera States of Coupled Oscillators, Phys. Rev. Lett. **101**, 084103 (DOI:10.1103/PhysRevLett.101.084103).

[78] Laing C. R. (2009), Chimera states in heterogeneous networks, Chaos: An Interdisciplinary Journal of Nonlinear Science **19**, 013113 (DOI:10.1063/1.3068353).

[79] Barreto E. *et al.* (2008), Synchronization in networks of networks: The onset of coherent collective behavior in systems of interacting populations of heterogeneous oscillators, Phys. Rev. E **77**, 036107 (DOI:10.1103/PhysRevE.77.036107).

[80] Bick C. *et al.* (2018), Chaos in Kuramoto oscillator networks, Chaos: An Interdisciplinary Journal of Nonlinear Science **28**, 071102 (DOI:10.1063/1.5041444).

[81] Montbrió E. *et al.* (2004), Synchronization of two interacting populations of oscillators, Phys. Rev. E **70**, 056125 (DOI:10.1103/PhysRevE.70.056125).

[82] Zhang X. *et al.* (2016), Model bridging chimera state and explosive synchronization, Phys. Rev. E **94**, 012204 (DOI:10.1103/PhysRevE.94.012204).

[83] Maksimenko V. A. *et al.* (2016), Excitation and suppression of chimera states by multiplexing, Phys. Rev. E **94**, 052205 (DOI:10.1103/PhysRevE.94.052205).

[84] Frolov N. S. *et al.* (2018), Macroscopic chimeralike behavior in a multiplex network, Phys. Rev. E **98**, 022320 (DOI:10.1103/PhysRevE.98.022320).

[85] Pietras B. and Daffertshofer A. (2019), Network dynamics of coupled oscillators and phase reduction techniques, Phys. Rep. **819**, 1-105 (DOI:10.1016/j.physrep.2019.06.001).

[86] Bassett D. S. *et al.* (2011), Dynamic reconfiguration of human brain networks during learning, Proceedings of the National Academy of Sciences **108**, 7641–7646 (DOI:10.1073/pnas.1018985108).

[87] Buldú, J. M. and Porter M. A. (2018), Frequency-based brain networks: From a multiplex framework to a full multilayer description, Network Neuroscience **2**, 418-441 (DOI:10.1162/netn_a_00033).

[88] Leyva I. *et al.* (2013), Explosive transitions to synchronization in networks of phase oscillators, Sci. Rep. **3**, 1281 (DOI:10.1038/srep01281).

[89] Um J. *et al.* (2011), Synchronization in interdependent networks, Chaos: An Interdisciplinary Journal of Nonlinear Science **21**, 025106 (DOI:10.1063/1.3596698).

[90] Makovkin S. *et al.* (2017), Multiplexing topologies and time scales: The gains and losses of synchrony, Phys. Rev. E **96**, 052214 (DOI: 10.1103/PhysRevE.96.052214).

[91] Leyva I. *et al.* (2018), Relay synchronization in multiplex networks, Sci. Rep. **8**, 8629 (DOI:10.1038/s41598-018-26945-w).

[92] Jadbabaie A. *et al.* (2004), On the Stability of the Kuramoto Model of Coupled Nonlinear Oscillators, Proceedings of the 2004 American Control Conference, Boston, Massachusetts, 4296-4301.

[93] Martens E. A. *et al.* (2009), Exact results for the Kuramoto model with a bimodal frequency distribution, Phys. Rev. E **79**, 026204 (DOI:10.1103/PhysRevE.79.026204).

[94] Pietras B. *et al.* (2016), Equivalence of coupled networks and networks with multimodal frequency distributions: Conditions for the bimodal and trimodal case, Phys. Rev. E **94**, 052211 (DOI:10.1103/PhysRevE.94.052211).

[95] Volo M. D. and Torcini A. (2018), Transition from Asynchronous to Oscillatory Dynamics in Balanced Spiking Networks with Instantaneous Synapses, Phys. Rev. Lett. **121**, 128301 (DOI:10.1103/PhysRevLett.121.128301).